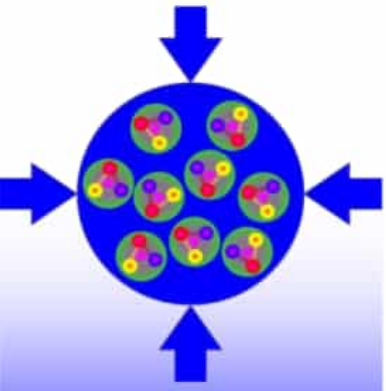

Compressed Baryonic Matter Experiment

mCBM@SIS18

The CBM Collaboration

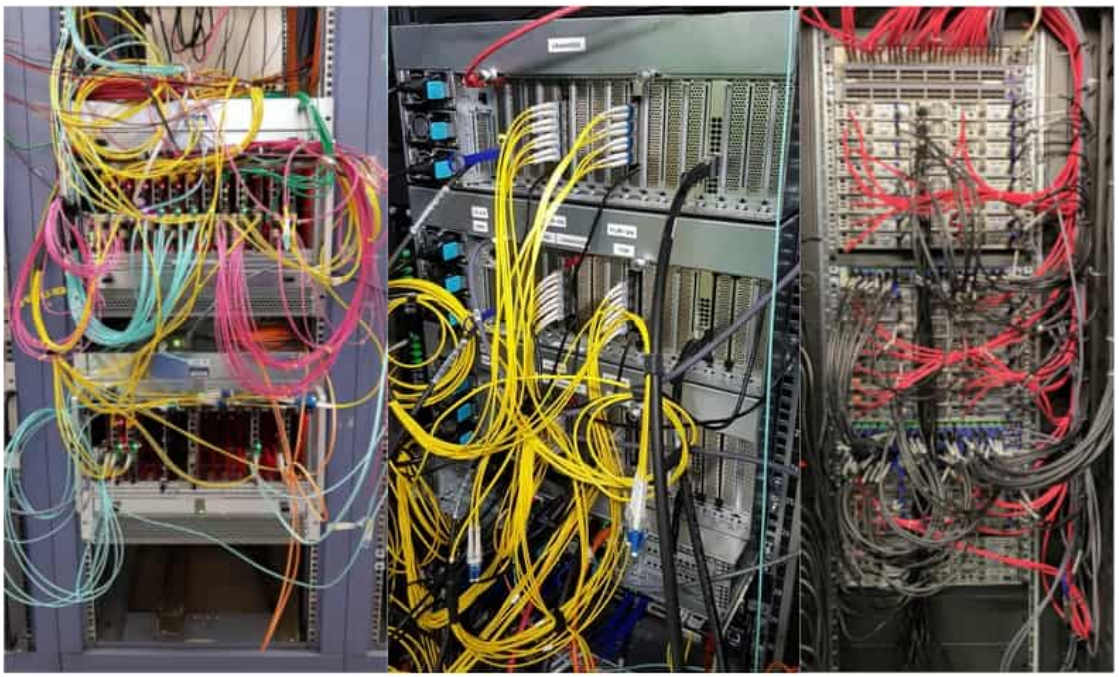

June 2020

mCBM@SIS18 2021/22 - Application for beam time at GSI/FAIR

Submitted to the General Program Advisory Committee (G-PAC) of GSI / FAIR
on June 10th, 2020

Authors: The CBM Collaboration
Responsible Editors: Norbert Herrmann and Christian Sturm

Publication year: 2025
Publisher: GSI Helmholtzzentrum für Schwerionenforschung GmbH
Planckstraße 1 / 64291 Darmstadt / Germany

DOI 10.15120/GSI-2025-00773

Application for beam time at GSI/FAIR (continuation request)

mCBM@SIS18 2021/22

A CBM full system test-setup for high-rate nucleus-nucleus collisions at GSI / FAIR

The CBM Collaboration

corresponding authors:
Norbert Herrmann and Christian Sturm

Submitted to the
General Program Advisory Committee (G-PAC) of GSI / FAIR
June 10th, 2020

CBM SVN revision 9231, June 10th, 2020

Executive summary

This beam time application submitted in June 2020 is a continuation request by the CBM Collaboration, following the proposal on the CBM full-system test-setup at the SIS18 facility under the name *mCBM@SIS18* (short "mCBM"), which was fully granted in September 2017. The primary aim of the mCBM setup is to commission and optimize the complex interplay of the different detector systems with the triggerless-streaming data acquisition and the fast online event reconstruction and selection. In particular, it allows testing of the detector and electronics components developed for the CBM experiment as well as the corresponding online/offline software packages under realistic experiment conditions up to the top CBM interaction rates of 10 MHz.

Construction of the mCBM cave (HTD) incl. experiment infrastructure started directly after acceptance of the initial proposal and was completed by mid 2018. This was subsequently followed by the setup of first detector stations. Optical fibers connect the mCBM setup with the mCBM DAQ container and furthermore with the Green IT Cube hosting the entry and processing nodes for online reconstruction and selection as well as data storage. Commissioning with beam started during the machine engineering runs in December 2018, followed by a main beam period in March 2019. With tests during the machine engineering runs in November and December 2019 we proceeded with the second year of commissioning with beam, followed by the main beam time March 27th to May 24th, 2020, which used completely the granted contingent of beam time. First results show time and spatial correlations between the synchronized data streams of the detector subsystems demonstrating for the first time a conceptual verification of the triggerless-streaming read-out and data transport of CBM.

In the period Q3 2020 to Q1 2021 major upgrades will be conducted on the triggerless-streaming DAQ system, on the detector subsystems as well as on the online/offline software packages. For commissioning we thus apply for 9 shifts in 2021 as secondary user, taken as single 8h-blocks with at least two days break between shifts. In our experience, this work-shift pattern is the most effective for the commissioning stage. Commissioning the benchmark run planned for 2022, we apply for 6 shifts in 2021, 2 days respectively, as main user to be scheduled subsequently to the first commissioning period.

After achieving full functionality and performance, we intend to validate the read-out and data processing concept of CBM by measuring the Λ production yield in Au + Au and Ni + Ni collisions at top SIS18 energies as a benchmark observable, which will allow comparison with published data. We thus aim to perform high-performance benchmark runs on Λ production at top SIS18 energies in 2022. Hence, we apply for 15 shifts, 5 days respectively, as main user and request in addition 6 secondary-user-shifts for a preparatory phase, taken in single shifts with at least 2 days break between shifts.

In the final development phase of the CBM Micro Vertex Detector (MVD) we intend to test the Monolithic-Active-Pixel-Sensor prototypes named MIMOSIS with UNILAC beam at the X6 and μX0 facilities. We hence apply for 12 shifts as secondary user at the X6 facility and 12 shifts as main user at the μX0 facility.

As an outlook for the years 2023 and 2024, we plan to continue the measurements on sub-threshold Λ production with mCBM at SIS18, performing energy scans down to very low incident energies. There, Λ production becomes extremely rare, benefiting most from the extreme rate capability of the CBM systems, especially the online reconstruction and selection. We expect that these runs will produce new data, to be published in peer-reviewed journals. For this program we estimate a need of about 21 shifts as main user and a preparatory phase with 6 shifts as secondary user per year.

Contents

1 Motivation

The Compressed Baryonic Matter experiment (CBM) at FAIR is designed to measure nucleus-nucleus collisions at an unprecedented interaction rate of up to 10 MHz which will allow study of extremely rare probes with high precision. To achieve this high rate capability, CBM will be equipped with fast and radiation-hard detectors, which are readout via a triggerless-streaming data acquisition system, which will transport data with a bandwidth of up to 1 TB/s to a large scale computer farm, allowing for event reconstruction and first level event selection.

In order to commission and optimize prototypes and pre-series productions of CBM detector systems with their triggerless-streaming read-out chains under realistic experiment conditions, a CBM full-system test-setup named mCBM@SIS18 (short "mCBM") has been constructed at the SIS18 facility of GSI/FAIR. The primary aim of mCBM is to commission and optimize (i) the triggerless-streaming data acquisition system including data transport to a high performance computer farm inside the Green IT Cube at GSI, (ii) the online track and event reconstruction and event selection algorithms and (iii) the offline data analysis as well as the controls software packages. mCBM comprises of final prototypes and pre-series components of all CBM detector subsystems and their read-out systems. Hence, the setup offers additional high-rate detector tests in nucleus-nucleus collisions under realistic experiment conditions. The experiences gained during the complete mCBM campaign will significantly shorten the commissioning period for the full CBM experiment at SIS100. The promising results obtained from the first commissioning phase underlines the key role of mCBM as a demonstrator and powerful tool towards the realization of the CBM experiment.

2 Status of the mCBM experiment

2.1 Setup

The mCBM experiment was setup in 2017 and 2018 at the detector test area HTD[1] situated at the beam entrance of the experimental area Cave-C (HTC), hosting the nuclear structure experiment R^3B. As depicted in Figure 2.1.1, the mCBM test-setup is positioned downstream a solid target under a polar angle of about 25° with respect to the primary beam towards a beam dump located 7 m downstream at the south end of the experimental area. mCBM does not comprise a magnetic field, and, therefore, measures charged particles produced in nucleus-nucleus collisions traversing the detector stations following straight trajectories. While the completion of mCBM is ongoing, the present mCBM setup (as of May 2020) includes detector stations of all CBM subsystems, shown in the photograph of Figure 2.1.1 as well as in the corresponding ROOT geometry (lower panel of Figure 2.1.1). Details are listed in Table 2.1.1.

mT_0	a fast and radiation-hard time-zero (T_0) diamond counter, consisting of 8 vertical strips each of 2 mm width, mounted inside the target chamber, 20cm upstream of the target. The T_0 counter is readout by TOF electronics (PADI and GET 4).
mSTS	2 6 x 6 cm^2 STS prototype modules mounted on a half-ladder, positioned on the 1st station (station 0). Each module contains 1024 channels on each sensor side, readout with 8 STS-XYTER v2.1 located on a FEB-8, interfaced to a GBTx ROB-3.
mMUCH	2 GEM prototype stations consisting of M2 modules with 2304 pads. Each module is equipped with 18x STS-XYTER v2.1 mounted on a single FEB each, interfaced to the GBTx ROB-3.
mTRD	1 TRD prototype module, type 8, 95 x 95 cm^2 large, with 768 rectangular pads, 6 FEB-4x1-2 per module interfaced to the GBTx ROB-3.
mTOF	5 TOF M4 prototype modules each containing 5 MRPC counters (32 x 27 cm^2). The readout is performed with PADI and GET 4 electronics interfaced to the GBTx ROB-1 as used in FAIR phase 0 at STAR. In total 1600 read-out channels.
mRICH	2 aerogel radiators each with size 20 x 20 cm^2, equipped with 36 MAPMTs, connected to 72 DiRICH modules, readout with TRB3.
mPSD	a single PSD module, readout by a PANDA ADC board.

Table 2.1.1: Detector stations of the mCBM test setup as of May 2020. A detailed description of each detector subsystem is given in the corresponding appendix subsection of this document's full version.

mCBM uses a right-handed coordinate system, where the origin is located in the target position, see lower panel of Figure 2.1.1. The x-axis (red) is horizontally aligned, the y-axis (green) is pointing vertically upwards, the z-axis (blue) is also horizontally oriented, but rotated around the y-axis by -25° away from the direction of the primary beam. The active detector areas are aligned in the x-y plane, in the perspective of an observer positioned downstream of the mCBM setup, who looks to the upstream direction, towards the negative z-direction. This representation is identical to the one which will be used for the full CBM experiment.

[1] German abbreviation: Hochenergie Transport D

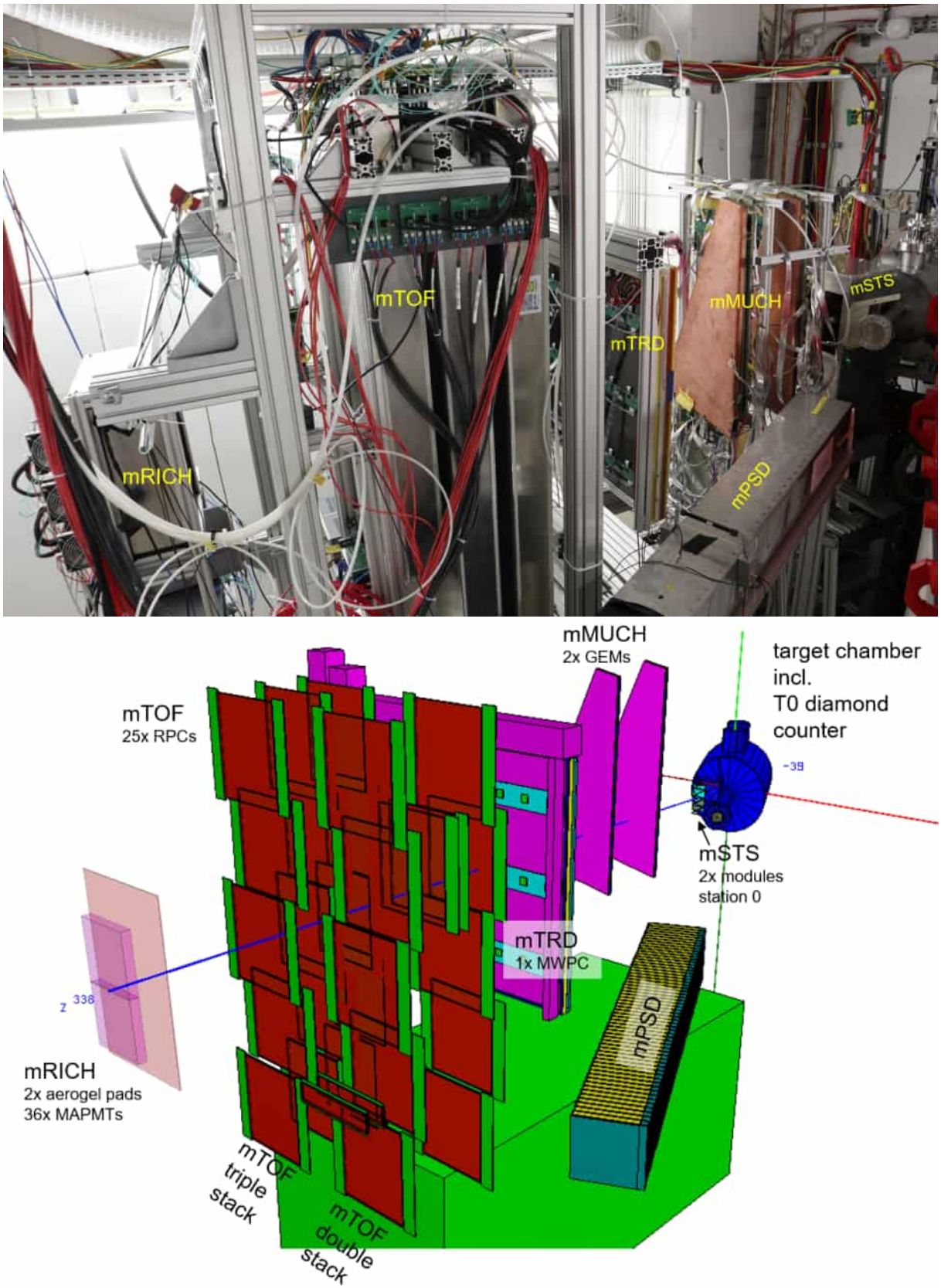

Figure 2.1.1: Photograph of the mCBM setup inside the HTD cave and ROOT geometry (lower panel) of the present mCBM setup as of May 2020. The beam enters from the right.

For track reconstruction, the May 2020 mCBM-setup comprises 1 (half) STS station (mSTS), 2 MUCH (mMUCH) and 1 TRD station (mTRD) making 4 tracking layers which provide redundant position information. The 5 super-modules of the mTOF subsystem has been grouped into a double- and triple-stack for the first commissioning period enabling tracklet searches within the mTOF system as well as detector tests incl. efficiency measurements of TOF-RPC modules. The high-resolution time-of-flight system consists of a fast and segmented diamond counter for time-zero (T_0) determination positioned 20 cm upstream of the target and a TOF stop wall (mTOF). The mRICH subsystem using 2x aerogel radiators is placed directly behind the mTOF detector and delivers a second measurement of the particle velocity in a selected acceptance window. Additionally, mCBM is equipped with a single PSD prototype-module (mPSD) positioned directly under the optical axis of the primary beam, 5° tilted relative to the beam axis while pointing to the target.

In the period Q3 2020 – Q1 2021, it is intended to expand the setup by integrating 5 STS ladders (mSTS), 3 MUCH stations (mMUCH) and 2 TRD station (mTRD). These will provide 6 tracking layers in total, offering redundant position information and allow to perform tracklet searches. Accordingly, the mTOF is going to be supplemented by a 2nd layer of RPC modules, see Figure 2.1.2. Additional tests of MUCH RPCs, TRD modules of the TRD inner part (mTRD-2D) and high-rate TOF modules for the inner region are foreseen for the beam campaign in 2021. Furthermore, the mCBM vacuum system is to be completed as well as the cooling of the experimental area is to be upgraded. In a later stage MVD stations (mMVD) will be added into the test-setup enabling a high-precision vertex reconstruction. Detailed descriptions of each detector subsystem, their technologies, read-out system, and system completion plan is given in the corresponding appendix subsection B as well as in the Technical Design Report (TDR) of the detector subsystems [5] - [10].

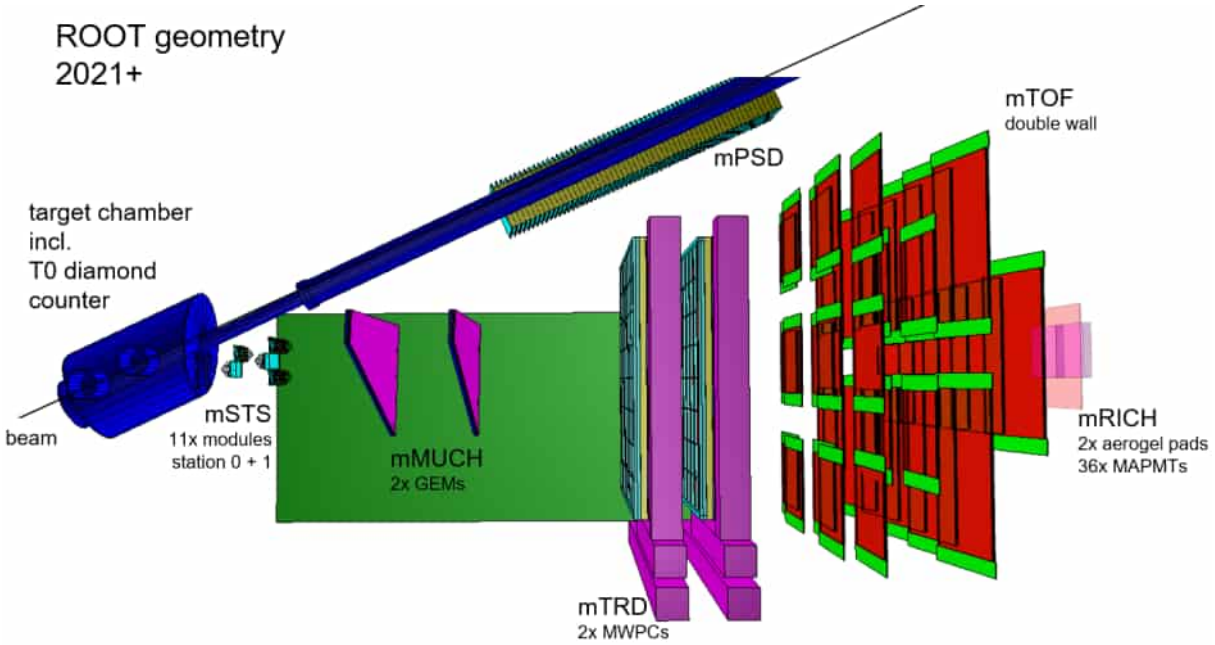

Figure 2.1.2: ROOT geometry for 2021 as of May 2020. Additional detector layers to be mounted for the planned detector tests in 2021 are not yet included.

2.2 Data acquisition and data transport

The CBM experiment at FAIR will measure relativistic nucleus-nucleus collisions with collision rates up to 10 MHz leading to data rates up to 1 TB per second. To achieve the required performance a triggerless-streaming data acquisition system is being developed, see Fig. 2.2.1. It includes ultra-fast and radiation-tolerant ASICs as front-end chips followed by CERN GBTx-based radiation-tolerant data aggregation units. Further down-stream, the data streams are handled by Data Processing Boards (DPB) containing powerful FPGAs. Next, they are forwarded via FLES Input Boards (FLIB), a PCIe based FPGA card, into the First-Level Event Selector (FLES), a computer farm, which performs on-line event selection. At mCBM these components of the readout chain, see Fig. 2.2.2, are spread across different locations, see Fig. 2.2.3. The described high-performance readout hardware needs high-performance firmware for the FPGA layers up to a fast and highly parallel on-line track and event reconstruction and analysis software.

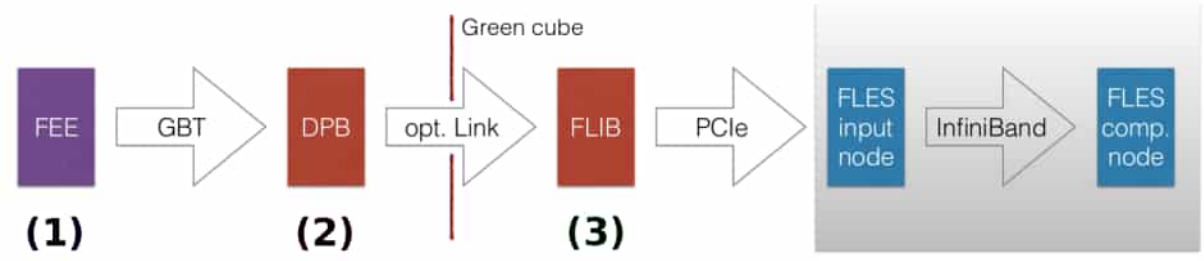

Figure 2.2.1: The mCBM readout chain based on DPB and FLIB, as operated until May 2020. The mCBM subsystems installed in the cave **(1)** are equipped with individual front-end electronics. These front-ends are interfaced by the GBTx ASIC, which forwards the detector data via optical GBT links. All GBT links are received by the DBP layer located at 50 m distance in the DAQ container **(2)**. The DPB is a FPGA based board, which allows for subsystem specific pre-processing of the arriving data stream. A 300 m long optical link connects the DPB output to the FLIB board installed in the FLES entry node in the GreenITCube **(3)**. The FLIB transports the arriving data in micro-slice format into the the memory of the FLES entry node. An InfiniBand network links the FLES entry nodes to the FLES processing nodes. Upon reception in a FLES processing node the micro-slices originating from all active subsystems are grouped into larger time-slices. These time-slices are then used for the online data reconstruction.

In 2019/2020 the mCBM detector front-ends are time-synchronized by the Timing and Synchronisation (TS) system, which relies on a simple clock and pulse-per-second (PPS) distribution. The detector front-end digitizes signals above threshold and assigns a time stamp to the hit. This data is then forwarded via an electrical connection to the GBTx readout board, where the electrical signals acquired through a large number of e-links are converted and merged into an optical GBT link operating at 4.48 Gbit/s. These GBT links are the detector interface to the Data AcQuisition (DAQ) chain. The detector subsystems are presently readout using read-out chains based on existing prototype implementations of DPB and FLIB. As current prototype hardware, an AMC FMC Carrier Kintex (AFCK) board is used for the DPB, a HiTech Global HTG-K700 PCIe board for the FLIB. Both boards are based on a Xilinx Kintex-7 FPGA.

Early 2021, DPB and FLIB will be replaced by a prototype of the Common Readout Interface (CRI) in the FLES entry stage, as it is foreseen for the CBM experiment. To reduce the number of FPGAs operated in the chain, these two will be substituted by a single device, the CRI, see details in Tab. 2.2.1.

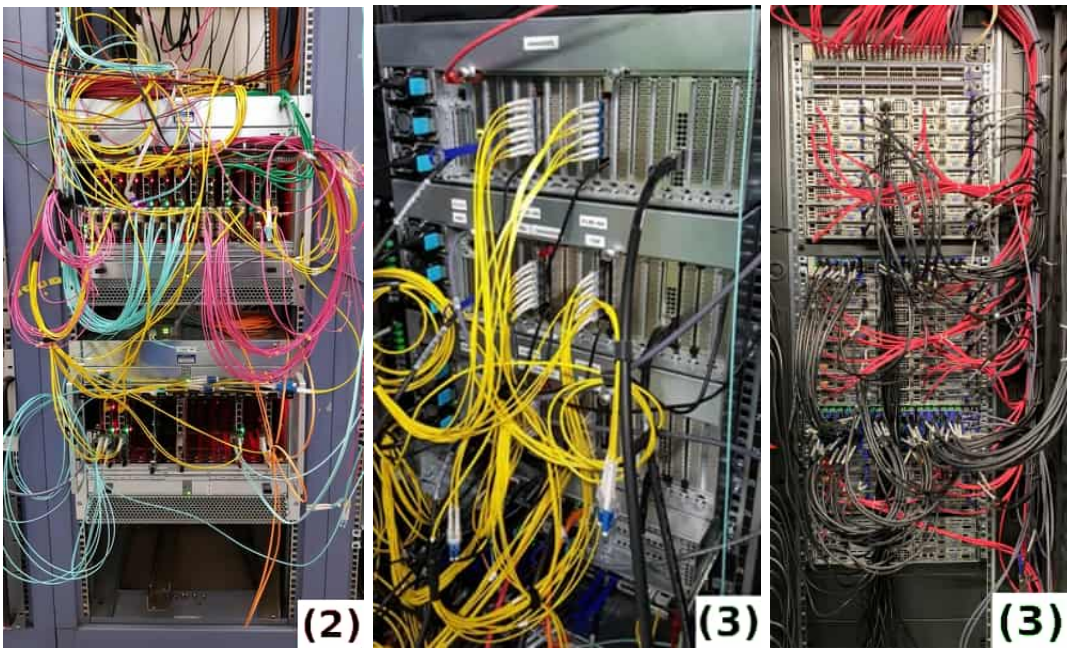

Figure 2.2.2: (left) The 1st processing stage of the triggerless streaming readout chain is located in the DAQ container. The GBT links originating from the experimental setup are interfaced to two microTCA crates **(2)**. Those are housing several DPB boards which receive data on up to 6 incoming optical links at a rate of 4.48 Gbps, perform some pre-processing and then forward that data via a single 10.0 Gbps fast optical link. (middle) The data sent from the DPBs is received by three FLES entry nodes **(3)**, installed rack 5A-60 in the GreenITCube. An entry node is equipped with two FLIB boards, each terminating four single mode fiber connections. (right) The FLES processing nodes **(3)** are mounted in the neibouring rack 5A-61. The stream of micro-slices departing from the FLES entry cluster is reassembled to time-slices upon reception in the processing nodes. A time-slice contains the data of all mCBM subsystems for a given period of time, typically 100 ms. The time-slices are then stored to disk and further processed for online monitoring.

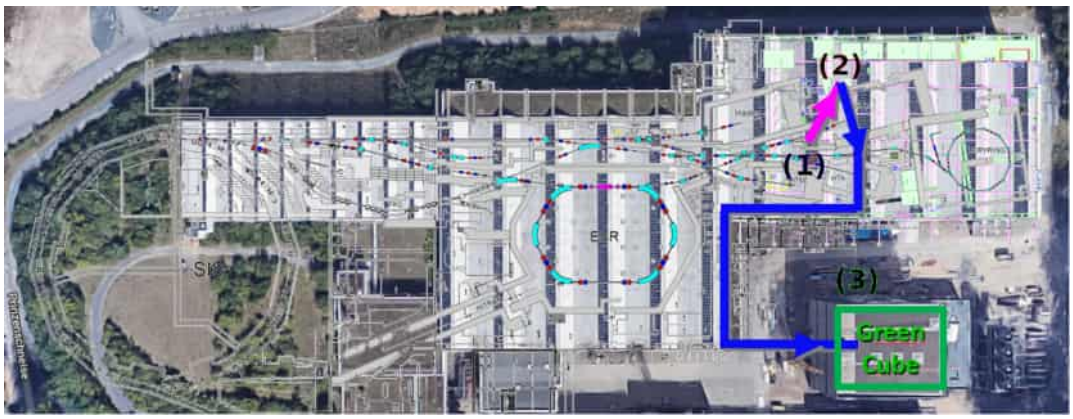

Figure 2.2.3: Site map of the components in the mCBM triggerless streaming readout chain (with backgrund image from Google Maps): the experimental setup, equipped with various types of front-end electronics and the GBTx readout boards, is located in the mCBM cave **(1)**. They are linked by 50 m long multi-mode fibers to the Data Processing Boards (DPB) operated in microTCA crates, which are installed in the DAQ container **(2)**. A 300 m long single-mode fiber connection forwards the data stream to the FLES cluster, consisting of entry and processing nodes, in the GreenITCube **(3)**.

component	description	FPGA type	current prototype	usage
DPB	Data Processing Board	Kintex-7	AFCK	2019/2020
FLIB	FLes Interface Board	Kintex-7	HTG-K700 (PCIe)	2019/2020
CRI	Common Readout Interface	UltraScale	BNL-712 (PCIe)	2021/2022

Table 2.2.1: Overview of the main CBM DAQ components and their implementation (top) prior to (bottom) and after the upgrade.

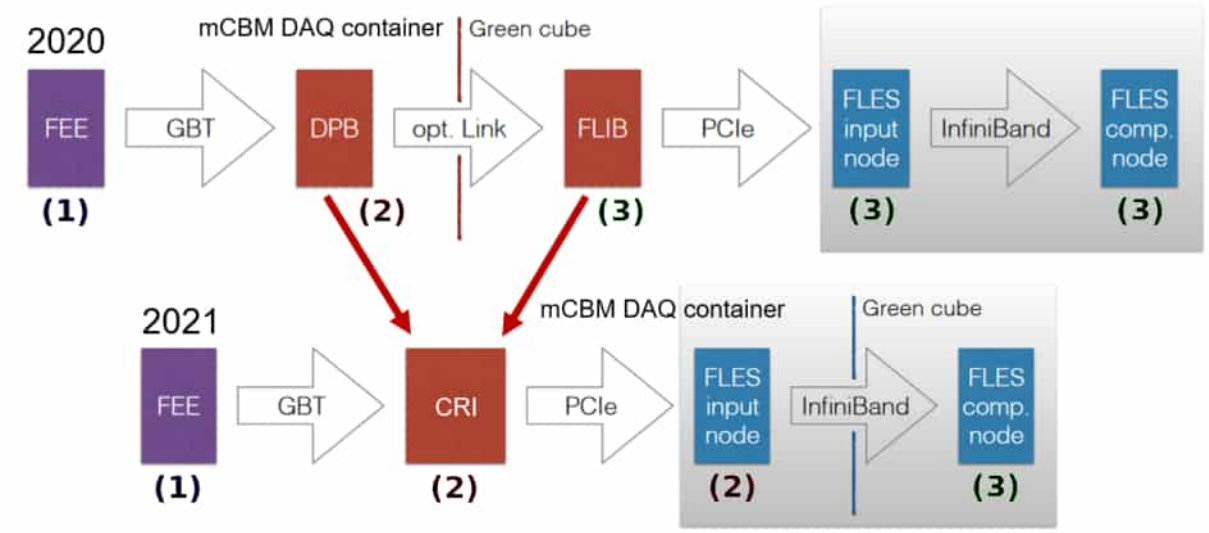

Figure 2.2.4: The mCBM readout chain in operation until May 2020 consists of 2 distinct FPGA boards, the DPB and the FLIB (top). In view of the upgrade of the readout system for spring 2021, both FPGAs will be replaced by a single FPGA entity, the CRI (bottom). As a concequence, the entry nodes housing the CBI boards will have to be relocated from the GreenITCube **(3)** into the mCBM DAQ container **(2)**. The 300 m long optical link between the entry node cluster and the processing node cluster will be operated employing standard Infiniband network technology.

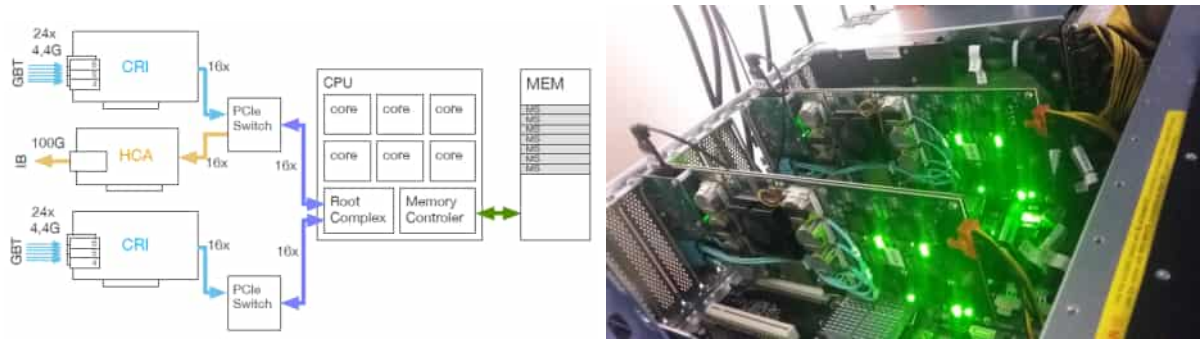

Figure 2.2.5: (left) An entry node will be populated with 2 CRI boards for the incoming GBT links and 1 Infiniband HCA for outgoing data to processing nodes. (right) Two CRI boards installed and powered in a prototype entry node.

2.3 First commissioning results

mCBM commissioning with beam	projectile	kin. projectile energy
2018		
Nov. 24, Dec. 13	^{108}Ag	1.20 AGeV
2019		
Mar. 12, 16, 23, 28, 30	^{108}Ag	1.58 AGeV
Nov. 27, Dec. 12	^{40}Ar	1.70 AGeV
2020		
Mar. 27, 29, 30, 31, Apr. 1, 2, 3, 5	^{206}Pb	1.075 AGeV
Apr. 24, 28, May 4	^{208}Pb	1.060 AGeV
May 24	^{209}Bi	1.078 AGeV

Table 2.3.1: mCBM commissioning with beam.

Commissioning with beam has started during the machine engineering runs in December 2018, followed by first the year's main commissioning beam time during March 2019, see Table 2.3.1. The second year's campaign started with firsts tests during machine engineering runs in November and December 2019, while the main commissioning with beam took place from March 27th to May 24th of 2020, which used completely the granted contingent of beam time. As experienced to date, 8 - 12 h beam blocks with breaks of at least two days in between, turned out to be the most efficient commissioning mode, since it allows to perform reasonable test sequences with beam, while permitting adaption of the setup or improvements of the firm- and software during breaks.

Significant improvements of the detector subsystems have been made during the first (and past) commissioning phase. This includes the data transport starting at the front-end ASICs through the data aggregation ASICs (CERN GBTx) to the FPGAs of the data processing boards (DPB). Hence, the DPB firmware development has been, and still is an essential part of the mCBM commissioning. In particular, timing stability of subsystem data streams at high data loads approaching resource limits of the DPB FPGA remains challenging, but could be handled during the recently completed beam campaign (see Table 2.3.1). The data analysis technique for the individual subsystems as well as for the common data analysis is still under development while the data analysis of May 2020 data is ongoing.

The mCBM setup offers the unique opportunity to test detector prototypes under real CBM conditions, i.e. with high intensive heavy ion beams. The necessary environment is given to measure the rate and multi-hit capability of detectors at full counter illumination (see mTOF track multiplicity, left side of Figure 2.3.4). Especially the rate capability of the counters has to be demonstrated in order to fulfill milestones like Conceptual Design Reviews (CDR) and Production Readiness Reviews (PRR).

For the TOF project the beamtime in 2020 was essential for the following upcoming milestones with target dates in Q3 2020 to Q1 2021: (i) the PRR for float glass MRPCs, (ii) the PRR for low resistivity glass MRPCs, (iii) the ASIC engineering design review (EDR) and (iv) the high voltage CDR. Even though the analysis of data taken during the 2020 beam time is ongoing, already now some preliminary results can be presented here. The left side of Figure 2.3.1 shows the correlation between the observed charged particle flux and the drawn HV current of a MRPC prototype equipped with float glass electrodes. The linear dependence of these two quantities indicates that the counter is capable to stand a particle flux of to at least 2 kHz/cm^2 which

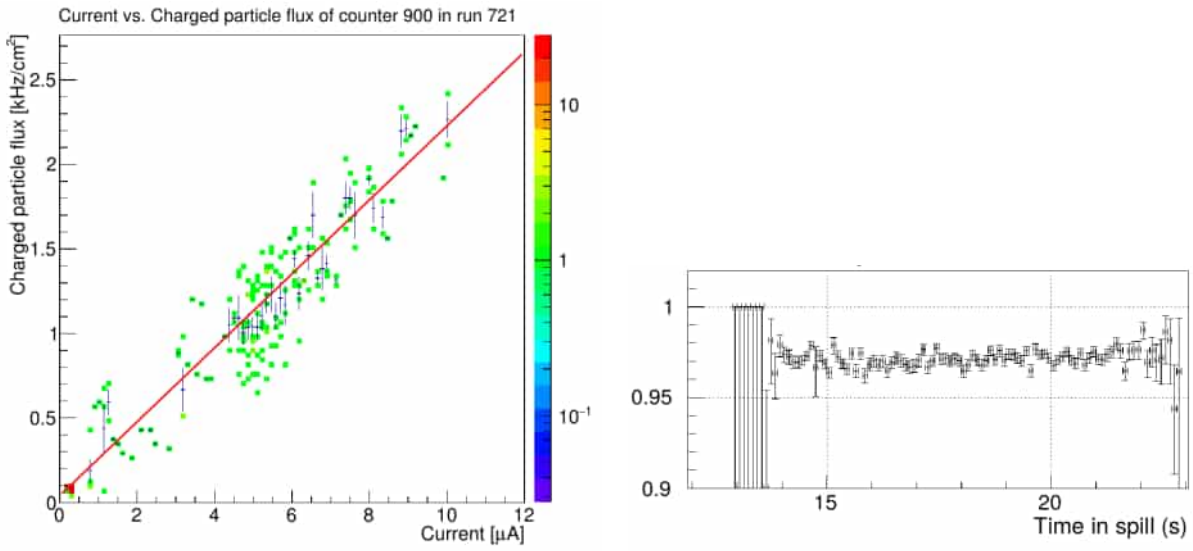

Figure 2.3.1: Correlation between incoming charged particle flux and drawn current of a RPC type MRPC3. In run 721 (April 28, 2020) particle fluxes up to 2 kHz/cm^2 were reached. Right: Efficiency as function of time in spill, at a particle flux of about 600 Hz/cm^2.

is twice as much as the anticipated rate at CBM (essential for milestone (i)). However, this assumption should be confirmed by further data analysis. A first step in this direction was done by analyzing a run where the observed charged particle flux was about 600 Hz/cm^2. The measured efficiency as function of time in spill is depicted on the right side of Figure 2.3.1 and amounts to 96 % without any degradation with time.

The left plot in Figure 2.3.1 is essential for fulfillment of milestone (iv) as well. In order to design and optimize the HV system for the full TOF wall at CBM, precise information on the HV current consumption at a certain rate is required. Based on Figure 2.3.1 and on the recorded MRPC currents an estimation of the highest achieved rates during the 2020 beam time campaign could be made. Close to the beam (on the double stack) a maximal rate averaged over the full module surface of about 7 - 8 kHz/cm^2 could be reached. This is sufficient to characterize the MRPC2 prototype equipped with the low resistivity glass used the intermediate rate region at CBM (milestone (ii)).

Recent, preliminary results of the mCBM commissioning selected for this document have been obtained from the beam campaign March - May 2020, representing the present status of the mCBM experiment (as of May 2020). Data have been taken with a common synchronized data transport including all detector subsystems. Figure 2.3.2 shows the total data rates (scale on the right) as well as data rates broken down by subsystem (scale on the left) observed by the processing nodes of the first-level-event-selector (FLES) inside the Green IT Cube of GSI. The peak total data rate exceeds 2.5 GB per second while the average total data rate measures to 0.85 Gb per second in ^{208}Pb on Au collisions at a collision rate of about 1 MHz (run 858, May 4th, 2020). The largest contribution had been delivered by the mSTS, the smallest by the mPSD and mRICH subsystem.

The key requirement for a triggerless-streaming DAQ system is the timing stability of its detector read-out systems to be verified by time correlations between subsystems, as shown in Figure 2.3.3. Accordingly, the time distributions of the subsystems are plotted with respect to the time-zero counter $t_{subsystem} - t_{T_0}$. Data were taken on May 4th, 2020, in a common, synchronized data transport into the Green IT Cube including all subsystems. All pairs $(t_{subsystem} - t_{T_0})$ within a time slice of length 10.28 ms are taken into account, Figure 2.3.3 shows a zoom-in on

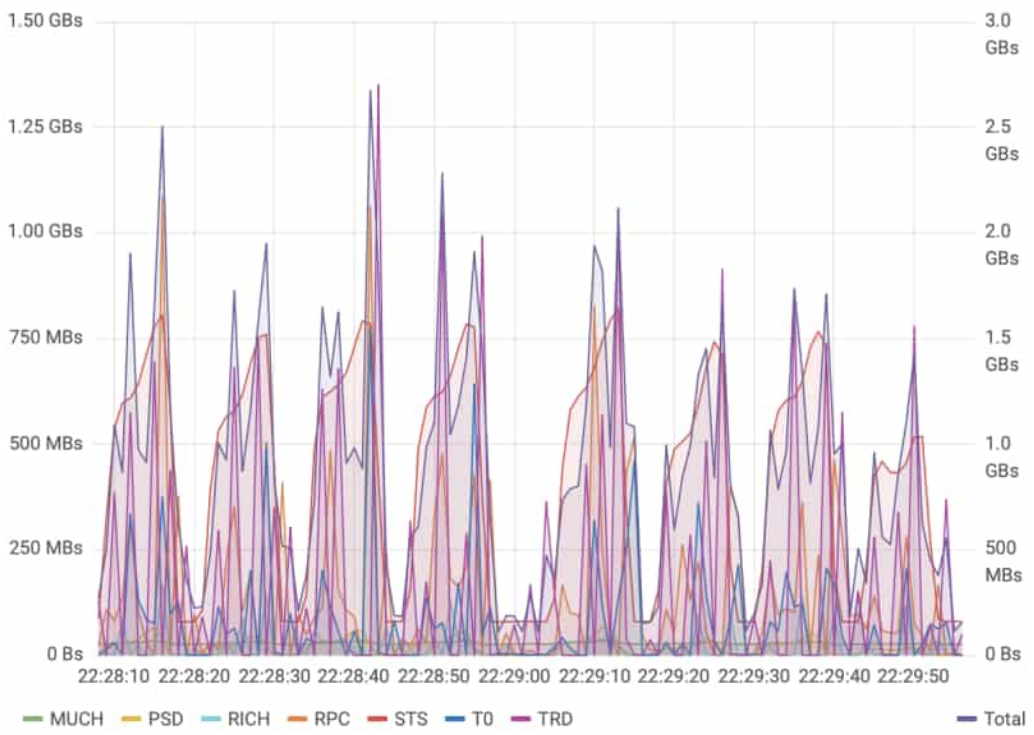

Figure 2.3.2: Total data rate (scale on the right) and break down to subsystem data rates (scale on the left) observed by the FLES processing nodes inside the Green IT Cube, May 4, 2020, run 858.

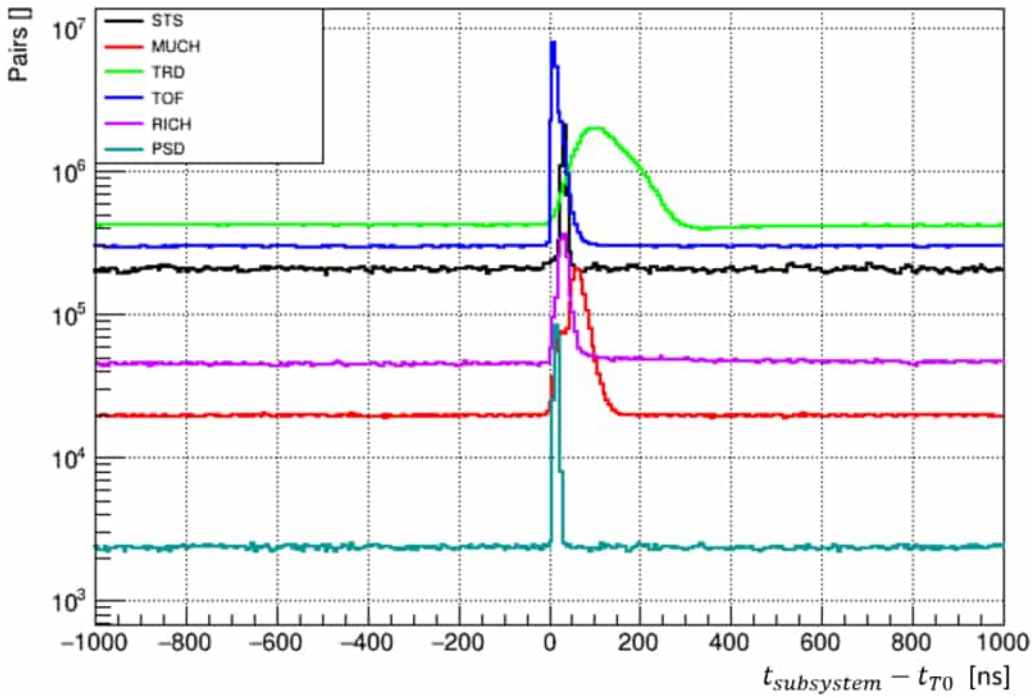

Figure 2.3.3: Time correlation of all subsystems (May 4, 2020, run 831).

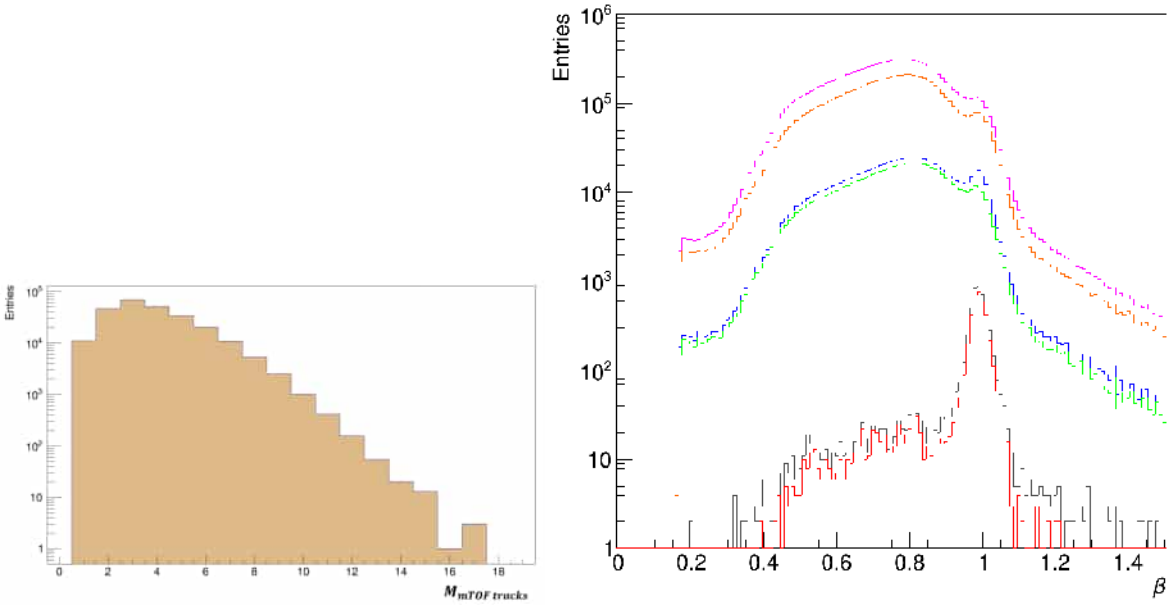

Figure 2.3.4: (left) mTOF track multiplicity, (right) β distribution of reconstructed mTOF tracks, (top = 1 to down = 6 with added event and track selections) (1) magenta: $M_{mTOF\ digi} = 3$, (2) orange: $M_{mTOF\ digi} = 10$, (3) blue: + $M_{mRICH\ digi} = 5$, (4) green: + mRICH hit, no ring, (5) grey: + closed ring in 20% enlarged radius, (6) red: + good rings.

a $\pm 1 \mu s$ range. The depicted time t results from time stamps assigned to the raw hit messages by their front-end ASICs, converted into digis with unit [ns] during the unpacking stage of the data analysis. Individual time offsets of the subsystems are corrected during the unpacking (see Table 2.3.2). No detailed time calibration procedures were applied. In general, the subsystem time offsets remain constant between runs which includes a synchronization sequence prior to each run start. Exceptions caused by detector malfunctions and a non-optimized synchronization sequence of a subsystem were observed.

	mSTS	mMUCH	mTRD	mTOF	mRICH	mPSD
subsystem time offset [ns]	985	885	25	-25	310	240

Table 2.3.2: Subsystem time offsets [ns] in respect to the T_0 counter were corrected during the unpacking stage of the data analysis. The "negative" mTOF time offset is induced by a long cable connection of the T_0 counter to the mTOF system.

After data unpacking, a simplified event building is performed by a time-cluster-search within a fixed window of 200 ns. So, event candidates which are found are then selected for a minimal requirement on the T_0 and mTOF multiplicity: $M_{T0\ \mathrm{digi}} \geq 1$ & $M_{mTOF\ \mathrm{digi}} \geq 10$. Subsequently, detector hits are identified by the subsystem specific cluster and hit finding. Based on reconstructed hits, mTOF tracks are formed by a tracklet search using the three layers of the mTOF triple stack configuration. Figure 2.3.4 shows the multiplicity of mTOF tracks (left side) and their corresponding normalized velocity ($\beta = \mathrm{v/c}$) distribution (right side). An interesting feature of the β spectrum is visible, an enhancement at $\beta = 1$ (speed-of-light). That this peak is caused by electrons is supported by the fact that it is relatively enhanced by matching the mTOF tracks to reconstructed mRICH rings. Comparison to low β tracks originating from hadrons show the enormous suppression power of the RICH system already in this rather limited geometry. The potential source of these electrons is the Dalitz-decay of neutral Pions π^0. Furthermore, the

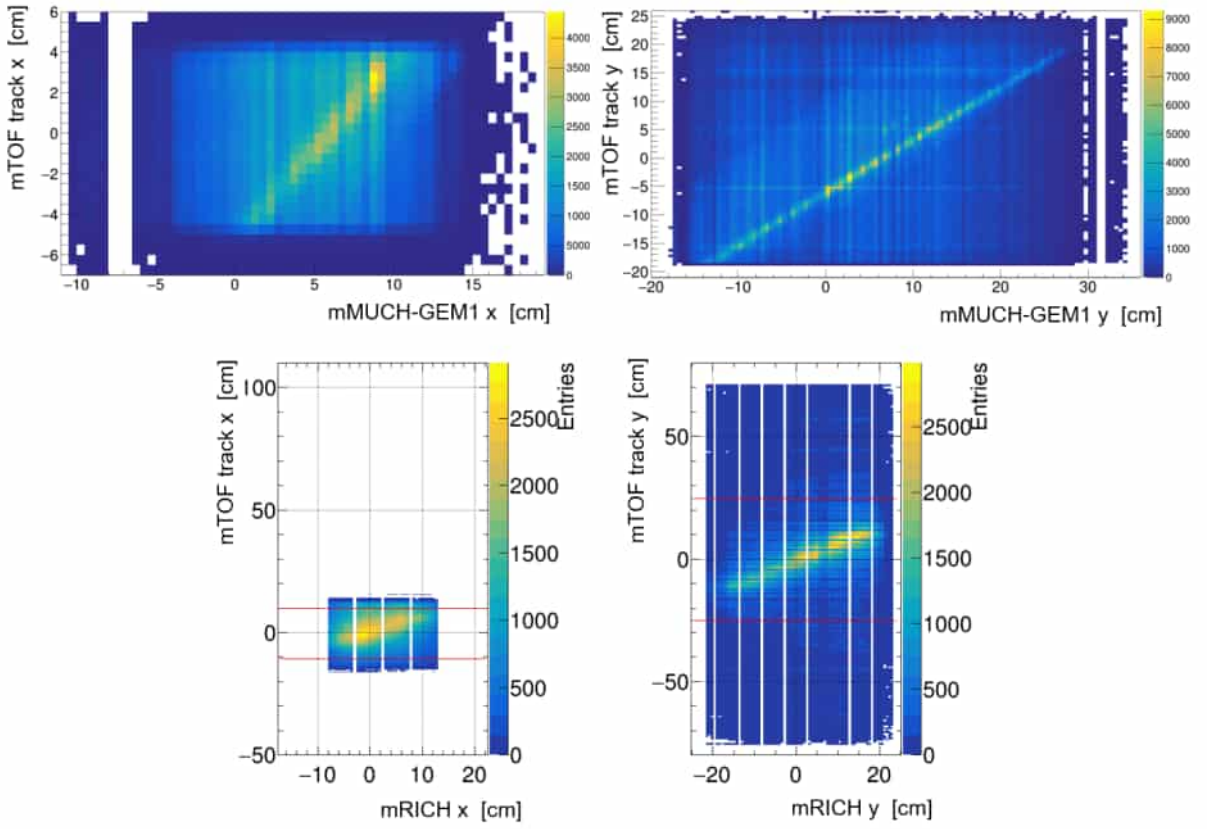

Figure 2.3.5: Correlations between spatial coordinates: mTOF tracks projected on the mMUCH-GEM1 plane vs. reconstructed mMUCH hits (top) and mTOF tracks projected on the mRICH plane vs. reconstructed mRICH hits (bottom). Data were taken in ^{208}Pb + Au collisions at 1.060 AGeV on May 4th, 2020, run 831. A deviation from the bisecting line is caused by alignment uncertainties.

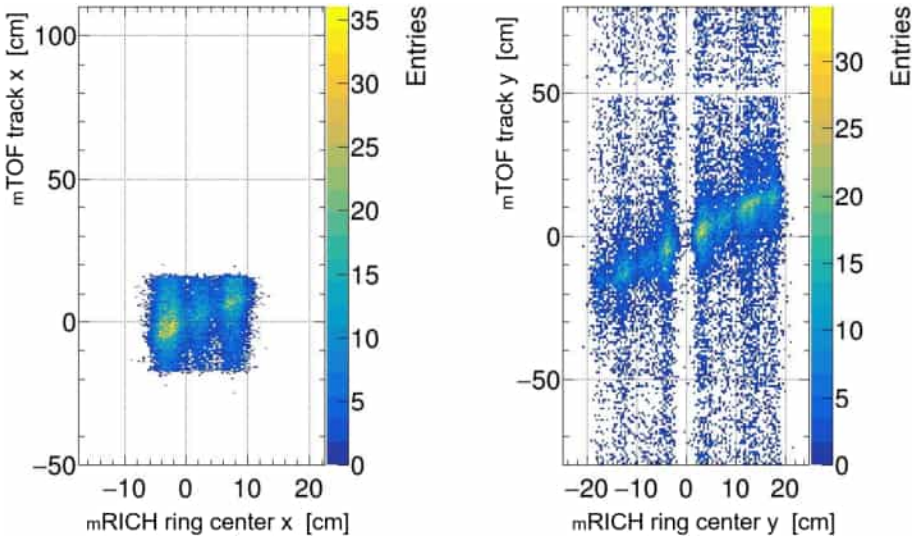

Figure 2.3.6: Spatial correlation: mTOF tracks projected on the mRICH plane vs. center coordinates of reconstructed mRICH rings (May 4, 2020, run 831). The non-optimized ring finding algorithm produces the inhomogeneous distributions.

peak provides a physical calibration point for the absolute timing calibration of the TOF system.

The spatial correlations of mTOF tracks pointing to the mMUCH and mRICH planes to reconstructed mMUCH and mRICH hits are depicted in Figure 2.3.5. One step further, the center coordinates of reconstructed mRICH rings are correlated with coordinates obtained by projection of mTOF tracks on the mRICH plane, Figure 2.3.6.

As a summary, the observed time and spatial correlations between detector subsystems demonstrate a first conceptual verification of the triggerless-streaming DAQ system of CBM. The extension to the other detector subsystems is ongoing.

3 Beam time request

3.1 mCBM during 2021 and 2022

The beam time request of the mCBM experiment for the years 2021 and 2022 is summarized in Table 3.1.1, subdivided into lines (1) - (4).

In the second half of 2020 major mCBM upgrades on the detector subsystems as well as on the triggerless-streaming DAQ system will be realized. Hence, the goal for 2021 is to commission the mCBM experiment to reach the design performance of the triggerless-streaming DAQ system and perform online event reconstruction and selection. Further high-rate tests of detector systems are foreseen. We therefore apply (1) for 9 shifts as secondary user for the commissioning part, taken as single shifts (8h-blocks) with at least 2 days break within shifts. As preparation for the benchmark runs starting in 2022 we apply (2) for 6 shifts in one block, 2 days respectively, as main user.

	year	objective	projectile	intensity	extraction	user type	shifts
(1)	2021	system commissioning incl. online reconstruction & selection	ions 1 - 2 AGeV	10^6 - 10^8 /s	slow, 10 s	secondary	9 (single 8h-blocks)
(2)	2021	commissioning for benchmark runs	Ni 1.93 AGeV	10^7 /s	slow, 10 s	main	6
(3)	2022	preparation of 1st benchmark run	ions 1 - 2 AGeV preferably: Au 1.24 AGeV Ni 1.93 AGeV	10^6 - 10^8 /s	slow, 10 s	secondary	6 (single 8h-blocks)
(4)	2022	1st benchmark run, Λ reconstruction	Au 1.24 AGeV and Ni 1.93 AGeV	10^6 - 10^8 /s	slow, 10 s	main	15

Table 3.1.1: mCBM beam time request for SIS18 beam in 2021 and 2022.

Having established full performance, we intend to perform the 1st benchmark run in 2022 targeting Λ reconstruction in Au + Au collisions at 1.24 AGeV and Ni + Ni collisions at 1.93 AGeV. Both have the advantage of previously published data, the former by the HADES experiment [1], the latter by the FOPI experiment [2]. For the rate estimation, a Monte-Carlo simulation was performed for a feasibility study, which was presented in the first mCBM proposal (submitted to the GSI G-PAC on June 19, 2017) [3]. Since mCBM does not include a magnetic field for momentum measurement, the reconstruction has to be done via time-of-flight (TOF) and track topology. It had been demonstrated that the limited information available for Λ reconstruction is sufficient. Our rate estimation is given in Table 3.1.2. In addition to the production time we request a setup-day (3 shifts) per collision system. Hence, we apply (4) for 15 shifts in total as main user, 5 days respectively. As a preparatory phase for the benchmark run (4), we apply (3) for 6 single shifts with at least two days break between shifts.

collision system	M_Λ, reconstructed	production shifts	total N_Λ, reconstructed
Ni + Ni at 1.93 AGeV	3.9×10^{-5}	3	100k
Au + Au at 1.24 AGeV	2.2×10^{-5}	6	120k

Table 3.1.2: Rate estimation for Λ reconstruction with mCBM, taking as a basis an average collision rate of 10^5/s, assuming a spill length of 10 s, 4 spills per minute and a duty cycle of about 0.5, which results to 9×10^8 collisions per 8h-shift.

3.2 Si-sensor development at X6 and μX0 in 2021 and 2022

The CBM Micro Vertex Detector (MVD) will be formed from highly granular CMOS Monolithic Active Pixel Sensors (CPS, Si-sensors). To match the requirements on position resolution, radiation hardness and read-out speed a next generation CMOS Monolithic Active Pixel Sensor named MIMOSIS is being developed. We propose to systematically test those features by illuminating the current prototype MIMOSIS-1, and in 2022 MIMOSIS-2 with relativistic heavy ion beam at the mCBM beam line and additionally, (5) and (6) (see Table 3.2.1), with low energy ions from the X6 beam line to simulate a beam halo and slow target fragments, respectively. It will in particular reveal the energy threshold for permanent damage caused by gate ruptures and help deciding, if a shielding to the CBM MVD against target fragments has to be considered. The study with relativistic ions at mCBM aims to measure cross-sections for Single Event Effects (SEE) caused by the beam halo. A scan of the MIMOSIS-1 and -2 sensors at the μX0 beam line (7) (see Table 3.2.1) will locate weak points in the design. This knowledge will be used to harden the related structures by layout modification and such allow for further improving the design of the next prototype. A detailed description on this project is given in chapter B.2 of the published long-version of this document. The results will generate a significant visibility beyond CBM within the CPS/MAPS community.

	year	objective	projectile	intensity	user type	shifts
(5)	2021 - 2022	Si-sensor (CPS) study at X6	medium-heavy ions (e.g. Ca, Ti) at max. kin. energy	10^6 /s	secondary	3 + 3
(6)	2021 - 2022	Si-sensor (CPS) study at X6	heavy ions (e.g. Au, Bi) at max. kin. energy	10^6 /s	secondary	3 + 3
(7)	2021 - 2022	Si-sensor (CPS) study at μX0	heavy ions (e.g. Au, Bi) at max. kin. energy	max.	main	6 + 6

Table 3.2.1: Beam time request for UNILAC beam at X6 and μX0 for 2021 and 2022.

3.3 Preview for the years 2023 and 2024

We intend to continue with benchmark physics runs at mCBM in the years 2023 and 2024 laying emphasis on the online/offline Λ reconstruction at various projectile energies. In particular, the Λ production becomes an extremely rare process at low incident energies far below the production threshold in binary nucleon-nucleon reactions. This demands a high rate capability which is well suited to test and optimize the CBM triggerless-streaming DAQ systems including firm- and software and the online/offline software packages with mCBM. On the other hand, we expect new data on sub-threshold Λ production, which can be published in scientific journals. For this program we expect a need of 21 shifts as main user and at a time 4 shifts as preparatory phase for each year (see Table 3.3.1).

year	objective	projectile	intensity	extraction	user type	shifts
2023 2024	preparation of benchmark run	ions 1 - 2 AGeV, preferably: Au 1.24 AGeV, Ni 1.93 AGeV	10^7 - 10^8 /s	slow, 10 s	secondary	4 4
2023 2024	benchmark run, Λ excitation function	Au, Ni 0.8-1.93 AGeV	10^8 /s	slow, 10 s	main	21 21

Table 3.3.1: Preview for 2023 and 2024 on planned request on SIS18 beam time for mCBM.

References

[1] J. Adamczewski-Musch et al. (HADES collaboration),
Sub-threshold production of K0s mesons and Lambda hyperons in Au+Au collisions at sqrt(sNN) = 2.4 GeV, Phys.Lett. B793 (2019) 457-463

[2] M. Merschmeyer et al. (FOPI collaboration),
K^0 and Λ production in Ni+Ni collisions near threshold, Phys. Rev. C 76 (2007) 024906

[3] mCBM@SIS18 - A CBM full system test-setup for high-rate nucleus-nucleus collisions at GSI / FAIR GSI-2019-00977, https://repository.gsi.de/record/220072

[4] Wojciech M. Zabołotny, Grzegorz Kasprowicz, Adrian P. Byszuk, David Emschermann, Marek Gumiński, Krzysztof T. Poźniak and Ryszard Romaniuk,
Selection of hardware platform for CBM Common Readout Interface, Proc. SPIE, vol 10445, 2017, ISBN 9781510613546

[5] J. Heuser, W. F.J. Müller, V. Pugatch, P. Senger, C. J. Schmidt, C. Sturm and U. Frankenfeld,
Technical Design Report for the CBM Silicon Tracking System (STS),
GSI-2013-05499, http://repository.gsi.de/record/54798

[6] S. Chattopadhyay, Y. P. Viyogi, P. Senger, W. F.J. Müller and C. J. Schmidt,
Technical Design Report for the CBM Muon Chambers (MuCh),
GSI-2015-02580, https://repository.gsi.de/record/161297

[7] C. Blume, C. Bergmann, D. Emschermann,
Technical Design Report for the CBM Transition Radiation Detector (TRD),
GSI-2018-01091, http://repository.gsi.de/record/217478

[8] C. Höhne,
Technical Design Report for the CBM Ring Imaging Cherenkov Detector (RICH),
GSI-2014-00528, http://repository.gsi.de/record/65526

[9] N. Herrmann,
Technical Design Report for the CBM Time-of-Flight System (TOF),
GSI-2015-01999, https://repository.gsi.de/record/109024

[10] F. Guber and I. Selyuzhenkov,
Technical Design Report for the CBM Projectile Spectator Detector (PSD),
GSI-2015-02020, https://repository.gsi.de/record/109059

A Common systems

A.1 DAQ and FLES

As already mentioned in the introduction, the mCBM DAQ system is deployed in two phases. During the start-up of mCBM (phase I) in 2018-2020, readout chains based on existing prototype implementations of DPB and FLIB were employed, see Fig. A.1.1. The readout started with a focus on the GBTx-based subsystems (mSTS, mMUCH, mTRD and mTOF). An upgrade of the readout chain will mark the transition to phase II, due early 2021. During this upgrade, the FLES entry nodes will be moved from the Green IT Cube to the mCBM DAQ container, see Fig. A.1.2. The Common Readout Interface (CRI), a PCIe Gen 3 x16 board, will be installed in the FLES entry nodes. The CRI will replace the DPB and FLIB boards and combine their functionality in a single FPGA device. This prototype board will take up to 24 GBT links as input and interface them to the FLES entry node memory. The CRI-based readout chain will be the first prototype implementation for the readout of the CBM experiment at SIS100.

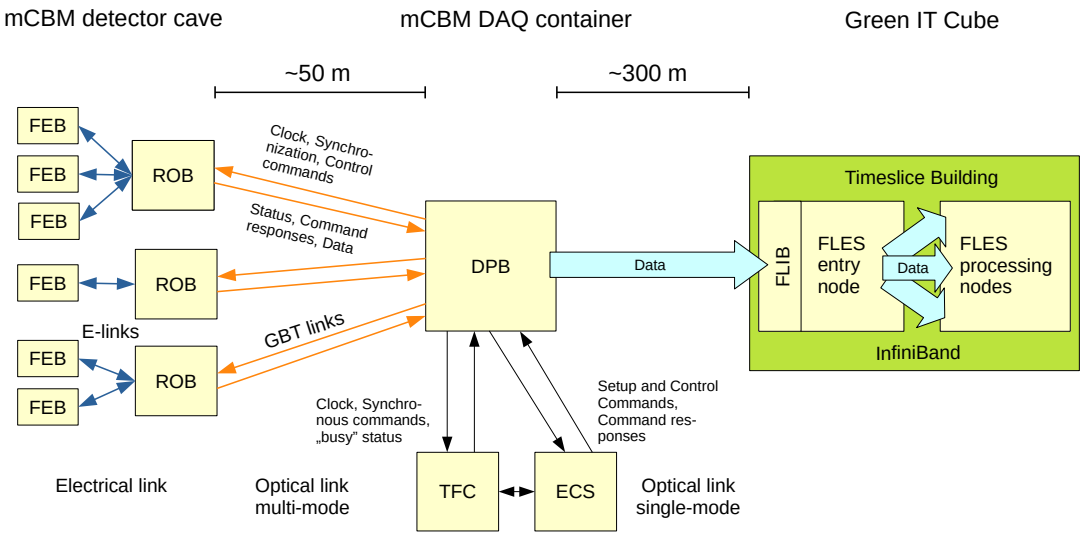

Figure A.1.1: mCBM readout chain in use during phase I, based on existing DPB and FLIB prototypes, adapted from [4]. The data is sent in micro-slices from the DPBs via single-mode optical fibers to the FLES entry nodes located in the Green IT Cube. The micro-slices are then forwarded via InfiniBand network to the FLES processing nodes, where the micro-slices are processed to time-slices. The time-slices are finally used in the online analysis.

In phase I (see Fig. A.1.1), the GBT links are forwarded to the Data Processing Boards (DPB), which are currently realized as AFCK boards operated in a microTCA crate, see Fig. 2.2.2. Preprocessing of the data, e. g. time sorting of the entry streams (mSTS) or feature extraction (mTRD), can be performed at this stage. The DPBs partition the data streams into micro-slices and merge several slower (4.48 Gbit/s) GBT links into a single 10 Gbit/s high-speed link. This link is realised with a trunk cable of single mode optical fibers installed between the DAQ container in the target hall and the Green IT Cube. This single mode fiber ends at the FLIB board located inside the FLES entry node. The current FLIB prototype is a Kintex-7 based PCIe Gen2 x8 board (HTG-K700), which can receive up to 4 optical FLIM links from the AFCKs. The data arriving at the FLIB is indexed and forwarded to its FLES entry node, which

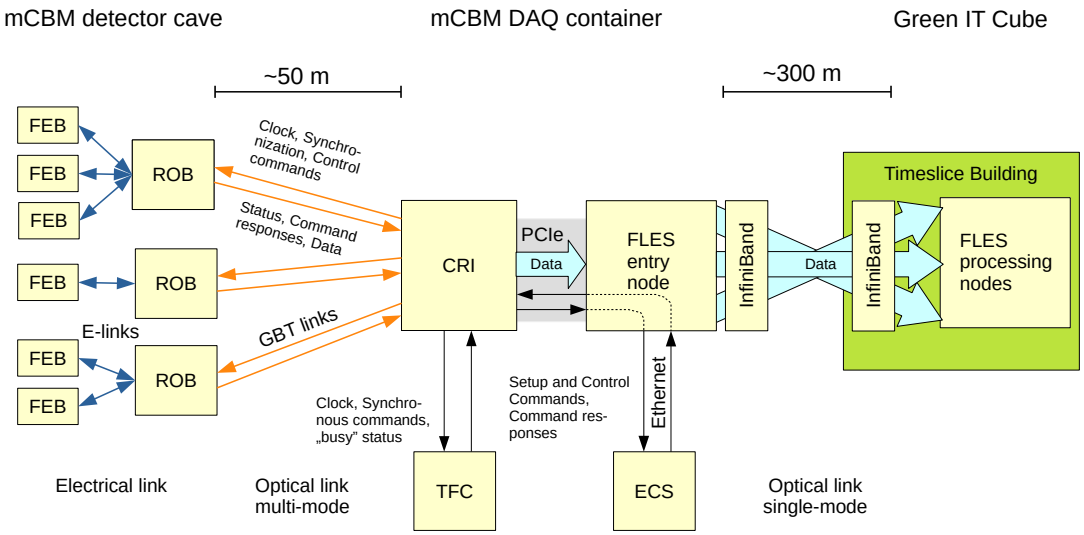

Figure A.1.2: Proposed mCBM readout chain for phase II, based on a CRI prototype board, adapted from [4]. The CRI board is a PCIe card operated in the FLES entry nodes, which were moved from the Green IT Cube into the DAQ container close to the mCBM experimental setup. The connection to the FLES computing nodes installed in the Green IT Cube is done with long-range EDR InfiniBand equipment. The stream of micro-slices sent from the FLES entry nodes is combined to time-slices in the FLES processing nodes.

subsystem	ROB-1	ROB-3	GBTx	DPB	CRI-24
mT_0	2x		2x	2x	1x
mSTS		5x	15x	3x	1x
mMUCH		6x	18x	6x	1x
mTRD-2D		6x	18x	–	1x
mTRD		2x	6x	2x	1x
mTOF	16x		16x	4x	1x
mRICH				1x	1x
mPSD				1x	1x
total	18x	19x	75x	19x	8x

Table A.1.1: Amount of GBT links and CRI used in the readout system during phase II for the full mCBM setup in 2021.

Figure A.1.3: The Common Readout Interface (CRI) board, based on the BNL-712 card, is a PCIe Gen3 x16 device interfacing up to 47 GBT links [4]. This CRI board will be the main component of the DAQ upgrade, replacing both DPB and FLIB (see figures below).

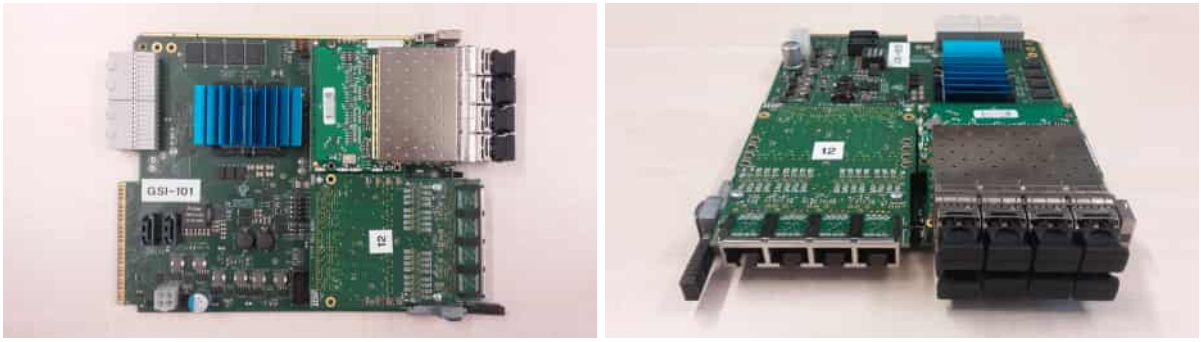

Figure A.1.4: AMC FMC Carrier Kintex (AFCK) board, a Xilinx Kintex-7 FPGA board in AMC form factor equipped with a FM-S18 FMC and a tDPB FMC. An AFCK with this configuration can be used to interface 6x incoming GBT links at 4.48 Gbit/s to 1x outgoing FLIM link.

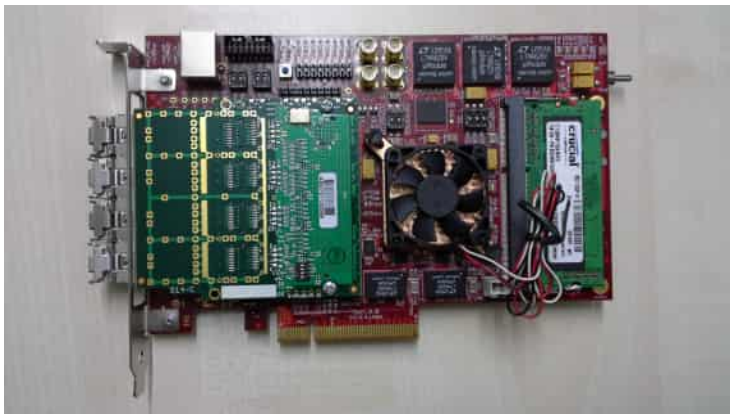

Figure A.1.5: FLES Interface Board (FLIB), a Xilinx Kintex-7 FPGA board with PCIe Gen2 x8 interface equipped with a FM-S14 FMC, offering 4x 10 Gbit/s links. The FLIB is the current interface into the FLES Entry Node (as of June 2017).

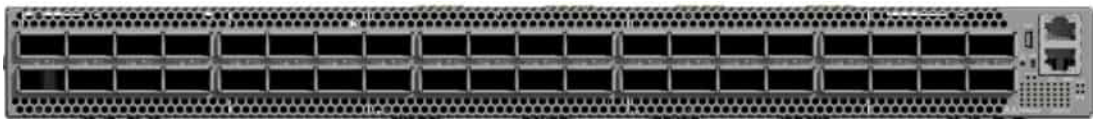

Figure A.1.6: Infiniband QM8700 HDR switch used for the backbone connection between the FLES entry node cluster in the mCBM DAQ container and the FLES processing node cluster in the Green-IT-Cube.

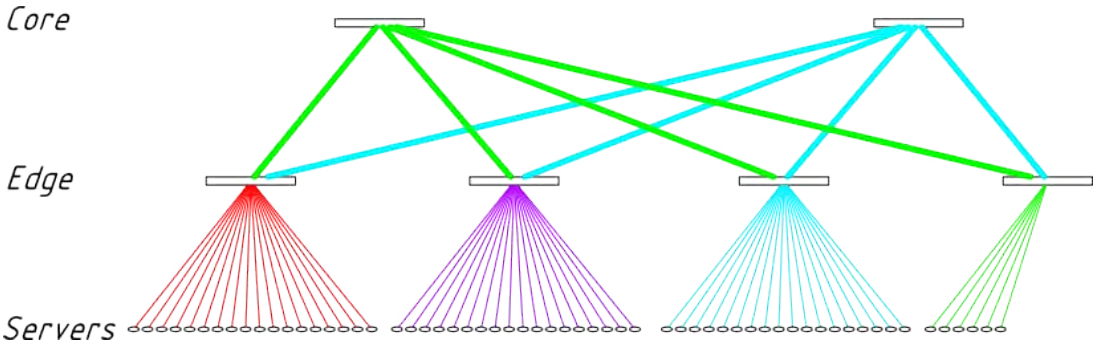

Figure A.1.7: Possible fat-free network topology to be used for the InfiniBand network cabling of the FLES, from *www.clusterdesign.org*. Both FLES entry nodes (EN) and FLES processing nodes (PN) will be connected to edge switches. The fat-tree topology allows to interface any EN with any PN at full bandwidth, which allows to build time-slices from micro-slices concurrently and on the fly.

transmits the data via an InfiniBand network to the FLES processing cluster located in the Green IT Cube. A dedicated topology (Fat-Tree, see Fig.A.1.7) of the InfiniBand network in the Green IT Cube allows to receive micro-slices originating from all active mCBM subsystems in a single FLES processing node. This FLES processing node combines all those micro-slices into a single time-slice, which is then passed to the reconstruction and analysis stage.

In 2021 during phase II, the mCBM readout scheme will be transformed into a prototype of the CBM@SIS100 DAQ chain. The FLES entry nodes will be transferred from the Green IT Cube into the mCBM DAQ container, located in vicinity of the mCBM cave. Here the CRI (see Fig. A.1.3), a PCIe card with a single UltraScale+ FPGA [4], will replace two separate FPGA boards, the DPB (see Fig. A.1.4) and the FLIB (see Fig. A.1.5). The amount of CRI boards required during phase-II of mCBM is summarized in Tab. A.1.1. The CRI will be mounted in the FLES entry node and will be capable of handling up to 24 GBT links. The GBTx modules on the detector front-ends will directly connect to the CRI, as a substitute to the microTCA layer. The CRI combines in a single board the DPB functionality with the micro-slice handling and PCIe interface of the FLIB. Major blocks of the DPB and FLIB firmware will be re-used in the CRI FPGA design. Now that the FLES entry node is located in the DAQ container, it needs to be attached to the distant InfiniBand network in the Green IT Cube to allow for time-slice building on the FLES processing nodes. This long range InfiniBand connection will be realized using the same single mode optical fiber infrastructure as used for the DPB to FLIB connection in phase I.

Figure A.1.8: The Flesnet Overview information page during data taking with mCBM on Monday May 4th 2020.

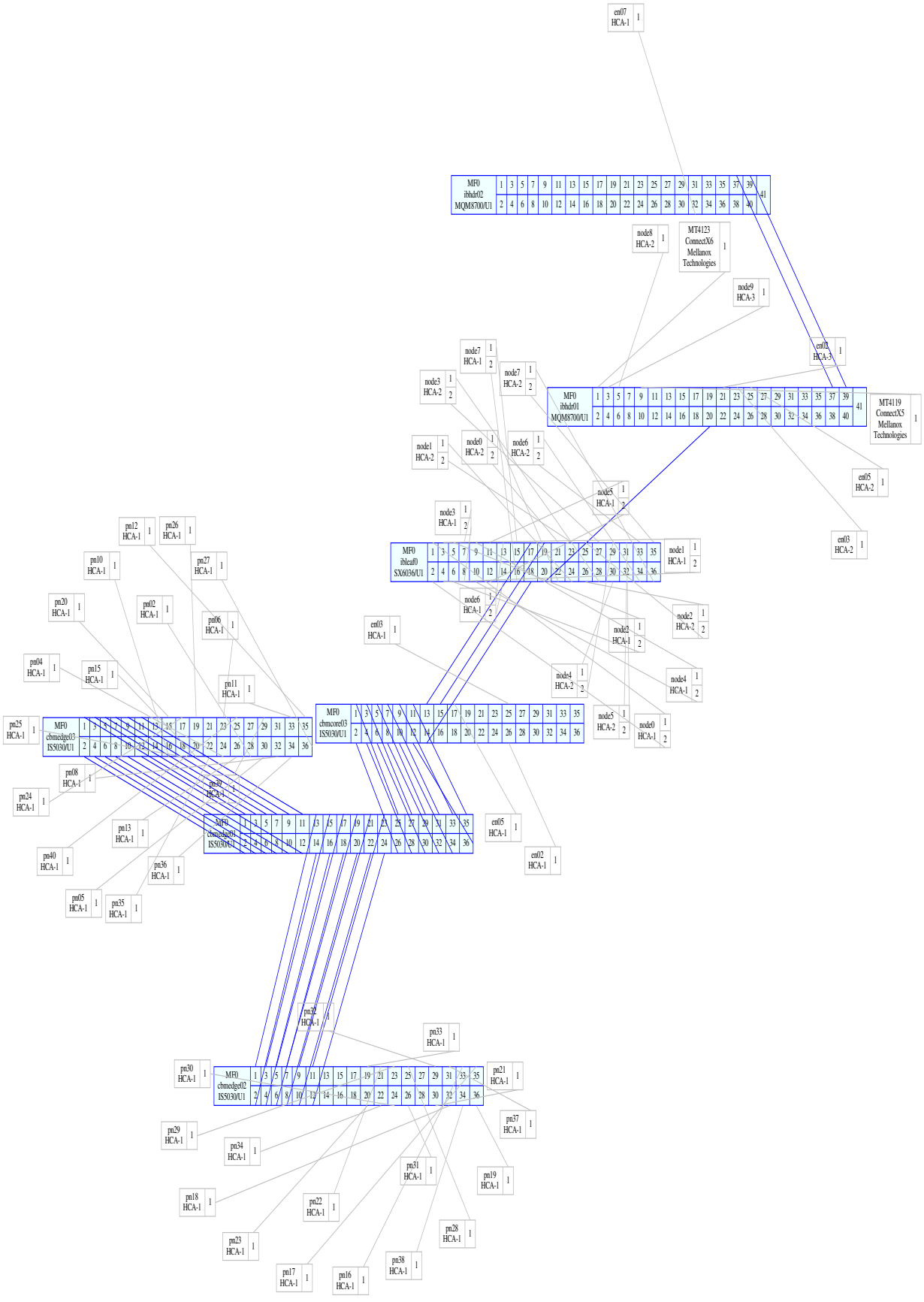

Figure A.1.9: Infiniband network topology for mCBM as of April 2020.

A.1.1 mTFC

The Timing and Fast Control for mCBM (mTFC) system will distribute timing and clock to all other subsystems in the experiment and provide the technical means for centralised experiment-wide low-latency control needed to ensure data flow integrity and consistency (e.g. for data throttling). The system will be built as a tree-like network of FPGA boards with fibre-based interconnections (see Fig. A.1.10). At the root of the network tree will be the mTFC Master node, running synchronously with the incoming master clock and distributing timing and control information through the hierarchy of intermediate nodes, mTFC Submasters, to endpoints – CRI boards acting as mTFC Slaves. As CRI boards contain extensive data processing logic, a mTFC Slave will be integrated in the processing firmware as an IP core, interfacing nodes with the rest of the mTFC network.

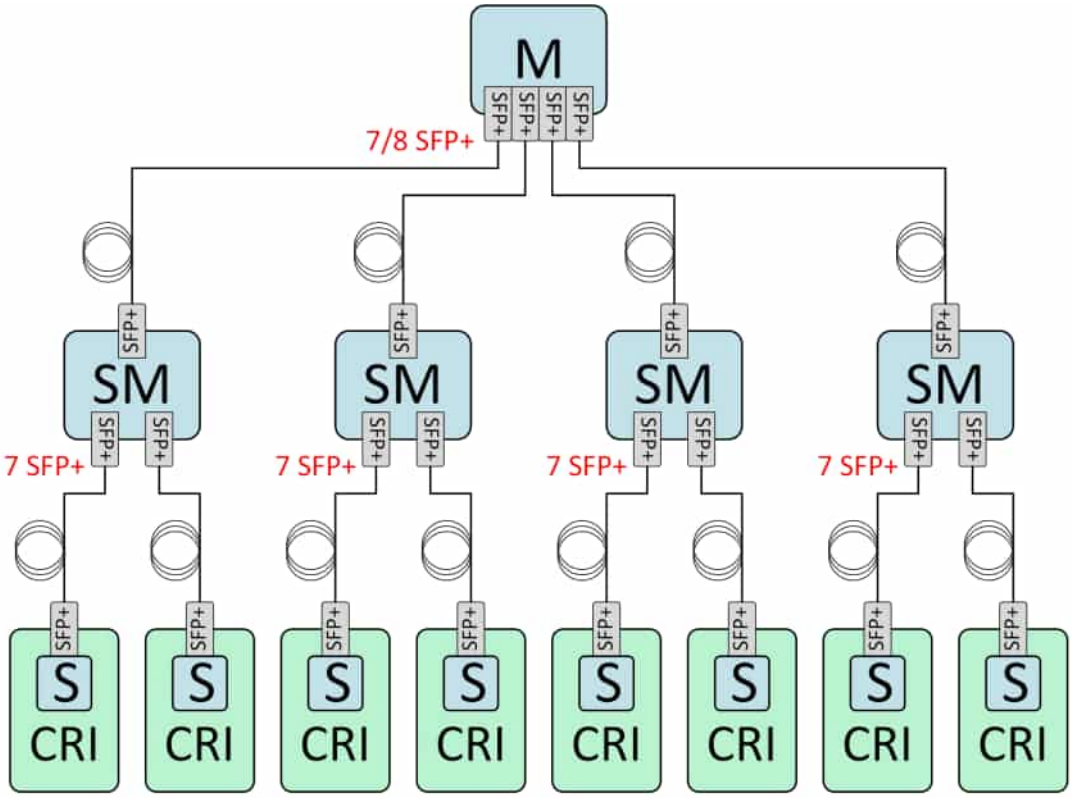

Figure A.1.10: Proposed mTFC network; M, SM and S are Master, Submaster and Slave nodes respectively. The number of link lines in the diagram is intentionally inaccurate to save space.

Master and Submaster nodes will be implemented on AMC FMC Carrier Kintex (AFCK) boards equipped with two Faster Technology FM-S14 cards each, providing SFP+ slots for 8 optical connections in total per board – either 1 upstream and 7 downstream connections or 8 downstream connections in the case of Master operation without a reference clock at the root node.

The mTFC system will provide synchronous clock and timestamp to online data processing boards – CRI, where this information will be used by subsystem-specific firmware to propagate synchronisation to the FEE layer. Timing information will be synchronised between mTFC layers with a negotiation routine on each mTFC link separately. The routine consists of two stages – syntonisation and synchronisation. This approach to individual link synchronisation enables the system for automated resynchronisation in cases of hardware fault or phase drift in the local clock.

A.2 Detector and Experiment Control System (DCS/ECS)

A.2.1 mDCS

The Detector Control System for mCBM (mDCS) will be based on the EPICS (Experimental Physics and Industrial Control System) which provides an architecture for building scalable distributed control systems. Each sub detector group will provide EPICS based individual Input Output Controllers (IOC) to access on one side the hardware sensors and actors to be controlled and monitored connected via field buses or LAN. On the other side those EPICS IOCs serve their obtained data, their process variables to the local network.

While the individual detectors provide the hardware access and infrastructure, the overall SCADA features including trending, archiving, and alarming can be centrally provided. As an option an additional separation level could be implemented to operate each detector in their own local networks, which themselves are accessed via gateways to filter data flow, control access and tune process loads. Only data needed for higher controls would then be provided via those gateways.

A.2.2 mECS

A prototype of Experiment Control System for mCBM (mECS) will be implemented based on State Machines in processes created by Python scripts. It should allow to find and implement the States, State transitions and Interfaces to other mCBM software necessary to provide the following functionalities:

- Reporting and monitoring of the State of each detector system in mCBM (including DAQ)
- Optionally: Reporting and monitoring of the current State of elements within a detector system
- Derivation of a global experiment State from the detector system States
- Run control (experiment-wide State transitions requests)
- Hardware state archiving and run relation (interface to mDCS)
- Firmware state archiving and run relation (interface to configuration and control software)

In a second phase, once the online analysis and selection software will be ready, support for the following States, State transitions and Interfaces will need to be added:

- Reporting and monitoring of the State of the online analysis processes (interface to mFLES process management)
- Reporting and monitoring of the State of the online analysis results (interface to online software or QA database)
- Online software high level control (State transitions requests to mFLES process management)
- Online analysis results archiving and run relation (interface to QA database)

B mCBM detector subsystems

B.1 mT_0

For the Time-of-Flight (TOF) based particle ID the reference timing is provided by the dedicated T_0 counter. The design goal for the time resolution of T_0 is 50 ps (including readout chain) based on the overall TOF resolution of 80 ps. The detector is necessary in the calibration/test phase of the TOF wall, while in high multiplicity events a software determination of T_0 will be carried out.

Figure B.1.1: The multi-segmented diamond plate of the T_0 counter.

The in-beam T_0 detector for the measurements with heavy-ion beams in the mCBM setup is constructed from an electronic grade polycrystalline diamond plate of 0.3 mm thickness (see Fig. B.1.1). A single plate of 20 mm x 20 mm is placed in a beam-pipe vacuum upstream from the target. The segmentation of the readout electrodes has two goals; (i) monitoring of the beam quality and position (detector is mounted in stationary position relative to the optical beam axis) and, (ii) that the peak data load on each channel can be processed by the readout electronics (digitizer). The first stage of the analogue front-end electronics is integrated on the PCB together with detector and high-voltage bias. The amplified signals are carried over a multi-pin vacuum feed-through connector to the outer part of the front-end electronics, where additional signal amplification, shaping and discrimination are taking place. The timing signals are processed with same kind of digitizers as TOF signals and they are synchronized to the same reference

clock. At high rates, the data overhead needs to be suppressed in conjunction with the data processing from the TOF wall. While the common clock guarantees the synchronization between both subsystems, the data throttling is independent, which can lead to unnecessary data loss.

object	number of GBTx	optical up-/down-links	duplex fibers	CRI
T_0 detector	2	$2 \times (1+1) = 2 + 2$	2	1

Table B.1.1: Required amount of CRI devices to interface the GBT links from the mT_0.

B.2 mMVD

B.2.1 Status of the CBM-MVD

The CBM Micro Vertex Detctor (MVD) will be operated in the target vacuum $5 - 20$ cm downstream the target. It has to reach a material budget of 0.3% and 0.5% X_0 for the first and the consecutive three sensor stations, respectively. The MVD will be formed from highly granular CMOS Monolithic Active Pixel Sensors (MAPS), which will be hosted on a cooling support made from highly heat conductive carbon materials (TPG, CVD-diamond). This support will drive the dissipated power of the sensors to liquid cooled heat sinks located outside the acceptance of the CBM experiment, which hosts also the PCBs of supporting electronics. The electrical contact between the sensors and the PCBs will be done by means of thin flex print cables.

To match their physics goals, the MVD sensors have to provide a spatial precision of 5 µm and a time resolution of 5 µs, which is to separate collisions at the envisaged average collision rate of 100 kHz Au+Au. Moreover, the MVD sensors have to resist a peak particle rate of up to 70 MHz/cm^2 and to withstand very inhomogeneous radiation doses peaking at 7×10^{13} n_{eq}/cm^2 and 5 MRad per year. Finally, they have potentially to tolerate the impacts of a sizeable number of nuclear fragments and heavy ions from target and beam halo, which may provoke harmful Single Event Effects (SEE).

To match those ambitious requirements, we are developing a next generation CMOS Monolithic Active Pixel Sensor named MIMOSIS. The ~ 5 cm^2 large and 50 µm thin sensor will feature 504 rows of 1024 pixels with a surface of 26.9×30.2 µm^2. Three buffer stages will flatten out the spatial and temporal occupancy fluctuations expected and reduce the peak data rate to 2.4 Gbps.

MIMOSIS forms a highly complex and radiation tolerant system-on-chip. The signals of minimum ionizing particles comprised of few $100\,e$ will be amplified and discriminated on the pixel itself. Hereafter, the data is concentrated by a multi-staged priority encoder. Internal digital data processing circuits will perform limited cluster finding, compress the data and translate it to a high level data protocol before sending it out.

The sensor is being designed to tolerate high integrated radiation doses. To improve its immunity to SEE, its steering logic is realized in triple redundant electronics, which is to compensate for possible bit flips as typically generated by the impact of heavy ions and nuclear fragments in CMOS electronics. Those functionalities are complemented by numerous test and self-diagnosis circuits.

A first small prototype, MIMOSIS-0, hosted mostly the complex pixels and the priority encoder used for reading them out. The prototype was successfully tested in the past two years[**?**]. The first full size prototype, MIMOSIS-1, hosts most features of the final design including the buffers and the related, complex steering electronics. The sensor was produced in May 2020 and will be subject of systematic tests in 2021. The results obtained from the test should help to improve the consecutive sensor MIMOSIS-2, which will also hosts additional digital electronics and should be tested in 2022. Among the key questions to be addressed are the immunity of the chip to heavy ion hits as experiences made in the past with elder sensors indicate both: That missing protection measures may turn into a rapid loss of sensors during operation and that adding those features may successfully prevent those losses[**?**]. The experiments proposed aims to obtaining quantitative SEE cross-sections and to spot possible weak points in the chip design.

In parallel to the development of the sensors, we continue the development of a dedicated mMVD module, which will be formed from 1+1, or 2+2 sensors (double-sided integration) with complete overlap, respectively, in order to allow for micro-tracking per station. This module will be equipped with a CBM compatible DAQ system, which shows additional complexity with respect to the lightwight system foreseen for the SEU-tests.

B.2.2 Goals of the mCBM experiments in 2021/2022

SEE in CMOS devices manifest themselves in different ways: Bit-flips in memory cells including the control registers of MIMOSIS may corrupt data but more importantly manipulate the configuration of the device until the mistake is corrected by re-initializing the register. Radiation induced glitches in the clock may desynchronise the numerous state machines of the chip until it is power cycled. So-called latch-ups create meta-stable short circuits, which may destroy the device thermally unless they are extinguished by means of an active power cycling. Finally, in case of highest energy transfers, irreversible ruptures of transistor gates may occur and destroy the device permanently.

The protective measures of the MIMOSIS-1 sensors to be tested include a triple redundancy of state registers and state machines, which should compensate individual bit flips in those units. Suited circuits in the biasing system will detect the over-currents generated by possible latch-up initiate a rapid power-cycling of the sensor. No protective measures are foreseen for data memories and to prevent gate ruptures. This is as individual bit flips in the data can presumably be tolerated while the vulnerability of the gates is a fixed property of the CMOS technology used for MIMOSIS-1. However, quantitative information on the energy thresholds and cross-sections for those kinds of events is crucial to estimate their impact on the total MVD design.

In the periode 2021/2022, a focus for mMVD will be laid on understanding quantitatively of the tolerance of the MIMOSIS-1 sensor to Single Event Effects (SEE) induced by heavy ion impacts. Moreover, we aim to identify and locate possible weak points limiting this immunity in order to eliminate them in the consecutive sensor prototype. The study will profit from the unique availability of heavy ion beams at GSI. They will be complemented by tests addressing the detection performances of the MIMOSIS-1 sensor for minimum ionizing particles and the sensors's tolerance to total ionizing and non-ionizing radiation doses. As they require high energy $\gtrsim 5$ GeV particle beams, the latter tests will be carried out complementarily to mCBM. Both test programs will rely on a lightweight stand-alone DAQ and sensor integration. The preparation of mCBM compatible mMVD modules will be followed up in parallel and is not expected to conclude within this beam period.

The tests will be performed by illuminating the running sensor with heavy ions. A defined data content will be stored in the state registers and data memory cells and read continuously back from the sensor. Any bit-flip will be recognized by scanning for discrepancies between the intended and real content of the returned data. Selected, representative state machines were equipped with a diagnostic output and feature moreover a counter, which indicates the number of successfully corrected bit flips. Both features should allow to estimate the number of successful and non-successful SEE corrections. Latch-up events will be recognized by the over-currents detected by the related protection circuits and by counting the power cycles initiated. At present, it is not known if gate ruptures will occur. If so, they will manifest themselves as permanent damage of the sensor, which may be spotted based on searching for permanent over-currents, faulty data and non-recoverable losses of synchronization.

B.2.3 Choice of beam lines

According to our present understanding, the MVD running under standard conditions will be exposed to heavy ions from two sources. The presumably dominant source will be relativistic heavy ions from the halo of the primary beam. Moreover, the MVD might be hit by slow, heavy target fragments. At the time given, no quantitative information on the intensity and composition of both sources is available. However, first results of ongoing simulation studies suggest that an impact of heavy target fragments, despite not excluded, forms a rare event. We anticipate that MIMOSIS-1 should tolerate impacts of relativistic heavy ions from the beam halo mostly without interrupts in its operation. The more harming target fragments, which

impinge at Bragg peak energies, should be tolerated without permanent damage. Based on this consideration, we propose to subdivide the tests into three blocks:

- A test with relativistic ~ 1 AGeV heavy ions as available at the beam dump of mCBM will model the frequent case of a relativistic beam halo ion impinging the MVD. A quantitative understanding of the cross-sections for SEE generated by this beam is required to judge if the present MIMOSIS-1 design is suited to ensure a stable MVD operation in the presence of beam halo.
- Testing sensors with ~ 10 AMeV ions at the UNILAC X0-beam line will allow to understand the impact of possible slow and heavy target fragments with Bragg-peak energies on the MVD. A focus will be laid on understanding the energy threshold for possible irreversible damage like transistor gate ruptures.
- In case the immunity of MIMOSIS-1 to reversible SEE is not yet found satisfactory, scanning the sensors with the ~ 10 AMeV micro-beam of the µX0 of the UNILAC will allow to locate possible weak points in the design of MIMOSIS-1. It is considered that once the location of sources of bit flips, clock instabilities and latch-ups are known, they can be eliminated by modest design modifications.

B.2.4 Technological implementation and beam time estimates

Estimating the beam times needed for the tests proposed is difficult as the cross-sections of SEE in MIMOSIS-1 are a priori unknown. This holds despite unpublished previous tests carried out with the ALPIDE sensor provides some qualitative input, which will be exploited for the test preparation. Our beam time estimates start from the assumption that the sensors of the MVD should not show more than one soft error per hour, which forces the need for an unscheduled restart of the sensor and the related need to resynchronize the MVD-DAQ. Assuming moreover that the MVD is composed of ~ 250 sensors with 5 cm^2 surface and that the maximum beam halo rate reached within the MVD specification amounts 1 kHz/cm^2, one concludes that the experiment should be suited to measure SEU cross-section down to $\sim 10^{-10}$ cm^{-2}. On the other hand, it appears reasonable not to overload the sensing part of the chip as this might turn into a saturation of amplification structures. It is not excluded that this might modify the electric fields and power consumption of the device and such bias the results. This consideration and the need to perform dosimetry suggests that the illumination should remain below ~ 1 MHz/cm^2. In consequence, one expects that the test of a specific structure will require $\sim 10^4$ s beam on sample. Given the duty cycle and the number of the structures to be tested, one ends up with a beam time requirement of about five days per beam line excluding the time needed for setting up and testing the installation.

B.2.4.1 Tests at mCBM The experiments in the mCBM beam line will form the backbone of the proposed test program. The sensors will be operated near the beam dump and thus exposed to a about 3 cm wide beam spot. The sensor will be operated consecutively in the beam in a test mode. In this mode, the configuration registers and data memories of the sensor will be filled with well defined data patterns, which are readout continuously. Any mismatch between the expected and the observed data pattern is interpreted as SEE-effect and the number of the mismatches is counted. In parallel, the synchronization of the internal sequencers of the sensor with respect to an external sequencer running on the same clock is supervised. Complementary to this, an internal self-testing circuit of this central instance of the sensor will provide the number of bit flips, which were corrected by the triple vote. Monitoring the biasing currents of the sensor will allow to detect the over-currents generated by latch-up. No gate rupture is expected at this energy.

The number of recognized SEE will be compared with the number of ions penetrating the sensor. As previously done in tests performed at the CERN-SPS [**?**], a dosimetry based on a fast scintillator of the size of the chip and with PMT readout will be used to count the ions. This system will be operated at a sufficiently low PMT-voltage to become blind to charged particles as backscattered from the beam dump. The stand-alone dosimetry is to complement the beam diagnostic detectors, which may however by themselves provide the moderate counting accuracy targeted.

As the test installation required for the proposed test program is independent from the mCBM experiment, tests may be carried out stand-alone as much as in parallel to the regular mCBM operation. We anticipate that a total of two weeks of beam time should be considered for performing the full test program including setting up and testing the system. A majority of this beam time may be carried out together with the other mCBM detectors provided that the beam intensity can be matched. Preferably, very heavy ions (e.g. Au) near the SIS18 top energy should be used.

B.2.4.2 Tests at X0 The proposed experiment aims to estimate the LET-threshold for possible irreversible damage. To do so, it is proposed to decelerate heavy ions in air such that the vulnerable structures of MIMOSIS-1 are hit by ions on the falling slope of the Bragg peak. By moving the sensor in beam direction, the LET may be modified. Non-conclusive observations made in earlier studies suggest that irreversible damage may occur for projectiles with a charge including and beyond Xenon. It is therefore proposed to exercise the experiment with a medium size ion before approaching highest LET values with dedicated heavy ion (e.g. Au) - beams. The consequences of individual gate ruptures in MIMOSIS-1 are hard to predict. However, it is considered that the above mentioned surveillance systems will be suited to register them as non-recoverable error.

Dosimetry beyond in-beam instrumentation is difficult at the X0 beam line as the low energy projectiles get stuck in the sensors. Conceptually, one may consider to use the sensor itself as a dosimeter as it is sensitive to heavy ions. However, the study aims rather at learning, if gate ruptures occur at all and at coarsely identifying the related SEU thresholds. Both can be carried out without precision dosimetry. Instead, TRIM [**?**] simulations based on the known geometry of the sensor structures will be performed in order to estimate the LET in a given depth.

B.2.4.3 Tests at µX0 The targeted tests at µX0 have to be performed with medium size ions, which provoke a maximum error rate without destroying the samples. Moreover, one has to spot candidate locations for weak design points in the sensor prior to the beam time. Obtaining this information requires a careful analysis of the data obtained from the previous tests. Due to the limited beam intensity of µX0 and the need to raster scan the 5 cm-sensor, the tests may require a substantial time. As the experiment aims for spotting the location of weak points rather than for estimating cross-sections, no dosimetry beyond the beam instrumentation is required. Instead, a careful spatial alignment of the device under test with respect to beam is required. It is considered that a well prepared test for a limited amount of identified candidates for weak points may be carried out within five days.

B.2.5 Status of the beam time preparations

The preparation of the experiment will be carried out based on first experiences made by illuminating MIMOSA-26 sensors to a 30 AGeV-Pb beam at the CERN-SPS. The latter test convinced us that MIMOSIS-1 will survive impacts of relativistic Au-ions without irreversible damage, which forms a prerequisite for the tests in the mCBM cave.

The MIMOSIS-1 sensor will return from production end of Q2/2020 and needs to be carefully tested before performing the experiments proposed. The design of the necessary test infrastructure is ongoing at the IPHC Strasbourg, the Goethe University Frankfurt am Main and GSI based on the experience with numerous previous sensor generations. This preparation work includes in particular the construction of a slow control interface for reading and writing the memory registers of sensor, which is well advanced. Moreover, a dedicated proximity board, which is to hold and bias the sensor, has to be prepared as the standard solution is neither optimized for the heavy ion tolerance nor for the vacuum tolerance required for operating the sensor in the µX0 beam line. This topic will be solved based on the experience made with the vacuum compatible detector prototypes for the CBM-MVD, which were designed from the start to match both requirements.

It is expected that the necessary preparation work including the necessary test of the sensors and building the necessary software tools can be carried out until Q1/2021.

B.3 mSTS

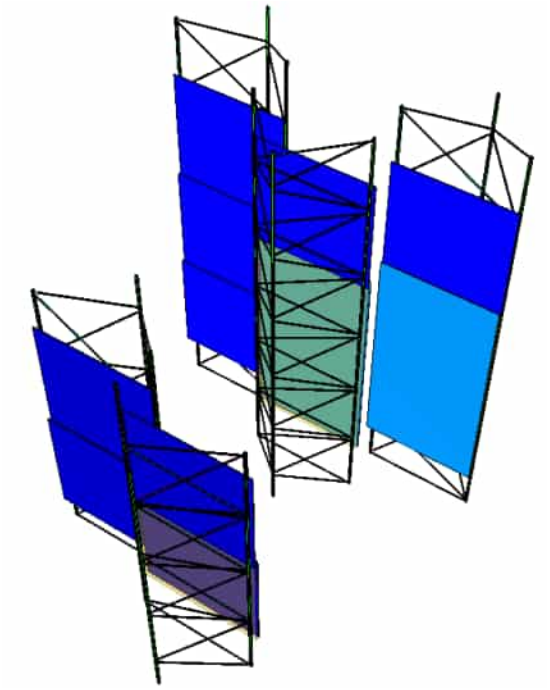

Figure B.3.1: CbmRoot geometry of the mSTS subsystem. The target is to be imagined on the left hand side of the first, smaller station. The sensors dimensions are 6 by 6 cm (dark blue, back side dark gray) and 6 by 12 cm (light blue, backside light gray), and shown attached to carbon fiber support structures.

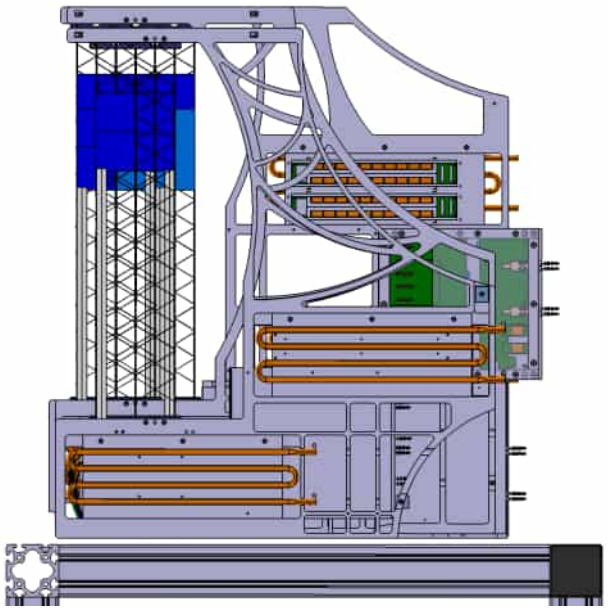

Figure B.3.2: CAD design of the four C-frames in mSTS, populated with detector ladders, cooling plates, powering electronics and further infrastructure. View downstream.

B.3.1 Overview

The mSTS detector is a demonstrator of the full Silicon Tracking System, focusing on proving with final or near-final components selected aspects of the full detector system to be constructed:

- foremost the basic functional unit of the STS, the detector module:
  - full integration of the module components (sensors, microcables, read-out ASICs, front-end board) during module assembly;
  - the module operation, i.e. powering, configuration, read-out, noise and signal levels, data integrity and data rates;
- several mechanical aspects:
  - mounting of modules onto carbon-fiber carriers, the ladders;
  - integration of the ladders onto the mechanical C-frames, carriers of the units;
  - cooling of the front-end electronics through several thermal interfaces by a liquid cooling system;

- low and high voltage supply and its distribution;
- read-out through the CBM prototype data-driven acquisition chain;
- stability of operation in terms of operating time, any possible interferences with other systems, and conditions up to high beam-target interaction rates.

The mSTS has been conceived to comprise two tracking stations, 0 and 1, covering the angular acceptance of mCBM ($\approx 13.0^\circ < \theta < 37.0^\circ$) to the right side of the beam axis. Several mechanical or conceptional simplifications have been deliberately applied in order to facilitate focusing on the core questions of module operational stability and read-out. The tracking stations are realized on two and three half-ladders, comprising two and three detector modules each, covering areas of 12 by 12 cm^2 and 18 by 18 cm^2. The ladders are arranged single-sided on four mechanical structures, the C-frames, somewhat differently but easier to realize than in the later full STS with its two-sided attachment of ladders to C-frames. Also, the cooling is restricted to water cooling of the front-end electronics. The sensors are operated at ambient temperatures, without additional cooling, as no long-period radiation accumulation will happen in mCBM. Therefore the mSTS enclosure fulfills purely mechanical and electromagnetic shielding purposes, and no thermal insulation aspects are addressed.

The arrangement of sensors on ladders to form the two tracking stations is shown in Fig. B.3.1, which depicts the simulation geometry in CbmRoot, and in Fig. B.3.2 with details of the CAD design.

Figure B.3.3: STS detector module comprising a double-sided silicon microstrip sensor, front-end electronics and a read-out microcables between the sensing and electronics parts. The top and bottom shielding layers are not yet attached.

B.3.1.1 Modules Every module comprises a double-sided silicon microstrip sensor with outer dimensions of 6.2 cm by 6.2 cm or 6.2 cm by 12.4 cm, segmented into 1024 strips per side. The strip pitch is 58 microns and the strip orientation is under 0 degrees (parallel to the ladder) and 7.5 degrees on the front and back side of the sensor. A prototype module is shown in Fig. B.3.3.

The modules with their 11 microstrip sensors present 11 x 2048 read-out strips and thus in total more than 22 thousand read-out channels, involving 176 STS-XYTER front-end ASICs. The front-end electronics boards will be attached to water-cooled plates to remove the dissipated power. Power-supply boards (POB) and readout boards (CROB) will be mounted in the vicinity of the

stations. The two stations will be housed in a box shielding against light and electromagnetic radiation, using a low-mass beam window. Inside of the box, the sensors are operated at ambient temperature.

B.3.1.2 Ladders The detector ladders are "half-ladders", i.e. from the emerging STS construction, that are cut in the middle and populated with two or three detector modules only, instead of possible five. The length of the carbon fiber support structures will be shorted accordingly. The three variants of mSTS ladders are schematically shown in Fig. B.3.4. Two of them, each comprising two detector modules, will form the first tracking station when mounted top-down onto a mechanical frame with a little lateral overlap. Three additional half-ladders, carrying two or three detector modules each, are to build up the second tracking station.

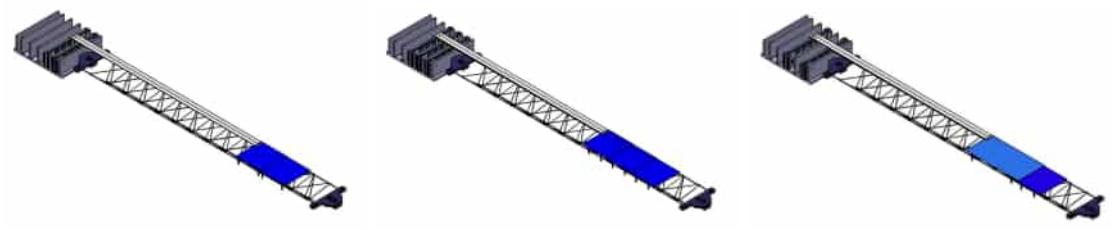

Figure B.3.4: CAD view of the three types of mSTS detector ladders, populated with either two or three detector modules. Left: Two modules with a 6 by 6 cm^2 sensor. Middle: Three modules with a 6 by 6 cm^2 sensor. Right: One module with a 6 by 6 cm^2 sensor, one module with a 6 by 12 cm^2 sensor. In the engineering drawings, the silicon sensors mounted on the carbon fiber supports are shown, as well the front-end electronics boards installed in cooling shelves. Only a fraction of the interconnecting microcables are displayed.

B.3.2 Present status

During the start-up at the end of 2018, and in the 2019 running, mSTS comprised one C-frame with one detector ladder with two modules using the latest frontend ASIC version 2.1 installed. It was experienced that one assembly step in the module construction, namely the necessary coverage of the STS-XYTER ASICs with "glob top" resin to protect the electrical wire bonds from mechanical damage, resulted in thermal stress during operation of the modules that destroyed critical power or communication bonds and made a good fraction of the ASICs non-operational. In spring 2019, a detailed analysis of the problem was made and a different, more plastic, glob top material used. A dedicated in-beam test of a module in a mSTS set-up was carried out in November 2019, in beam at the COSY accelerator, Research Center Jülich, Germany. It confirmed not only that the module was fully electrically operational, but also that it met the specifications in terms of system noise (ENC $\approx$ 1000 e^-), time resolution and further tracking related parameters. The C-frame was later installed in the mSTS box fitting the mCBM beam table and environment and run in the November 2019 mCBM campaign. Also there the detector worked fully, however was subjected to a 8.3 kHz noise that has been present since then; it is subject of detailed investigations. For the mCBM running from March to May 2020, a new ladder with two newly prepared modules was mounted and operated on station 0. The detector is shown in Fig. B.3.5.

B.3.3 Completed system

The detector will be completed for the run in 2021 to the design in Figs. B.3.1 and B.3.2. A further half-ladder with two 6 cm by 6 cm sensor modules will be installed on a new C-frame 0,

Figure B.3.5: Left: STS assembled in the integration laboratory, with the back-cover opened. Right: mSTS installed on the mCBM beam table in March 2020.

one half-ladder with one 6 cm by 6 cm sensor module and one 6 cm by 12 cm sensor module on a new C-frame 2, and two half-ladders on a new C-frame 3, one with three 6 cm by 6 cm sensor modules and the other with one 6 cm by 6 cm sensor module and one 6 cm by 12 cm sensor module. This work is currently ongoing, the mechanical C-frames have been prepared already, modules are being assembled, the ladder integration is to be resumed after a break due to the coronavirus pandemic and overnmental imposed distancing – ladder assembly is a many-hands, non-automated work, where close human contact is unavoidable.

B.3.4 Read-out chain

The mapping of the STS ladder front-end electronics to the readout hardware is summarized in Tabs. B.3.1 and B.3.2. The FEB-8x1 are equipped with 8 STS-XYTER ASICs and utilize 1 e-link per STS-XYTER, summing up to 8 e-links per FEB-8x1. Since each sensor has 1x n-side FEB and 1x p-side FEB, 16 e-links need to be readout for a single sensor. A ROB-3 is equipped with 3 GBTx ASICs and provides connectivity for 42 readout e-links. The optical connection of the ROB-3 is handled with 1 down- and 3 uplinks, occupying a total of 3 Multi-Gigabit Tranceivers (MGT) on the CRI.

In station 0 and in the unit 2 of station 1, each ladder consisting of 2 sensors can be readout with a single ROB-3, see Fig. B.3.6 and Fig. B.3.7. However in station 1 unit 3, the ladders are equipped with 2 and 3 sensors, respectively, and thus would require 32 and 48 e-links, respectively, the latter being too much for a single ROB-3, see Tab. B.3.1. Therefore this unit will be equipped with 2 ROB-3s, one of them for the 32 e-links from the ladder with two sensors and 8 e-links (one FEB-8x1) from the ladder with 3 sensors. The number of CRIs required to interface these 5 ROB-3 is shown in Tab. B.3.2. Each CRI is offering 24 optical ports. To read out the full mSTS in 2021 with 11 sensors, 5 ROB-3, 15 duplex fibers and 1 CRI are required.

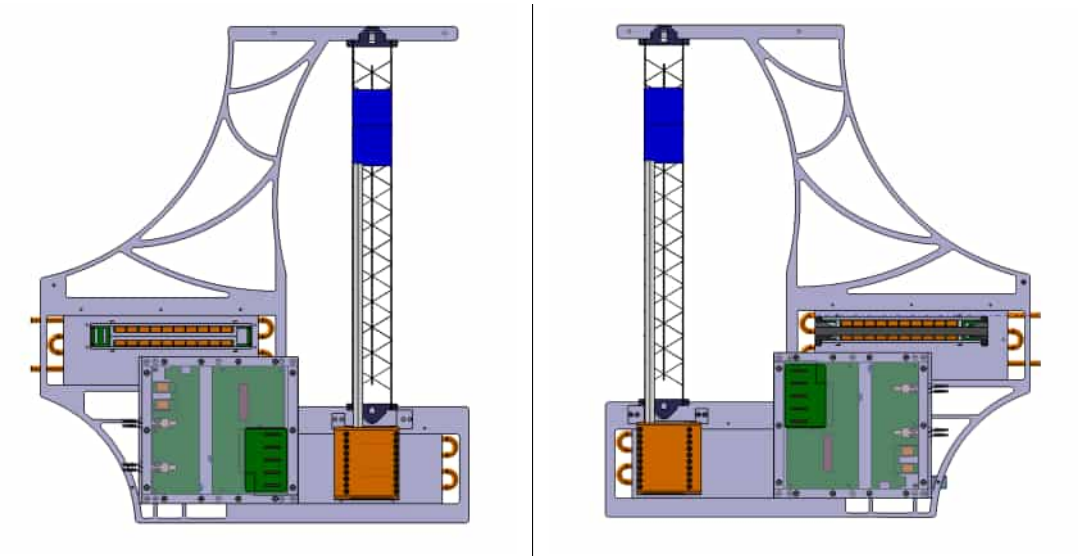

unit 0 unit 1

station 0

Figure B.3.6: CAD drawing of the mSTS units in station 0. The green objects are the ROBs.

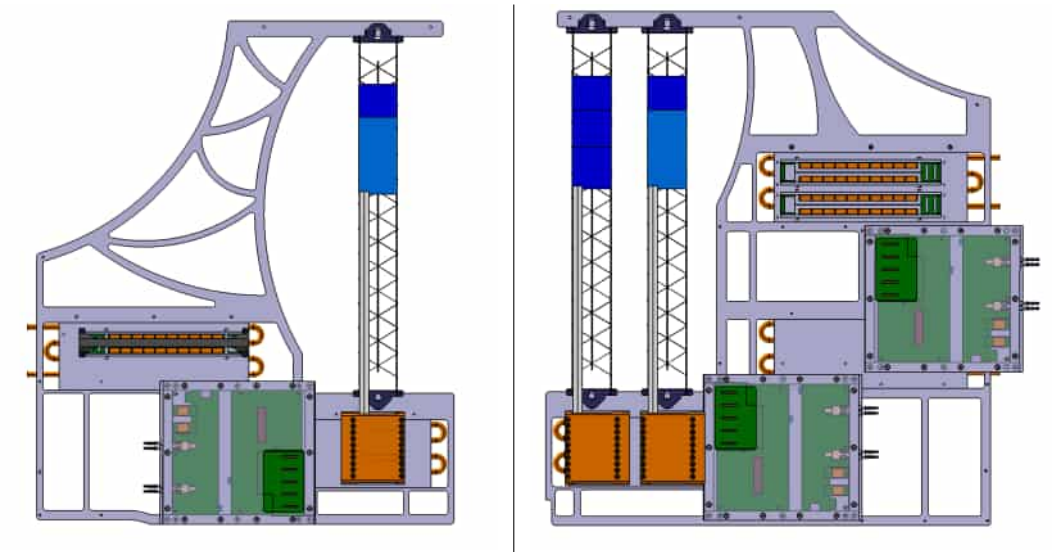

unit 2 unit 3

station 1

Figure B.3.7: CAD drawing of the mSTS units in station 1. The green objects are the ROBs.

Table B.3.1: Amount of FEB-8x1 and GBTx ROB-3 required to read out the mSTS.

object	number of FEBs	e-links on FEBs	number of ROBs	e-links on ROBs	e-links unused
C-frame 0	4	4 x 8 = 32	1	42	10
C-frame 1	4	4 x 8 = 32	1	42	10
C-frame 2	4	4 x 8 = 32	1	42	10
C-frame 3	10	10 x 8 = 80	2	2 x 42 = 84	4
total	22	176	5	210	34

Table B.3.2: Required amount of CRI to interface the GBT links from the mSTS.

object	number of ROBs	optical up-/down-links	duplex fibers	CRI-24
C-frame 0	1	1x (3+1) = 3+1	3	1
C-frame 1	1	1x (3+1) = 3+1	3	same
C-frame 2	1	1x (3+1) = 3+1	3	same
C-frame 3	2	2x (3+1) = 6+2	6	same
total	5	15+5	15	1

B.3.5 Detector control system

A prototype version of the Detector Control System (DCS) for the mSTS was tested during the mCBM campaign from March to May 2020. The system was designed to collect experiment and control data in real-time being published by Input/Output Controllers (IOCs). Values of process variables defined in IOCs are being stored in PostgreSQL and MySQL databases and their status is being constantly monitored for any alarm events. Any changes appearing in the Alarm System are also being logged. Figure B.3.8 presents the current status of DCS development. All the important components of the system are located in the multi-container docker-compose application (Control System Studio, Archive Engine, databases, Alarm Server, Elasticsearch, Kibana, MPOD IOC, Lauda IOC).

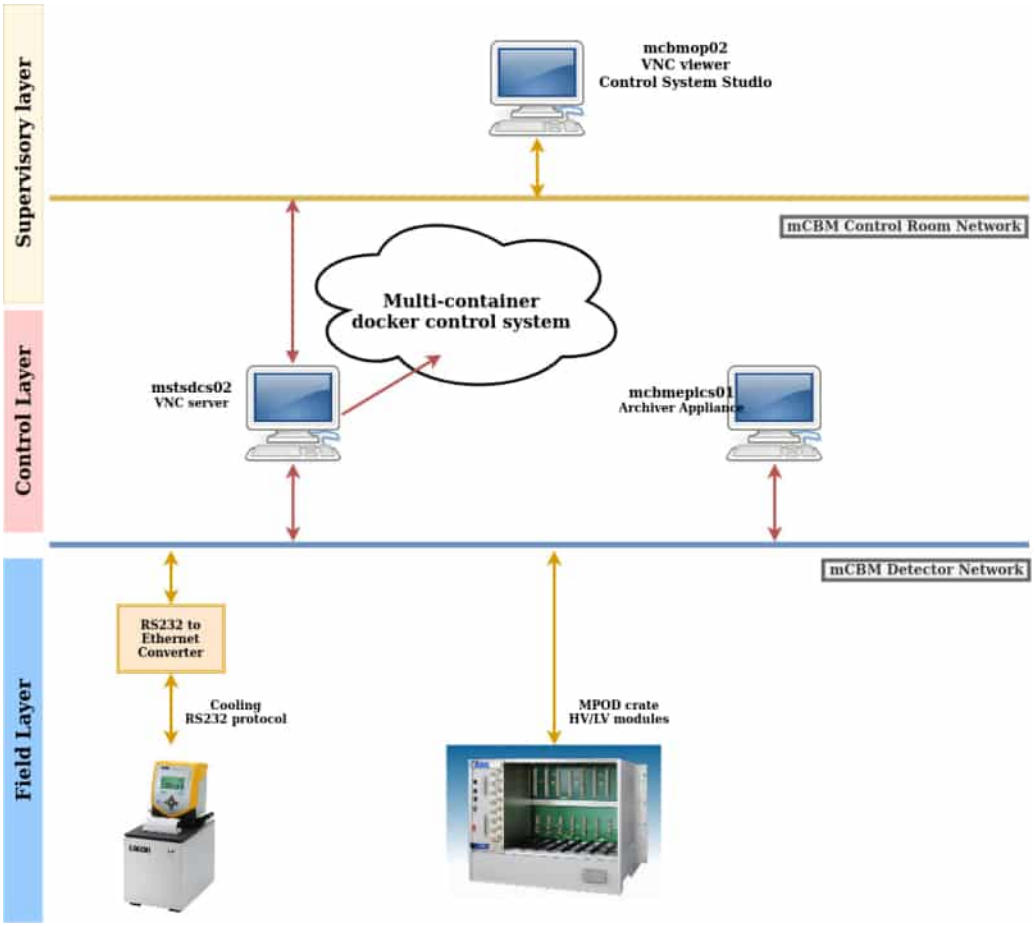

Figure B.3.8: Architecture of the DCS for mSTS in mCBM.

During the mCBM campaign, the DCS operated without issues for the whole period. Nevertheless, for 2021, the stability and performance of the DCS is expected to be further improved, with particular emphasis on system configuration. Figure B.3.9 describes the behavior of the sensor during one of the days with beam presence at mCBM. The values clearly indicate silicon sensor current dependence on the beam intensity, as well as on the spill length.

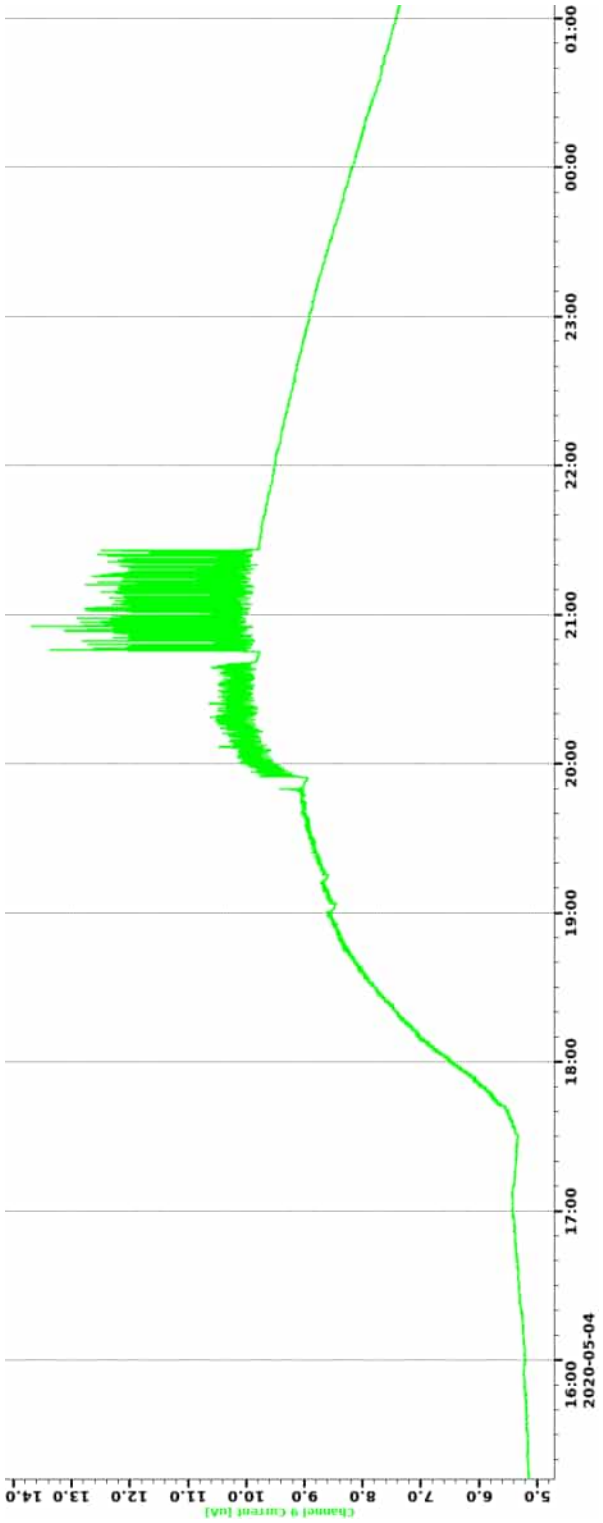

Figure B.3.9: Currents as a function of time stamps (UTC) in a mSTS module for one beam day.

B.3.6 First detector-specific results from commissioning

During mCBM running from March to May 2020, mSTS was permanently operational over a period of 47 days. All 32 front-end ASICs were functional up to the end of the beam time, confirming the reliable operation with the new "glob top" resin.

In the course of the beamtime period, a new firmware was commissioned with improved hit sorting and buffer sizes, which allowed to reliably read-out mSTS up to the highest beam intensities.

During the beam campaign we varied conditions of beam intensity. Figure B.3.10 shows data rates as a function of time-slices (TS), given in number of recorded signals in the whole detector per time-slice for different beam intensity and target thickness. The beam spills and the spill structure of the accelerator, followed by a short break, can be clearly identified. The rates during the off-spill breaks remain constant, while during on-spill the rates increase following the increased beam intensity. At the highest intensities, the rate scales less than from the intensity increase as only one out of the maximum 5 read-out links per ASIC were connected through the STS front-end electronics boards to the acquisition system. The scaling from thin to thick target is also being investigated.

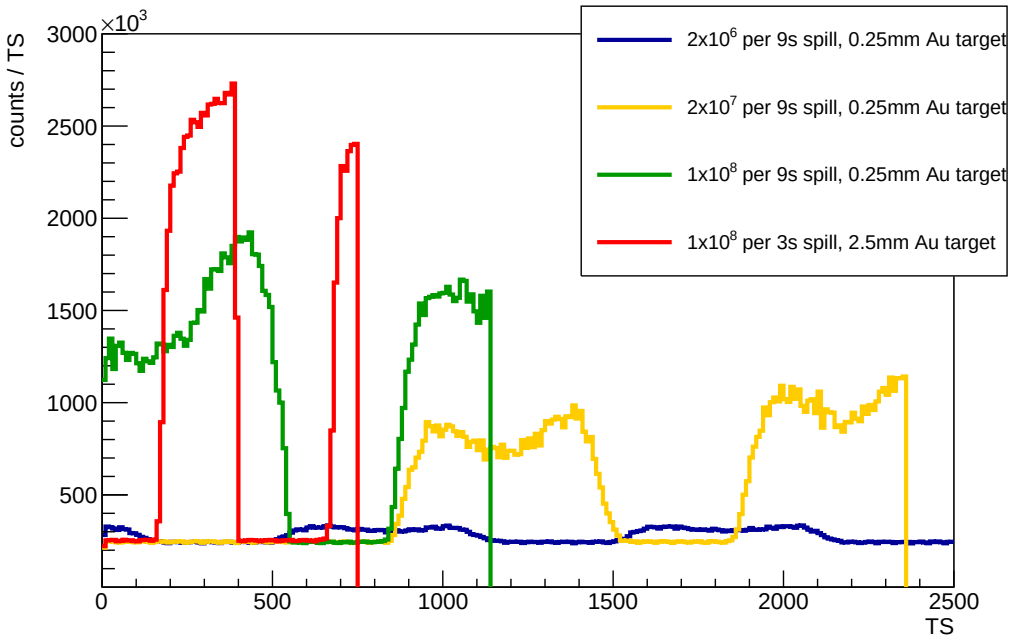

Figure B.3.10: Rates of STS data as function of time-slices, for a number of accelerator spills at various beam intensities and two target thicknesses.

The targeted STS system noise of around 1000 e^- ENC was demonstrated during detector commissioning in the assembly laboratory at GSI before the beamtime (see Fig. B.3.11). On both the p- and n-sides, one ASIC was excluded from the measurement. The first ASIC on the p-side shows higher noise since it is connected to the split tilted strips which have a higher capacitance due to the interconnection lines on the second metal layer.

The measured signal is shown in Fig. B.3.12 illustrating the channel distribution for one module: the red vertical lines separate the eight read-out ASICs, i.e. 128 channels, while the thick line in the middle of the histogram separates the p- and n-sides of the detector. During the beamtime, all ASICs were functional, in both modules, and only few broken channels are visible. The other panel of the figure shows the signal charge distribution in ADC units for all

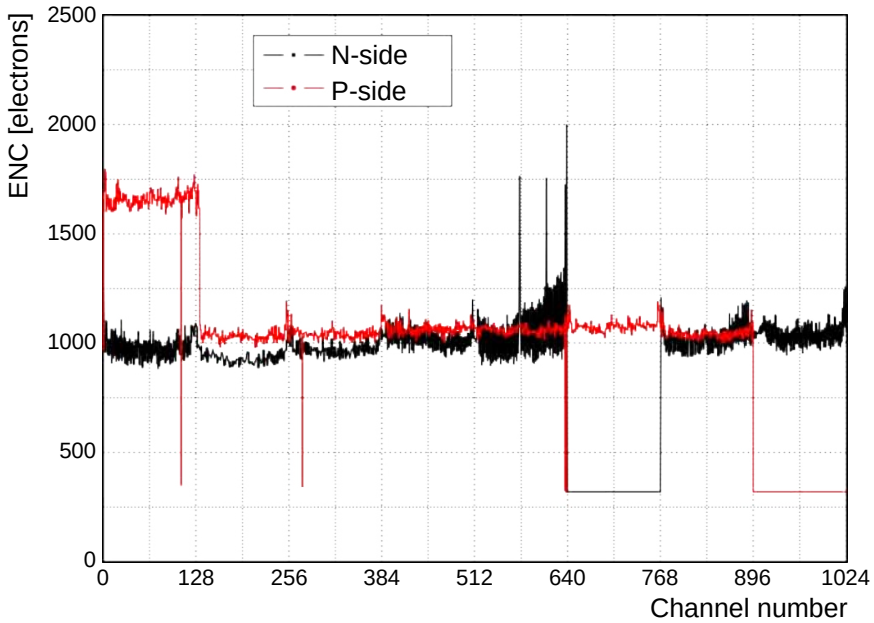

Figure B.3.11: Noise in the channels of the module, given in units of electron charge. The measurement was done applying internal test pulsers in the ASICs, and subsequent calibration.

the channels of the first module. Detailed analysis of the data taken is in progress to yield robust signal calibration and thus the signal-to-noise ratio.

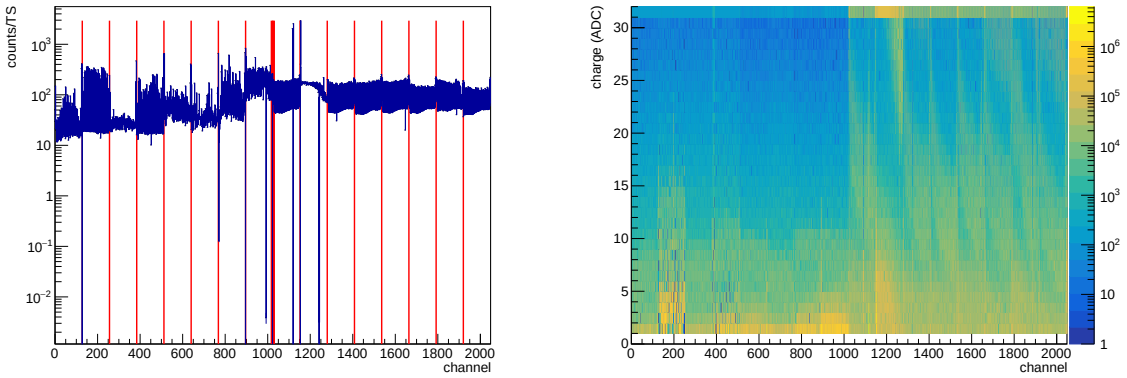

Figure B.3.12: Channel count distribution of one module (left), and signal charge distribution in ADC units before calibration (right).

The time calibration was done identifying a peak in the correlation with the T0 detector, i.e. t_{T0} - t_{STS}. The correlation is studied as a function of charge, for all ASICs separately. Figure B.3.13 shows the time difference t_{T0} - t_{STS} as a function of the signal charge in one typical ASIC. At high charge, above 20 ADC units, the peak is very sharp, indicating a time resolution better than 5 ns; at low charge the effect of the time-walk is visible and leads to a broadening of the peak and a shift towards later signal. All ASICs show the same time synchronization. Moreover we did not observe any time-jumps indicating sudden changes in the time synchronization, as observed previously, thanks to improvements of the sorting buffer and algorithm in the DPB firmware.

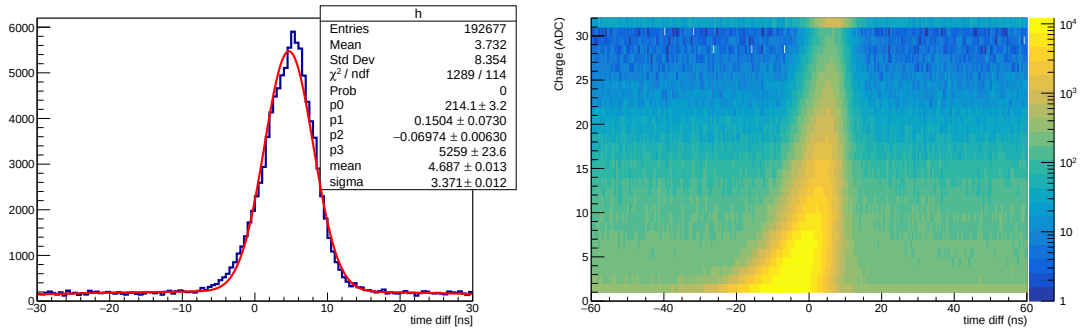

Figure B.3.13: Time difference between data ("digi") of STS and T0, as a function of the signal charge for one typical ASIC. The right panel shows the time difference only for signal with charge larger than 20 ADC units.

The reconstruction proceeds with the correlation of neighbouring signals (clusters) within a time window of 20 ns. In order to improve the signal-to-background ratio, the time difference of signals in 2-strips clusters, shown in Fig. B.3.14 is studied. The distribution shows a time resolution of few ns, in agreement with the conclusion from the correlation with the T0 detector. This is an excellent resolution, considering that walk correction - which reaches about 20 ns for low charge signals, has not yet been applied.

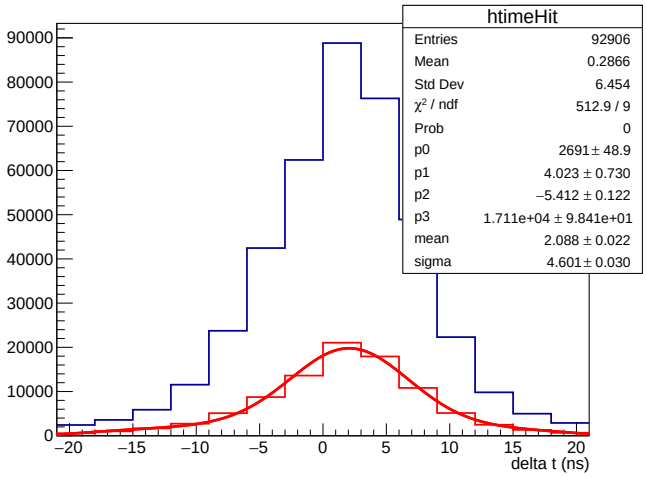

Figure B.3.14: Time difference of digis of 2-strip clusters (p-side: red, n-side: blue). The bin size is 3.125 ns. No time-walk correction has been applied yet.

Finally clusters in the p- and n-side are correlated to form hits. Taking advantage of the excellent time resolution, a time window of 20 ns has been used for the selection. The hit positions from the STS modules are presented in Fig. B.3.15. With the upper module, every second (even) channel on the p-side was turned off due to high noise. Also a few broken channels are visible.

Detailed analysis is in progress to evaluate the performance of the STS detector, in terms of signal-to-noise and efficiency and to study the space and time correlation of the STS data with the other detectors of the mCBM setup.

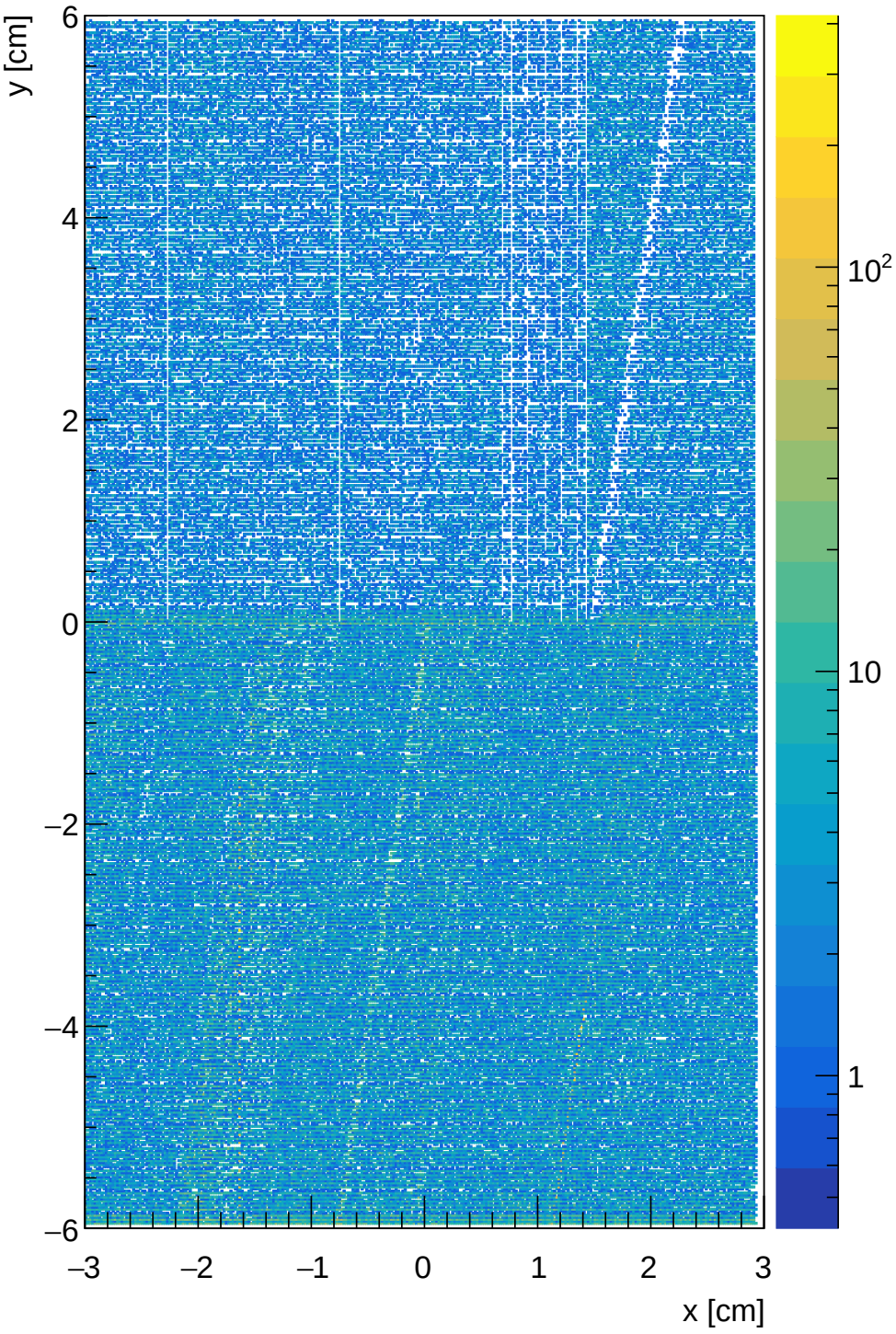

Figure B.3.15: Reconstructed hit maps in the two STS modules.

B.4 mMUCH

CBM Muon chambers (MuCh) for SIS-100 consists of hadron absorbers divided into five segments. The first absorber segment is made of graphite-concrete combination of total 60 cm thickness which is partially positioned inside the CBM-magnet and four other segments are made of iron of 20 cm, 20 cm, 30 cm and 100 cm thicknesses as positioned downstream the target. Four detector stations each of which arranged in triplets of layers and sandwiched between each absorber pair, except the fifth station are for registering the passage of particles through them. Particle density calculated for Au+Au minimum-bias collisions at 10 AGeV decreases radially and also along the beam direction. The maximum particle density averaged over three detector layers in a station and close to the beam pipe is 200 kHz/cm^2, 13.0 kHz/cm^2 and 4.7 kHz/cm^2 for the 1^{st}, 3^{rd} and 4^{th} stations respectively. It is therefore important that the detector technology handles the estimated flux. Based on the literature and other considerations, it has been decided to use triple-GEM chambers for the first two stations and single-gap RPC for the last two stations. The TRD layers of CBM positioned after the 5^{th} absorber segment is to be used as the 5^{th} detector station of MuCh.

B.4.1 mMUCH setup

Figure B.4.1: Two GEM chambers in the mini-CBM setup

In the mini-CBM first phase, we installed two GEM chambers as shown in the setup in Fig. B.4.1. The chambers have following features:

- The sector-shaped triple-GEM chambers are of the same dimension as required for the 1^{st}st MuCh station. The chambers were placed to have a maximum overlap with other detectors like STS, TRD, TOF in the mCBM setup.

- Each chamber had a 10 mm thick Aluminium cooling plate that had 6 mm Aluminum pipes laid out inside it in a spiral manner, through which cold water flows. The perforations were to facilitate attaching FEBs to the chamber.

- We used STS-XYTER-2.1 based readout FEBs as will be used in the final CBM setup. Each chamber had the provision of reading with a maximum of 18 FEBs, however, due to resource limitations, we could not populate the chambers in the first phase of the run upto the full capacity.
- Rest of the readout chain used DPB, FLIB and FLES same as used by other detectors in mCBM and similar to that to be used in CBM.

Main motivations of taking data with these two chambers at mCBM were as follows:

- Test the chambers with full DAQ and control systems as of main CBM
- Operate the chamber with optimum noise performance so as to make use of the available bandwidth of STS-XYTER.
- Obtain time and spatial correlations of the chambers between each other and with other detectors in an environment of high energy heavy ion collision at high interaction rate.
- Test the rate capability and radiation tolerance of the chambers
- Obtain tracking capability of the setup using mSTS. mMUCH, mTOF and other detectors.
- Operate the chambers with HV, LV and other services with a configurations close to that in the main CBM.
- Include mMUCH hits in mCBM track reconstruction and other studies

B.4.2 mMUCH results

In total we have collected data during the all the campaigns until now where T0, mSTS, mMuCh and mTOF were included. Some of the main results from both the periods of 2019 and 2020 have been discussed below. In the Nov/Dec-2019 run, about 90%(17 out of a total of 18 FEBs) of GEM1 was active. The time correlation spectra between a FEB of GEM1 and T0 and also between two FEBs within GEM1 are shown in Figure B.4.2. The Right-side figure demonstrates the variation of offsets for all FEBs after correction. The plot in the inset shows the narrow spread of these values, which is helpful for event reconstruction.

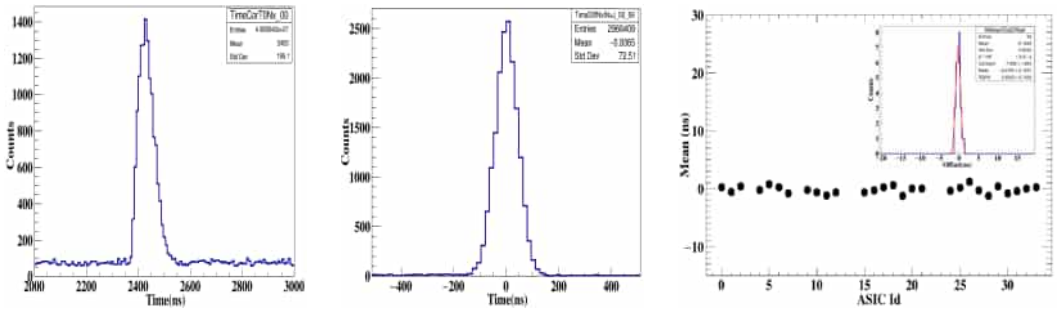

Figure B.4.2: Time difference distribution for Nov/Dec 2019 data. Left: between one FEB of GEM1 with T0 digi without offset correction. Middle: between two FEBs of GEM1 after offset correction. Right : distribution of the corrected “means” for all the FEBs along with their relative spread in the inset.

Figure B.4.3 shows the spill structure as measured by the mMUCH modules along with T0 for the Nov/December 2019 run. The raw data from GEM1, without noisy-channels-removal is

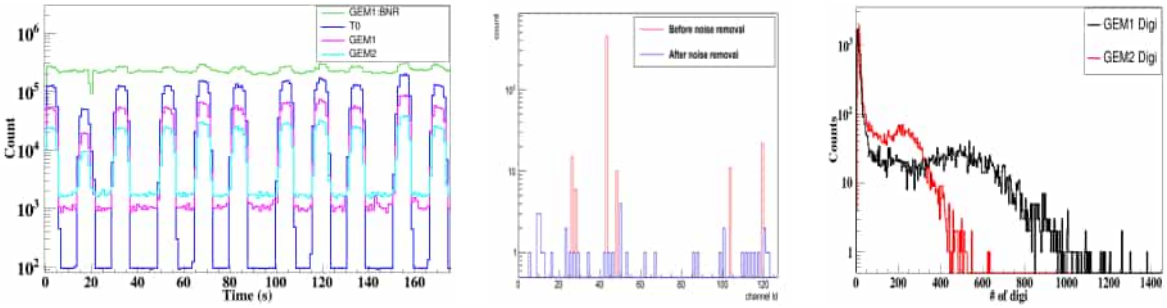

Figure B.4.3: Left: Spill structure for GEM1, GEM2 and T0 for Nov/Dec 2019 run. BNR stands for "Before Noise Removal". Middle: A representative plot for noisy channels removal showing the off-spill counts for a FEB. Right: number of digis per TS for GEM1 and GEM2.

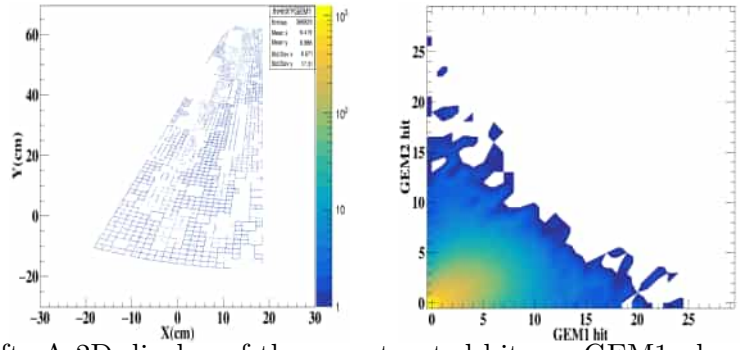

Figure B.4.4: Left: A 2D display of the recontructed hits on GEM1 plane after event reconstruction. Right: Multiplicity correlation of GEM1 and GEM2 after event reconstruction, for Ar+Au collisions(Dec2019).

shown in green. One can hardly see any spill structure and it becomes extremely clear, after removing the noisy channels (by the process shown in Figure B.4.3) (middle) for both the GEM modules. They match perfectly with the T0 spill structure, with a spill duration of 7.5 seconds. Figure B.4.3 (right) shows the distribution of ndigis/TS for the two mMUCH modules. GEM1 peaks on the higher side owing to its higher acceptance. Events were reconstructed for every Time-slice by grouping all the hits involving GEM1, GEM2, T0 and TOF in a time window of 200 ns. Any such group of hits satisfying along with the condition of having a minimum of 10 TOF digis and 1 T0 digi in this time interval of 200 ns was considered to be an event. A 2D distribution of the hits reconstructed in GEM1 plane has been shown in Figure B.4.4, while the multiplicity correlation between hits in GEM1 and GEM2 is shown in right panel of the figure.

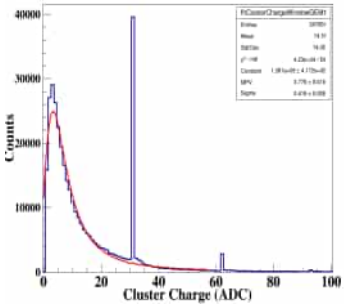

Table 1. Table for pad size at different granularity regions.

Granularity Region	Pad Size (mm)
1	~3.22 - ~4.55
2	~4.55 - ~6.22
3	~6.44 - ~8.49
4	~7.66 - ~10.09
5	~9.59 - ~11.40
6	~11.59 - ~14.02
7	~14.02 - ~16.97

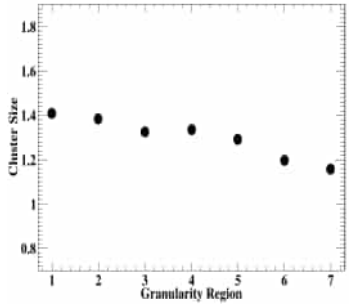

Figure B.4.5: Left: ClusterADC distribution for GEM1 (HV=4600). Middle: table showing labled regions having pads of different dimensions, in the sector shaped module and (right) variation of cluster-size with pad granularity region.

The cluster ADC distribution of the reconstructed hits is shown in Figure B.4.5 left. The readout plane of mMUCH consists of progressively increasing pad sizes and these regions are indicated in the table shown in middle panel of the figure, while the corresponding values of the average cluster-size in these different regions are shown in right panel of the figure.

Several high intensity runs were taken during Mar-May 2020 campaign. Shown in Figure B.4.6 (left) is the spill structure from mMUCH modules for three different interaction rates for a GEM HV of 4600 V. For such a high intensity run (run 534 – 8x10^7 particles/spill), the ndigis correlation per time slice for GEM1 and GEM2 and that with TOF is shown in the middle and right panels of the same figure, respectively. The GEM1 digis is observed to be linearly correlated with those in the TOF detector.

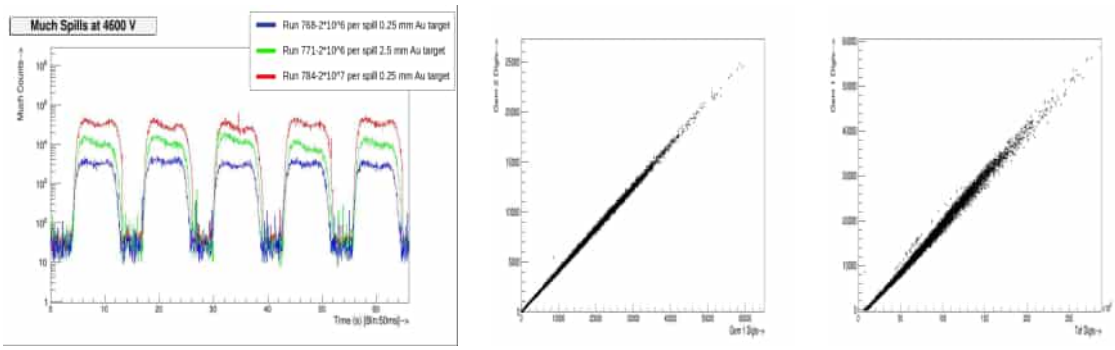

Figure B.4.6: Left: Spill structure at different interaction rates (March-May2020). Number of digis correaltion in TS for GEM1 vs. GEM2 (Middle) and GEM1 vs. TOF(Right) for high intensity (8x10^8 per spill) case

Based on the data campaign in the first phase of the mCBM, we draw following conclusions:

- We could operate both the GEM chambers at low beam intensity (up to 10^6 per spill) with very good noise performance and could obtain spill structures, time correlation with each other, with T0, TOF and TRD.
- A dedicated LV distribution box (LVDB) developed for the main CBM had been used in the mCBM setup. A control system developed for CBM was also used in the setup. However, control system of HV could not be tested.
- A time-based event-reconstruction algorithm was applied for the analysis, good correlations between hit-multiplicities as measured by various detectors were obtained. T0 showed a saturating behaviour at high multiplicity.
- Hits have been reconstructed from the recorded Digis and spatial correlations (X-X and Y-Y) seen between hit positions of different chambers as was obtained from the data taken in December 2019. For the data taken during March-May 2020, we could extract good correlation between Y-positions of two GEMs, X-X correlation needs further work.
- At very high voltage ($>$ 4700V) and at high intensity ($>$ 10^7 per spill), FEBs in the chambers started showing “link break” where communication between affected FEB and AFCK got lost. During the entire data taking period, several efforts have been made to solve the issue, however, still the work is ongoing.
- In the readout, time sychronization between different FEBs/AFCKs and during the entire run was a major issue as observed during data analysis. Quite often, time-stamps of FEBs were to be adjusted for the offsets created for unknown reasons.

- The method of finding efficiency of the chambers using mTOF tracks is being developed.

B.4.3 Upgrade for 2020/21

In view of the performance so far, we propose a setup shown in Fig. B.4.7 with major targets given below for our next set of mCBM beam campaign (2021-24):

- Run the setup with three GEM chambers and fully populated with FEBs. We might install new GEM modules based on the R&D being performed in the lab and results obtained in the last run.

- We also plan to replace one or two present GEM chambers with a chamber suitable for the 2^{nd} station of MuCh.

- Run with a range of beam intensities including maximum possible intensity of high statistics. We need to sort out the "link break" issue before the data taking.

- Include a single-gap low-resistivity bakelite RPC in the setup as shown in Fig. B.4.7 and run with STS-XYTER for required intensity. We might opt to run with the gas mixture of mTOF (5% SF6), however availability of a dedicated gas system will be very useful as we usually operate the chambers with lower SF6 fraction that plays a major role in terms of opearting voltage of the chambers. Due to space constraints, overlap of RPC with other detectors might not be very high, but we plan to test the standalone RPC in various conditions. The RPC module will be of same shape, size and segmentation as of the 3^{rd} station of CBM-MuCh. RPC made of same electrode materials (linseed-coated bakelite) have been tested in the lab and at GIF++ at CERN with muon beams and photon flux. The final RPC pick-up panel will be based on the results of these tests. The RPC will be placed 20 cm away from the GEM2 module side-wide. Simulation study shows a maximum of 10 kHz/cm2 interaction rate at the proposed position for 10 MHz beam intensity in 1.2 AGeV Au+Au collisions. The FEBs will be equipped with STS-XYTER-2.1 and will be tested at low and high beam intensities. Depending on the available space during the run, we might opt to test different RPC modules.

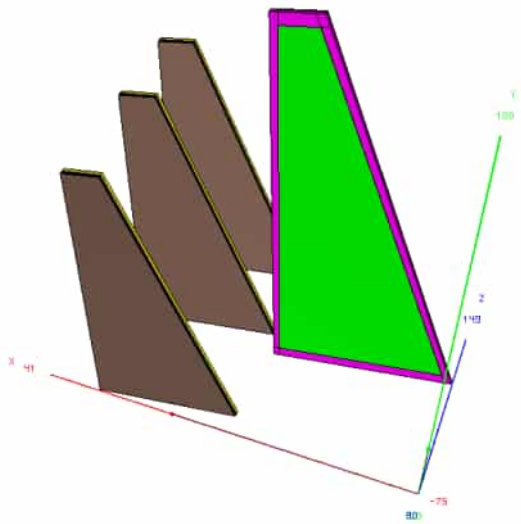

Figure B.4.7: Proposed mMuCh setup including RPC(shown in green)

B.4.4 Readout electronics

In the upcoming beam-time, a new FEBs will be used which focuses mainly on issues mentioned below:

- Compact design: This is a new MUCH specific FEE board with reduced flexible detector connections links. Right now there are separate flexible links used which are not the part of the FEE board. This will be integrated with the new MUCH FEE using rigid-flexible PCB along with metal core bottom layer design. This will improve the noise performance, cooling performance and space management of the MUCH system.
- ESD protection: These are additional ESD protection diode to be installed at the input of the FEE board. These are placed mainly for the RPC detectors so that highly ionizing particle in the detector will not destroy the electronics channel as can be seen from the lab experience.The readout setup could be tested with CRI as it will be used in the final CBM setup. During the run, optimum parameters of the ASIC will be obtained for highest intensity runs.
- We also plan to run with CRI as and when other CBM subsystems adopt that.

B.4.5 HV, LV and controls

- We plan to use a HV system built at VECC for testing the feasibility of running GEM chambers with them. RPC will however use the existing HV system at mCBM
- Present LVDB prototype board is a 30 cm x 15 cm in dimension and has 15 active channels. In the upcoming test beam we will upgrade it to a compact real size LVDB board which will be 15 cm X 10 cm with provision to feed power to 18 FEE boards.
- Python based/EPICS based slow control data acquisition software will replace the existing GUI based Matlab program.
- A monitoring system to monitor cave parameters (pressure, temperature) and gas monitoring system will be installed.
- UDP point to point communication will be upgraded to DHCP TCP protocol.
- HV segmentation control system is being developed for the GEM detectors and have been already tested with a stand-alone setup. In the upcoming beam time, this microcontroller based HV controller will be installed and its performance will be verified.

B.5 mTRD

B.5.1 Detector setup

The final installation of the TRD in mCBM will consist of four layers à one module, see Fig. B.5.1. These TRD modules have outer dimensions of 95 x 95 cm^2 and compare mostly to the large modules foreseen for the outer region of the CBM-TRD at SIS100. They are equipped with pad planes segmented into 6×128 = 768 rectangular pads each, see Fig. B.5.2. In a first integration phase, the integration of two layers will be completed, supposed to deliver already one hit with precise x coordinate (1^{st} layer) and one hit with precise y coordinate (2^{nd} layer) per track. Before the 2020 mCBM beam measurements, it was possible to install the first TRD module as visible in Fig. B.5.3.

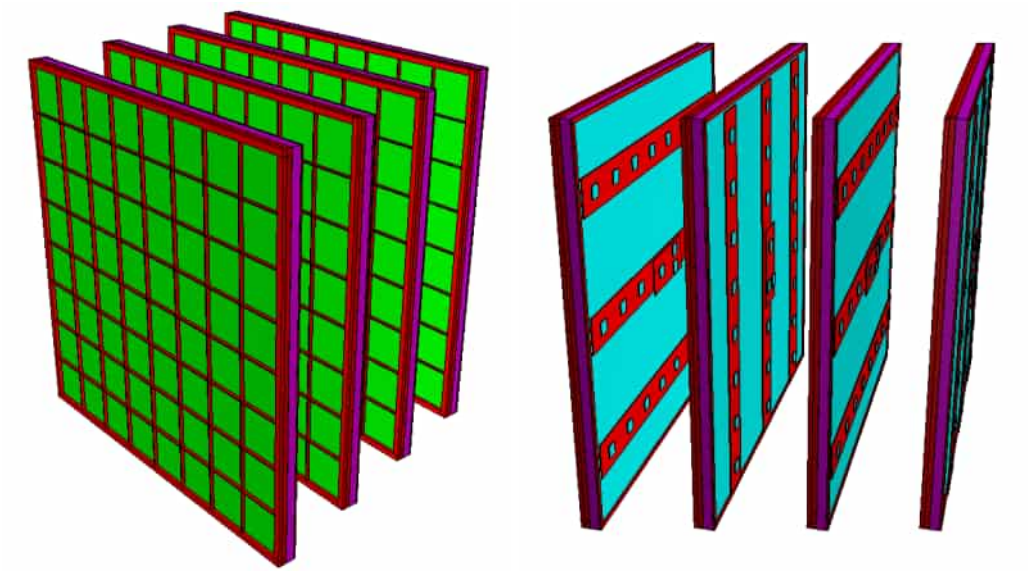

Figure B.5.1: mCBM-TRD geometry v18e as included in CbmRoot.

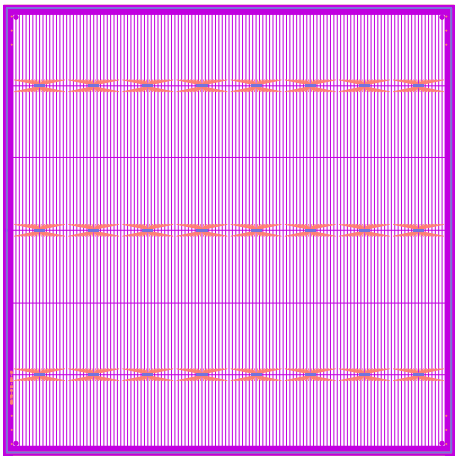

Figure B.5.2: The pad plane layout for TRD module type 2015/8 consists of 6 rows of 128 pads. The pads are about 7.18 mm x 150 mm in size. Each pair of pad rows will be equipped with two SPADIC Quad-FEBs. These Quad-FEBs are populated each with 4 SPADIC ASICs.

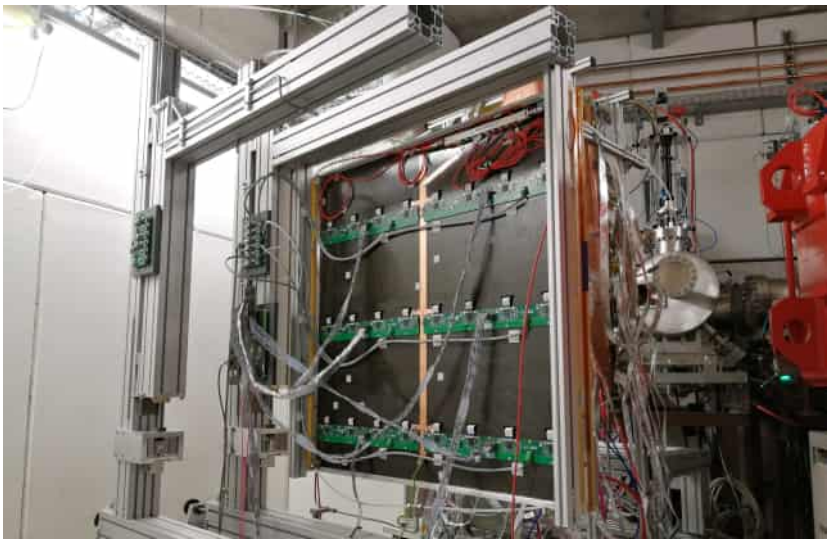

Figure B.5.3: Photograph of the first mCBM-TRD module with SPADIC 2.2 readout electronics after installation for the 2020 mCBM campaign.

B.5.2 Readout

The TRD uses the GBTx ROB-3 for multiplexing the e-link connections of the front-end electronics to the DPB layer. The SPADIC readout electronic is arranged on Quad-FEBs with four ASICs à 32 channel, thus 128 readout channels per FEB. Each Quad-FEB can be connected to the data acquisition system via 8 uplinks, configured via 1 shared downlink and needs to be supplied with 1 clock downlink. As these TRD modules were designed prior to todays definition of the CBM data acquisition, it was chosen to read out here only 7 of 8 pad columns per TRD module, but thereby to enable data transport using only 1 GBTx ROB-3 per module, as specified also in Table B.5.1. Table B.5.2 shows the requirement of DPBs for TRD readout.

object	number of FEBs	number of e-links	number of ROBs	e-links on ROBs	e-links unused
module type 8	6	3x8+3x6 = 42	1	42	0
total	24	168	4	168	0

Table B.5.1: Amount of Quad-FEBs and GBTx ROB-3 required to read out the mCBM-TRD.

object	number of ROBs	optical up-/down-links	duplex fibers	DPBs
module type 8	1	3+1	3	1
total	4	12+4	12	4

Table B.5.2: Required amount of DPBs to interface the GBT links from the mCBM-TRD.

B.5.3 DPB firmware

The TRD DPB firmware was updated to support the CROB based readout of the SPADIC 2.2. The CROB features 3 GBTx ASICs with 14 uplinks each, therefore the data preprocessing was

set up to support 42 uplinks. In addition to the FPGA firmware, also the control software was updated to support the new GBTx firmware.

In preparation for the common readout in the mCBM setup, the DPB firmware for the TRD has been implemented with the necessary data-preprocessing to generate microslices in accordance to the FLES specifications. For this, a message decoder was implemented which generates a SPADIC message container from the SPADIC message frames. The message container comprises all the metadata of the hit message, i. e. the e-link ID, channel ID, timestamp, hit type, multihit flag and the number of samples, as well as up to 32 ADC samples.

After that the message containers are sorted into their respective microslices. This is done through a time gating module which controls the data flow of the hit message containers. The hit messages of each e-link are continuously passed through until the first message arrives which belongs to another microslice. Then the data flow is stopped for that particular e-link until all e-links received the first message of the next microslice.

The sorted hit messages are then serialized into an efficient 64 bit format, packed into microslices and sent to the FLIB. The data preprocessing as well as the microslice generation has been successfully tested during the 2019 DESY TRD testbeam campaign and confirmed in the 2020 mCBM campaign. During the 2020 mCBM campaign, the firmware was hardened for operation in high-load situations of the common system, characterised e.g. by back pressure from FLES side, which was successfully tested.

B.5.4 TRD-specific software

The raw data messages of the TRD readout are highly optimized containers for the transfer of the raw information generated due to a registered signal on a channel (“hit message”). However, for further processing of the information the messages need to be unpacked and written into an analysis oriented container. For this purpose, a completely new *TRD unpacking* software was written. The new version not only suits the general format and data flow of mCBM, but also provides online-monitoring capabilities of the incoming data stream.

From regular hit messages, the unpacker extracts information about the hit time, the trigger type, all forwarded ADC samples and whether this hit message follows directly to a previous signal (“multi-hit”). The package provides several modes of operation, varying from a focus on performance to one on debugging.

The software also translates the position information from the hit message into a global CBM address. The reconstruction is based on: the channel ID in the local ASIC coordinate system and the ID of the ASIC in the global TRD coordinate system. While the local channel ID can directly be read from the TRD raw message, the ASIC ID has to be reconstructed via the eLinkID and the ID of the AFCK. The mapping between the given information in the TRD raw messages and the global channel addresses in the CBM address scheme is read from parameter files into the unpacker, which have to be prepared beforehand.

A first test of the software package took place at the DESY 2019 testbeam campaign. It was successfully used in the 2020 mCBM campaign, during which also the set of run macros for comfortable usage of the package was optimised.

B.5.5 First results

Since TRD joined the common mCBM readout beginning with the commissioning phase 2020, it is of highest interest to investigate the commissioning records and SIS18 beam records, e.g. in terms of detector behaviour and proper function of the readout. Fig. B.5.4 shows the repoduced accelerator spill structure in agreement with another subsystem, which we interpret as proof of the data transport and time building/reconstruction on the large scale. Fig. B.5.5 shows the correlation of digis in time to another subsystem on nano-second scale. The correlation peak

of the TRD was found to be stable over time. An improved time resolution is currently being prepared by implementation of precise pulse time reconstruction from the recorded signals.

Fig. B.5.6 shows the distribution of trigger frequencies in the online monitoring system during common run 745. The TRD geometry with six pad rows leads to six bands, visible in the plot as expected.

Further quality checks are ongoing, e.g. analyses of trigger efficiency and signal quality are in preparation, but also spatially resolved correlation and track reconstruction is to follow. These checks are expected to deliver valuable information for the configuration of TRD with two layers for the next measurements.

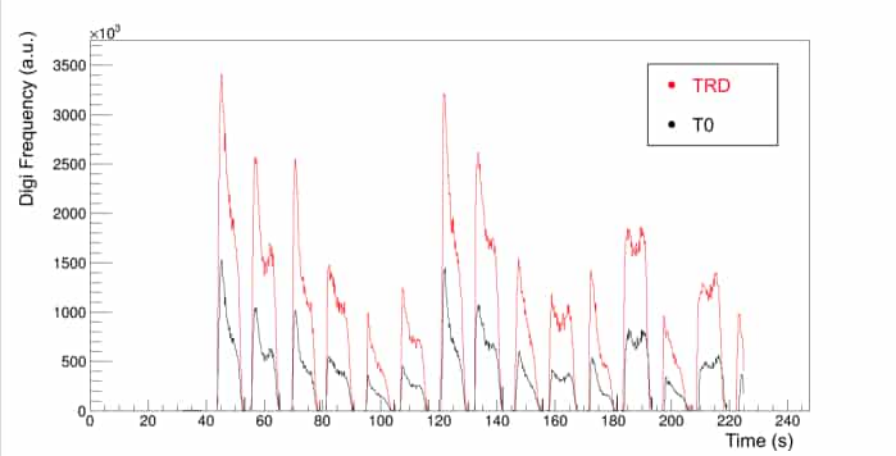

Figure B.5.4: Digi trigger frequency of two subsystems in mCBM in run 458.

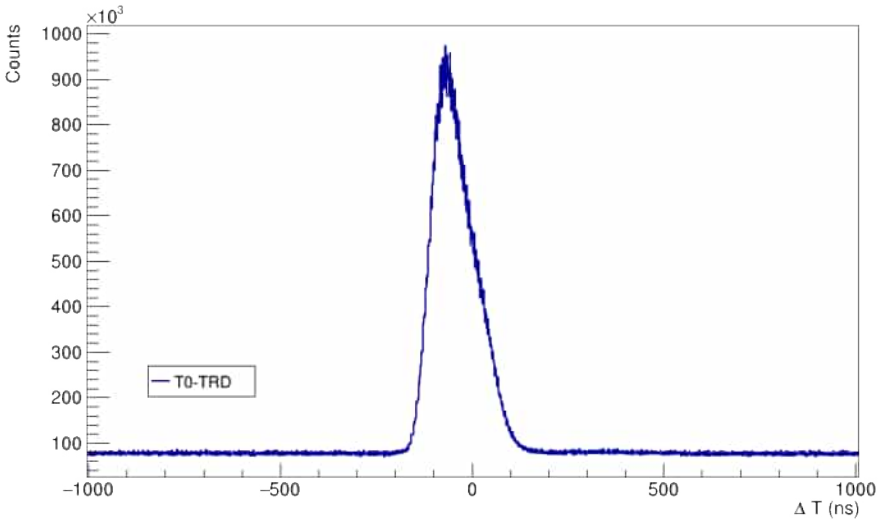

Figure B.5.5: Time difference of digis from TRD and another subsystem in run 760, interpreted as correlation.

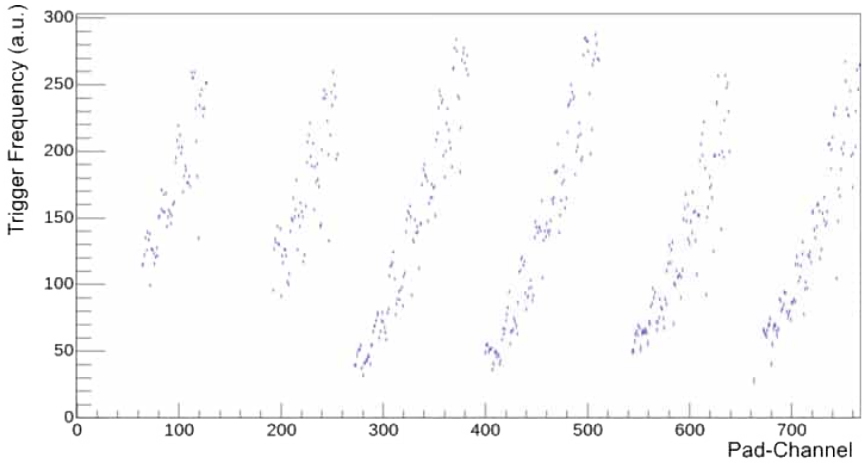

Figure B.5.6: Trigger frequency vs. readout channel, TRD online monitoring, during run 745.

Figure B.5.7: Four TRD modules as foreseen for installation in mCBM, photograph taken during preparation phase of an earlier testbeam campaign.

Detector and Periphery Control System

The mCBM-TRD was supplied and monitored in terms of LV, HV and detector gas in the 2020 campaign successfully using the available detector control system. The parameters of the foreseen final control system are listed in Table B.5.3.

Subsystem	Location	Controlled unit	Number	Interface	Parameters	Control	Frequency
Readout	ROC	FEB on/off	24	GPIO	Boolean	write	on request
	ROC	FEB temperature	24	I^2C	Temperature	read	1 s
	ROC	ASIC on/off	96	GPIO	Boolean	write	on request
	ROC	ASIC power	96	I^2C	Voltage	read	1 s
	ROC	ASIC configuration	96	File (DAQ)	SPADIC config values	read	per run
ROC	Cave	ROC environment	1	RS485	Temperature, humidity	read	1 s
FEB LV	Cave	LV channel on/off	4	CAN-bus	Boolean	read/write	1 s
	Cave	LV channel control	4	CAN-bus	Voltage, current lim	read/write	0.5 s
	Cave	LV PS temperature	1	CAN-bus	Temperature	read	1 s
Drift HV	Service area	HV channel on/off	4	EPICS	Boolean	read/write	1 s
	Service area	HV channel control	4	EPICS	Voltage, ramp speed, current lim	read/write	0.5 s
Anode HV	Service area	HV channel on/off	4	EPICS	Boolean	read/write	1 s
	Service area	HV channel control	4	EPICS	Voltage, ramp speed, current lim	read/write	0.5 s
Gas system	Gas level	H_2O sensor	1	RS485	Humidity	read	0.5 s
	Gas level	O_2 sensor	1	4–20 mA	Oxygen contamination, temperarure	read	0.5 s
	Gas level	Gas component flow	2	RS485	Flow set/flow measurement	read/write	0.5 s
	Gas level	Gas supply line flow	3	4–20 mA	Flow	read	0.5 s
	Cave	Detector level pressure	2	4–20 mA	Pressure	read	0.5 s

Table B.5.3: Main parameters of the foreseen detector control system for the mCBM-TRD. The system used in 2020 was partially using different interfaces.

B.5.6 mTRD-2D

For the inner region of CBM, the collaboration considers a significantly improved alternative to that presented in the TDR of the TRD. Employing triangular readout pads, this alternative would ensure significantly improved 2D position information with a single detector layer. Subsequently, also the FEE is specially designed for such read-out topology wrt the TDR TRD modules. In Fig. B.5.8 the status of the mTRD-2D integration in the mCBM is presented, in terms of mechanical, software and hardware developments. The mechanical structure used to mount the module on the mCBM experimental table is shown in Fig. B.5.8-left; integration in the CbmRoot geometry in Fig. B.5.8-top-right. Reading-out and reconstruction of the signals together with the rest of the subsystems is also in a close to final stage. The FEB boards which house the read-out ASIC *Fast Analog Signal Processor* (FASP) and the digital processor component *Generic Event Time-stamping Streamer* (GETS) are shown in Fig. B.5.8-bottom-right. The mTRD-2D FEE is integrated in the AFCK-FLIB read-out. The extension the to CRI board is also considered.

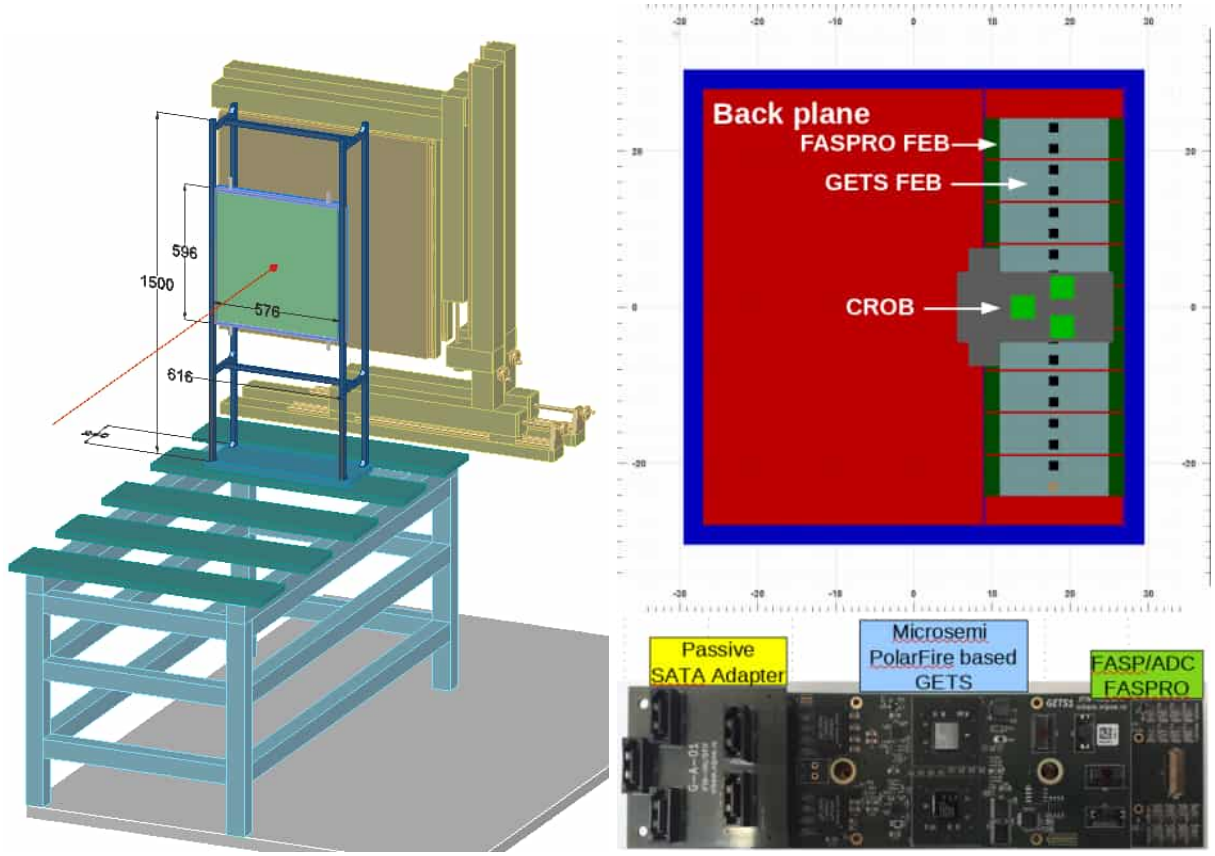

Figure B.5.8: Proposed installation of the mTRD-2D module in the mCBM setup (left) and some key elements of CBM integration; the CbmRoot geometry implementation (top-right) and the FASPRO-GETS FEBs system (bottom-right).

The detection requirements for the TRD inner zone were demonstrated by the TRD-2D prototype during the R&D period. An outstanding spatial resolution capability was shown, by a first tracking setup, already during a CERN-SPS test beam in 2015 (see Fig. B.5.9-left). The measured results were afterwards substantiated by a detailed and realistic implementation in CbmRoot. In Fig. B.5.9-middle the intrinsic $x - y$ position resolution is shown wrt to MC position information. Last but not least the particle rate capabilities are a key feature of the inner zone detection technology. We have demonstrated such capabilities by monitoring the reconstructed cluster rate over a continuous X-rays irradiation interval of 5 *min*. The rate

was controlled by keeping the X-ray tube intensity constant and modifying the distance to the detector. In Fig. B.5.9-right the results obtained for various distances (see the r_0 parameter) are shown. A maximum X-photon rate of 50 kHz/cm^2 was detected and transported to disk by the TRD-HR FEE without loss. The design target rate is 100 kHz/cm^2 which should be achievable in the context of the mCBM setup.

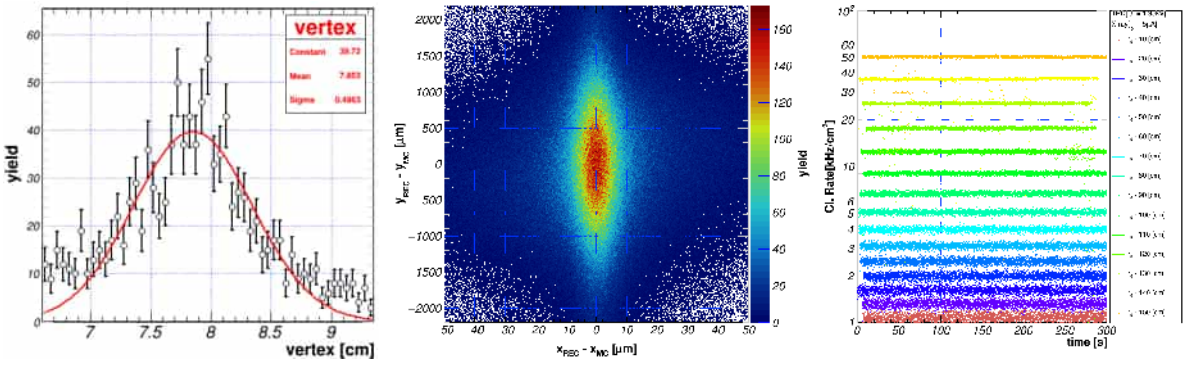

Figure B.5.9: Performance plots obtained with the mTRD-2D module; position resolution of vertex obtained with three TRD stations at CERN-SPS (left), 2D position resolution of hits wrt MC particles in CbmRoot (middle) and measured X-rays rate in a free-running DAQ (right).

The TRD module (mTRD-2D) will be installed in the mCBM experiment, together with the mTRD modules mentioned in appendix B.5, during phase III of commissioning. The read-out will employ up to 9 FASPRO boards operating up to 54 FASP-04 ASIC (see Fig. B.5.8, top-right).

mTRD-2D readout

Similar to the mTRD prototypes, the mTRD-2D uses the GBTx ROB-3 board for interfacing the FEE to the DAQ. Each FASP chip is read-out using 1 e-link @ 320 MBits/s out of the 14 e-links/GBTx chip available. A total of 6 ROB-3 are needed to read the full module with an e-link efficiency of 71%. As we foresee our participation starting in phase II, the connection to the FLES input node will be based on the CRI-12 boards with 2 CRI boards reading our 18 GBTx up-link connections.

object	number of FEBs	e-links on FEBs	number of ROBs	e-links on ROBs	e-links unused
module type 4	18	18 x 10 = 180	6	42 x 6 = 252	72

Table B.5.4: Amount of FEBs and GBTx ROB-3 required to read out the mTRD-2D.

object	number of ROBs	optical up-/down-links	duplex fibers	CRIs
module type 4	6	6x (3+1) = 18+6	18	2

Table B.5.5: Required amount of CRI-12 boards to interface the GBT links from the mTRD-2D.

B.6 mTOF

Since the operation start of mCBM the mTOF setup consisted of five full size modules from type M4 (see Fig. B.6.1 right corner). Each module comprises 5x MRPCs from type MRPC2 (former MRPC3a [8]), 10x PADI FEE preamplifier/discriminator boards (32 channels each), 10x Get4 FEE TDCs (32 channels each), and 2x Readout Boards equipped with a single GBTx chip. MRPC2 counter has a double stack structure with 2×4 gaps of 25 μm gap size and low resistivity glass of 0.8 mm thickness. the read out electrode has 32 strips with 1 cm pitch and 27 cm length and is readout on both sides. The MRPC2 counter is foreseen for the intermediate rate region [8] of the CBM TOF-wall with the requirement of a rate capability about 5 kHz/cm^2. The total active area of the mTOF is 150 x 125 cm^2 and comprises 1600 read out channels.

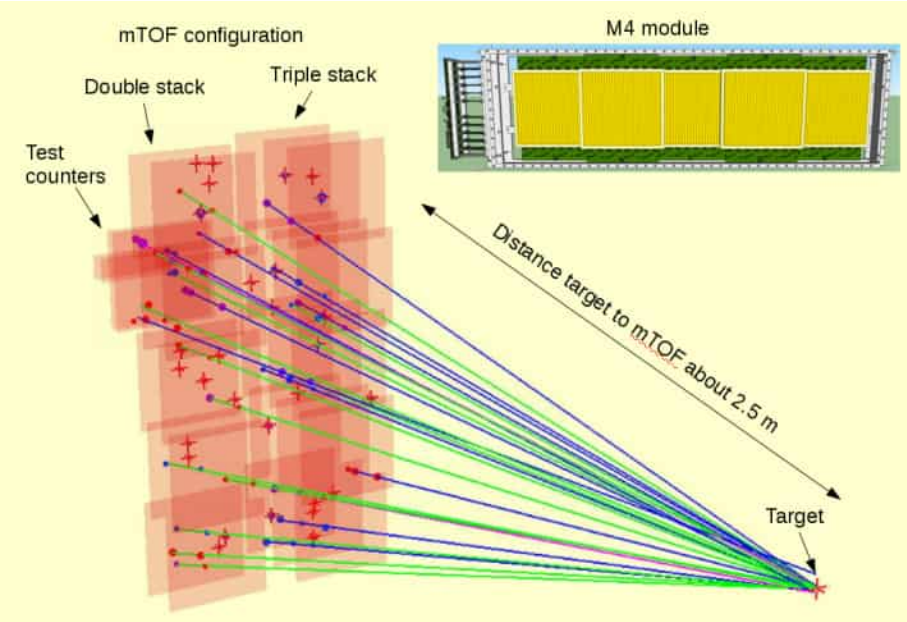

Figure B.6.1: Technical drawing of a mTOF M4 module, holding 5 MRPC2 counters combined with an event display of a measured high multiplicity Pb+Au event.

As depicted in Fig. B.6.1 the 5 mTOF modules were arranged in a triple and a double stack configuration. The triple stack, centered at 25° in respect to the beam, allows to form triple hit tracklets which can be use by the other subsystem as a reference. However, with three staggered modules the performance of each module can be elaborated by using the other two as a reference. The double stack, located closer to the beam (at a polar angle of about 12°), faces a higher particle flux and offers a reference system to additional CBM TOF MRPC prototypes which were tested during the beam time campaigns. It is evident that also from the doubles stack two hit tracklets can be obtained. Figure B.6.1 shows an event display of a high multiplicity event generating 100 hits in mTOF of which 28 tracks could be reconstructed.

The infrastructure for the mTOF system consists of a clock distribution, a LV power supply (MEAN WELL) with 12 V and 100 A, a LV distribution box with 16 channels, a 15 kV HV power supply (CAEN + ISEG) with 12 + 4 negative and 12 +4 positive channels and a closed loop gas system.

B.6.1 Beam time results from mTOF

As already mentioned in chapter 2.3 the test of detectors and readout with heavy ion beams under similar rate conditions as in full CBM is essential in order to reach all anticipated milestones.

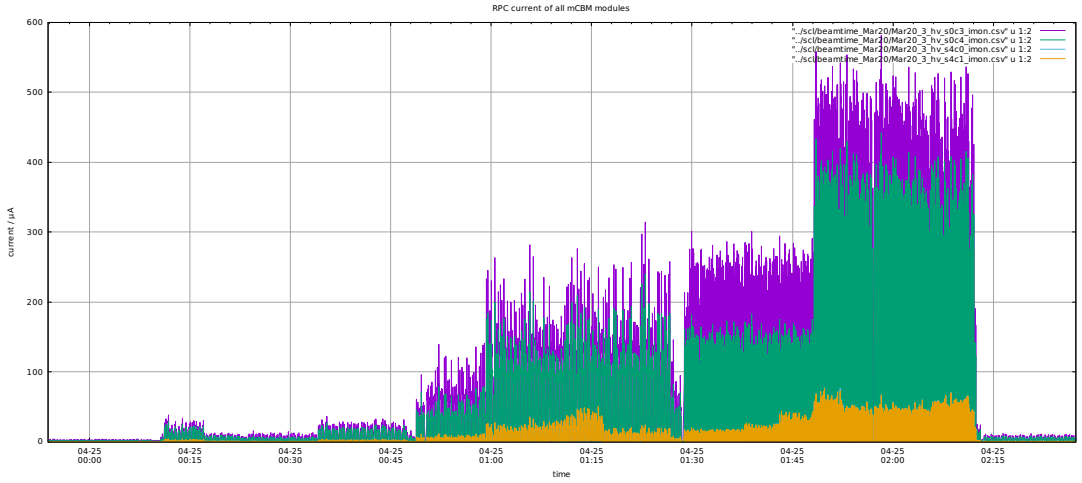

Figure B.6.2: Measured HV current from the double stack + test counters during a rate scan performed on 25th of April 2020. From the current it is possible to make conclusions on the incident particle flux.

One important milestone for TOF is the ASIC engineering design review (EDR). For this purpose the counters of the triple stack were equipped with the new PADI version XI allowing a comparison to those of the double stack which were readout by PADI version X. Detailed analysis is ongoing.

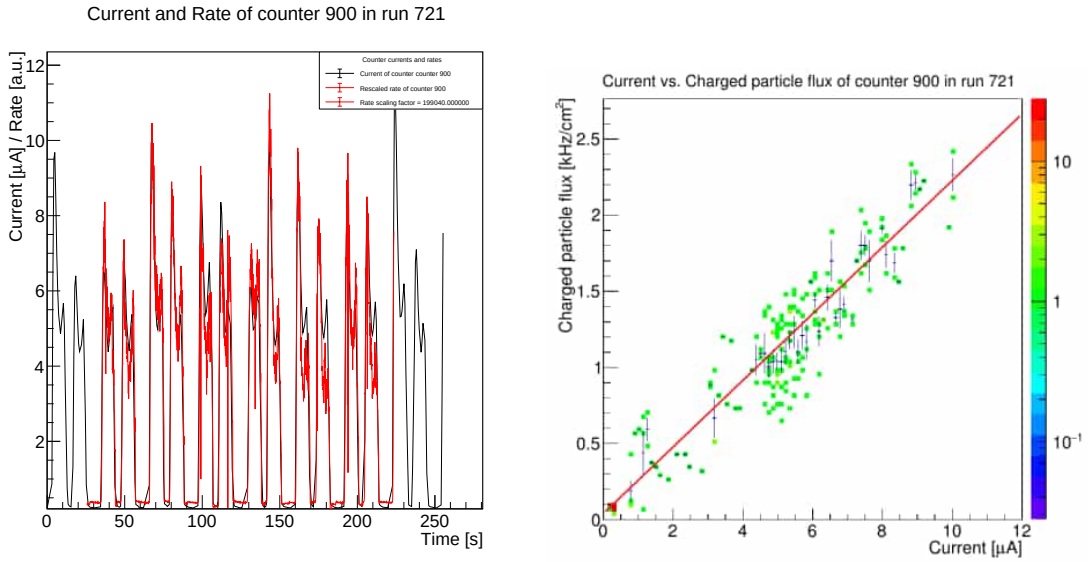

Figure B.6.3: Left: Measured HV current (black) and rescaled rate (red) of counter 900 as function of time. The rescaling factor is shown in the legend. Right: Correlation between incoming charged particle flux and drawn current of counter 900 (MRPC3). In run 721 particle fluxes up to 2 kHz/cm^2 were reached.

Another important milestone is the HV conceptual design review. Since the CBM TOF wall will be exposed to particle fluxes from 100 Hz/cm^2 at large polar angles to about 30 kHz/cm^2 in the center the HV current consumption (which is rate dependent) has to be precisely known in each module in order to optimize the HV supply system. During the last beamtimes the mTOF HV currents were recorded. As an example Fig. B.6.2 shows an overlay of the measured currents

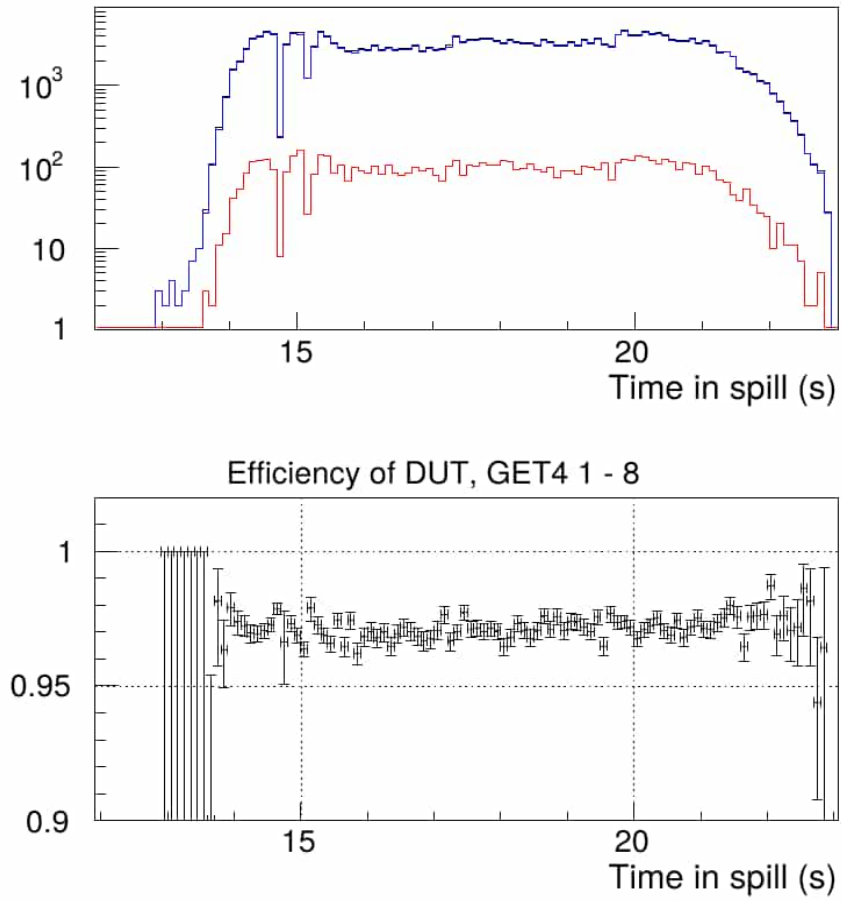

Figure B.6.4: Top: found (blue) and missed (red) hits on counter 900 as function of time in spill. During run 717 the incoming particle flux was in the order of 600 Hz/cm^2. Bottom: Efficiency as function of time in spill.

of the double stack modules (green and violet) together with test counters currents (dark yellow) during a rate scan performed on 25th of April 2020.

Currents in the order of 500 μA indicate an average incident particle flux of about 7 - 8 kHz/cm^2. This is higher than the M4 modules will be exposed to at CBM and is enough to demonstrate the functionality of the MRPC2 counters which is required for the acceptance of the production readiness review (PRR).

Towards this goal the analysis has been started for 2 MRPC3 prototypes (labeled as counter 900 and 901) which were operated during the last beam time campaign. The MRPC3 contains ultra thin float glass as resistive material and has a required rate capability of 1 kHz/cm^2. In order to correlate the drawn current with incident particle flux the data obtained by the DAQ have to be synchronized with the data recorded by the slow control system. This is shown on the right side of Fig. B.6.3. The black line denotes the measured HV current where the spill structure is clearly visible. Overlaid is the scaled counter rate (red). With the χ^2 - method these two quantities are synchronized and the offset in time is applied to the rate. Now the two values can be directly compared and plotted in a 2D histogram as shown on the right side of Fig. B.6.3. The y-axis is converted from rate to the incoming particle flux by applying the scaling factor and dividing by the counter area.

The linear dependence between incoming particle flux and drawn current is an indication that the counter fulfill the required rate capability. However, this has to be confirmed by further data analysis. Note, that the counter 900 (containing float glass electrodes) was exposed to a

flux of about 2 kHz/cm^2 in this particular run (721) which is twice as much as the anticipated flux at CBM (important for the PRR milestone).

A first step towards deterning the rate dependence of the counter efficiency was performed by analyzing run 717. Counter 900 was sandwiched between two M4 modules acting as reference. Fig. B.6.4 shows on the left side a histogram where in blue the found hits and in red the missed hits of counter 900 are plotted as function of time in spill. From this plot the efficiency (shown on the right side) can be calculated amounting to 96 % without degradation in time. From this result one can conclude that the MRPC3 prototype is capable to stand a rate at least up to 600 Hz/cm^2.

B.6.2 mTOF upgrade

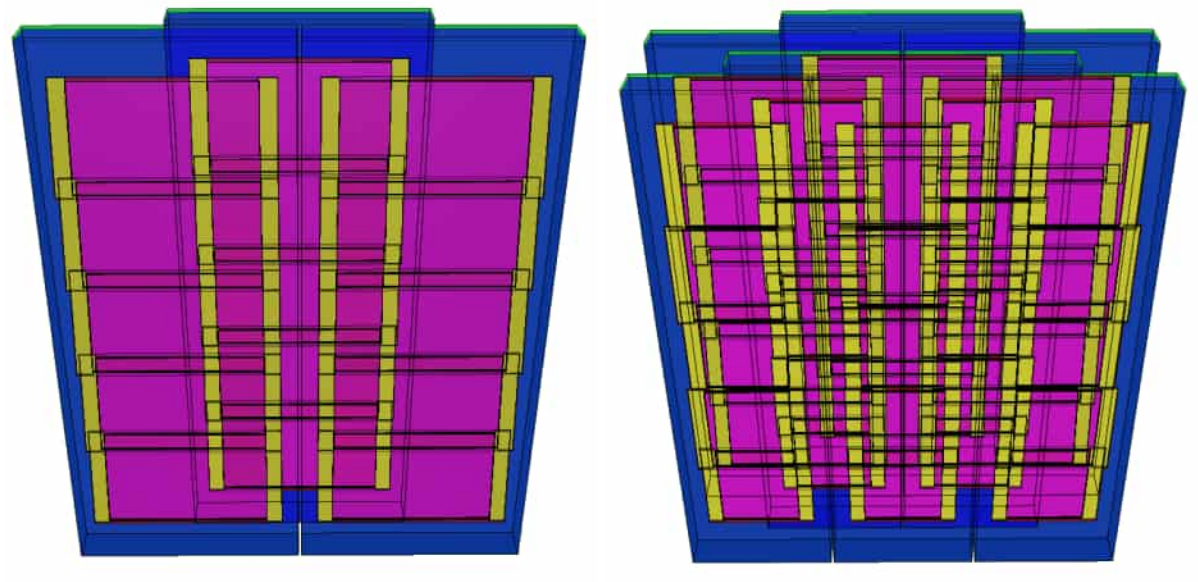

Figure B.6.5: (left) In 2021 the mTOF subsystem will be complemented by an additional layer of three M6 modules. (right) The resulting CbmRoot geometry of the mTOF v20d subsystem consisting of 2 layers: 5x M4 modules in the front and 3x M6 modules in the back.

Since 2018 mTOF was composed of 5 modules from type M4. In order to use the mTOF modules as a reference they where arranged in a triple stack and a double stack configuration as described above. However, this module arrangement does not allow for full mTOF acceptance. In order to have the full acceptance but still keep the benefit of track reconstruction an mTOF upgrade was proposed.

The upgrade plan foresees for 2021 three additional modules from Type M6 (the largest TOF modules in CBM) building up a second layer. Each M6 module contains 5 counters of the type MRPC4 [8] which are tilted inside the gas box by 10° (conf. Fig B.6.5). The counters have an overlap region covering 2 readout strips of the neighboring MRPC.

The MRPC4 prototype contains ultra thin float glass of 0.28 mm thickness as electrode material and is foreseen for the low rate region (up to 1 kHz/cm^2) at CBM. Hence the counter have the lowest granularity (50 cm^2) of all CBM TOF prototypes. The counters have an active area of 50 $\times$ 32 cm^2 comprising 32 readout strips.

In addition it is planned to install new test counters addressing the high intensity region faced by the inner part of the TOF wall. The prototype counters for this investigation are shown on the left side of Fig. B.6.6 and are build with low resitivity glass elctrodes as in MRPC2, however, with a reduced dimension of 30 $\times$ 6 cm^2 and a gap size of 200 μm. The counter comprises 32

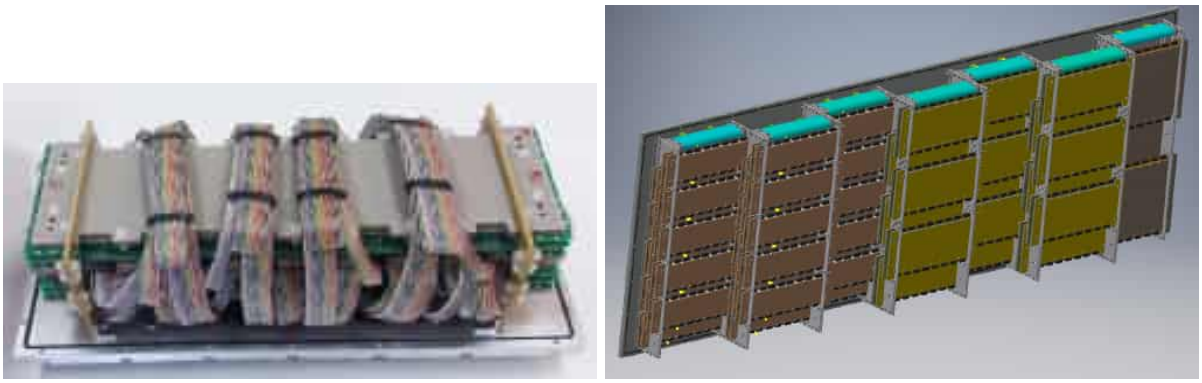

Figure B.6.6: (left) High rate protopype counter MRPC1a. (right) Technical drawing of Module M0 to be constructed in Bucharest.

readout strips with a granularity of 5.6 cm^2. It is designed to cope with a particle flux of up to 25 kHz/cm^2.

mTOF readout

In contrast to the mSTS, mMUCH and mTRD subsystems, which use 3 GBTx ASICs on a single ROB-3 board, the mTOF will integrate one single GBTx ASICs on each readout backplane of which two are connected to each module. This single GBTx is behaving like a ROB-1. The total number of GBT up- and downlinks is therefore symmetrically distributed for mTOF. Its readout system will consist of 16 ROB-1, interfaced with 16 duplex fibers to 1 CRI, as listed in Tab. B.6.1.

object	number of GBTx	optical up-/down-links	duplex fibers	CRI
(5x) M4 module	5 × 2	10 × (1+1) = 10 + 10	10	1
(3x) M6 module	3 × 2	6 × (1+1) = 6 + 6	6	same
total	16	16 + 16	16	1

Table B.6.1: Required amount of CRI devices to interface the GBT links from the mTOF.

B.7 mRICH

The prototype of the Ring Imaging CHerenkov detector (RICH) that is used in the mCBM experiment is based on an aerogel radiator in a dry nitrogen environment and the CBM RICH readout electronics (Fig. B.7.1). It is placed behind the mTOF detector and moved to the center of the mTOF triple stack to have the highest possibility to detect particles passing all detectors and deliver a second measurement of the velocity of the particles.
In combination with mTOF it should be possible to separate protons/kaons from pions/electrons and thus improve the PID and thus momentum measurement in mCBM.

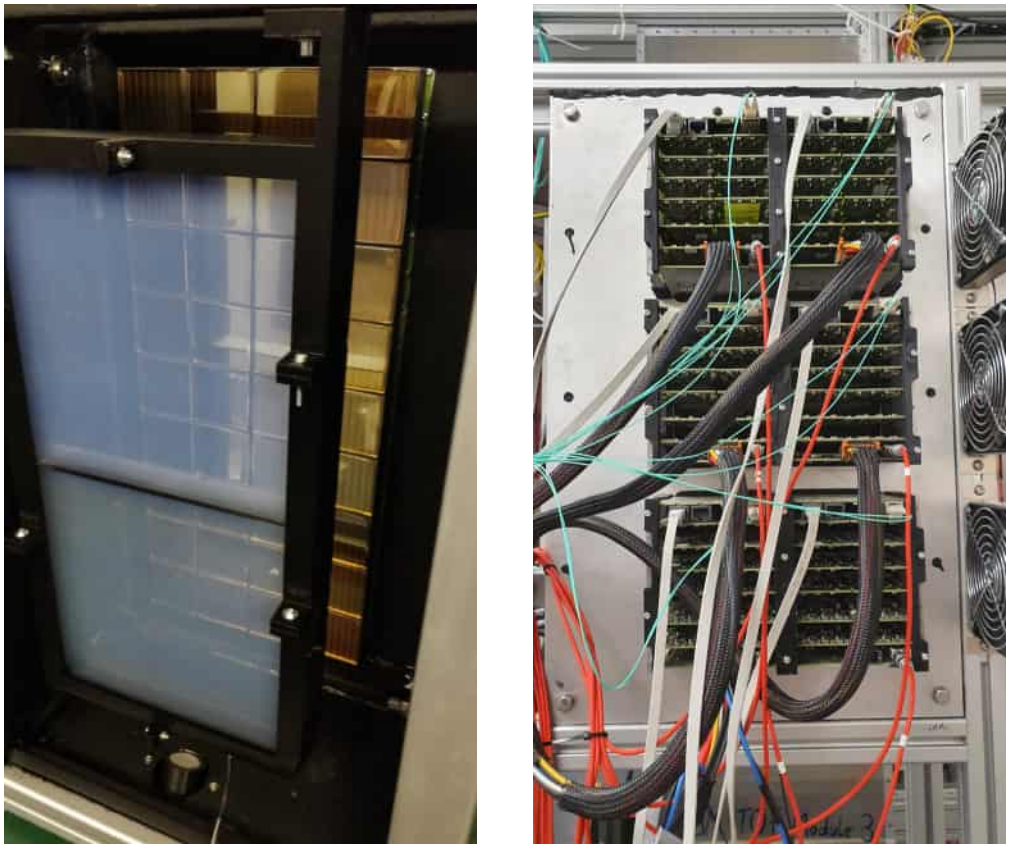

Figure B.7.1: (left panel) Photograph of the (opened) mRICH detector with a view on the two aerogel radiators and the 36 MAPMTs behind. (right panel) Backside of the detector. The readout of the detector with high voltage, low voltage, data fibers and internal "pseudo trigger" distribution.

Two 20x20x3 cm^3 aerogel blocks are positioned inside a metal box with 10 cm distance to the photomultiplier plane. The entrance window of the box is built from plastic and the backside of the detector is equipped with 2x3 CBM RICH readout backplanes. Each backplane hosts 6 MAPMTs. Thus the mRICH detector consists out of 36 Hamamatsu H12700 Multianode Photomultipliers (MAPMTs) and has an acceptance of 47.6 cm x 21.3 cm. One MAPMT has 64 pixels and is read out by two DiRICH Modules each.
In addition to the 12 FEE modules, each backplane has a power module that is used to distribute the low voltages to all FPGAs on the backplane as well as the distribution of the readout signal of the FEE and the high voltage of the MAPMTs.
A combiner module in each backplane is used as data concentrator from all FEE modules. The combiner controls the readout of a backplane and hosts the data connections to higher levels in the readout chain.

Below the mRICH detector (Fig. B.7.2), the readout and power distribution is placed. A HMP4040 LV power supply placed in a radiation save corner of the cave is connected to a copper bar construction via long cables. The 24 V on this line is distributed to 6 DCDC-converter boards that convert the 24 V to the four specific voltages that the FEE needs (1.1 V, 1.2 V, 2.5 V and 3.3 V).
The mRICH uses for now standard TRB Hardware with specific firmware to operate in the CBM environment. A TRB3sc is placed below the mRICH to serve as a hub for the 6 combiner boards. It combines all data streams and sends out the data via optical fibers in UDP packages to the DPB in the DAQ-container. In addition it gets a "trigger" signal from the DPB each time a microtimeslice is started. Based on this information the data from the last microtimeslice is send out in the FEEs. Therefore the TRB3sc hosts a central trigger system (CTS) to control the readout. The TDC finetime of each channel of the DiRICH boards is calibrated online on the combiner board. This simplifies and speeds up the unpacking and the online reconstruction.

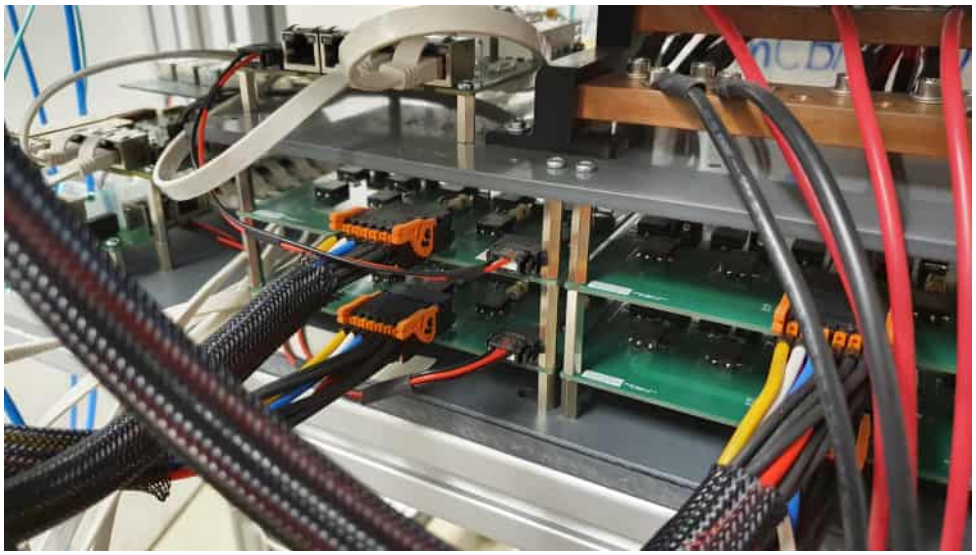

Figure B.7.2: LV distribution and TRB3sc for readout control.

For the future it is planed and under preparation to upgrade the readout scheme to the Common Readout Interface (CRI). Therefore the mRICH readout will be restructured. The previously used TRB3sc with a CTS and the hub functionality will become obsolete as the CTS functionality will move to the combiner board and the hub functionality will be placed in the CRI. This gives the flexibility that each DiRICH backplane is a standalone unit that is operating individually, but synchronous to the CRI. Next to the increase in possible data rates it is to mention that the restart of individual parts of the detector will be more reliable. In addition this change will replace the UDP connection that is nowadays used between the TRB3sc and the DPB to a trbnet connection between individual DiRICH backplanes and a CRI, that can scope with higher package sizes, included slow control messages and more features.

B.7.1 Analysis

The mRICH detector has taken data with the other mCBM detectors in common runs for several times and shows the smallest amount of data due to the small number of channels, see Fig. B.7.3. To achieve a very good time alignment, the detectors are all aligned in time against the T0 detector. The times of digis from all detectors show all an enhancement in the data rate during

spills. Even the relative increase in the amount of data scales properly over the systems.
The application of event building and the ToT-Cut reduces the number of digis in the mRICH. On the resulting hits the ring finder is searching the rings which leads to a very clean separation between spill and offspill as in offspill data no rings are found (Fig. B.7.3).

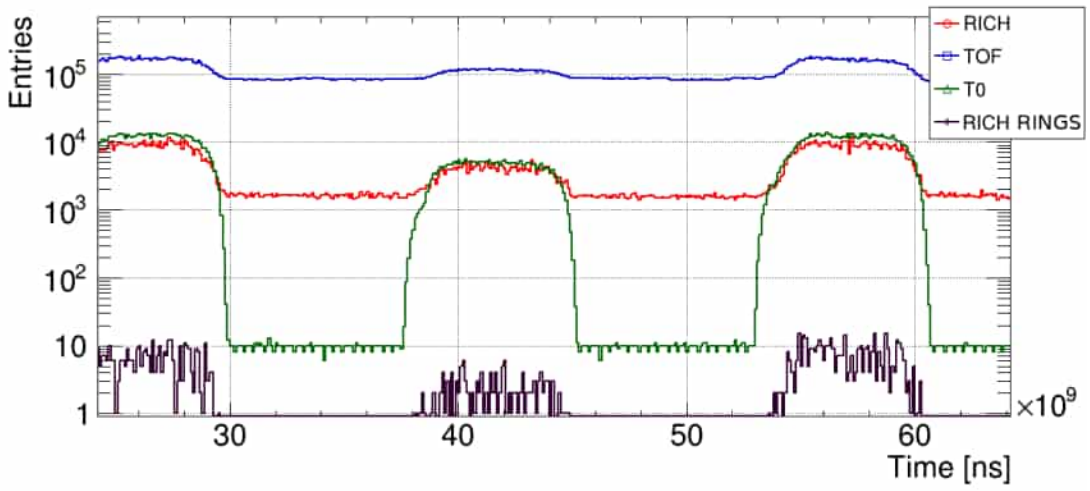

Figure B.7.3: Times of the digis from data stream of RICH, TOF and T0. In addition the corresponding found rings are shown.

The DiRICH boards are using FPGA based Time to Digital Converters (TDCs). Thus for each pixel position, the time of the rising edge of a signal beyond a certain threshold and the corresponding falling edge is known. Based on this information a Time over Threshold (ToT) is calculated and calibrated. Cuts on the ToT help to reduce the crosstalk between two pixels dramatically. Fig. B.7.4 shows the ToT distributions of the mRICH in March 2020 data before the application of a cut in the raw digis. The right side shows the same distribution after the ToT cut and the event building. The expected two sharp peaks are very well separated and a cut could be applied here. The left peak stems from crosstalk and can be cut away. More detailed analysis on background data shows very well the influence of the cut on crosstalk. In Events with more than 10 Hits on the mRICH detector, many of the hits are from crosstalk and could be rejected by applying this cut.

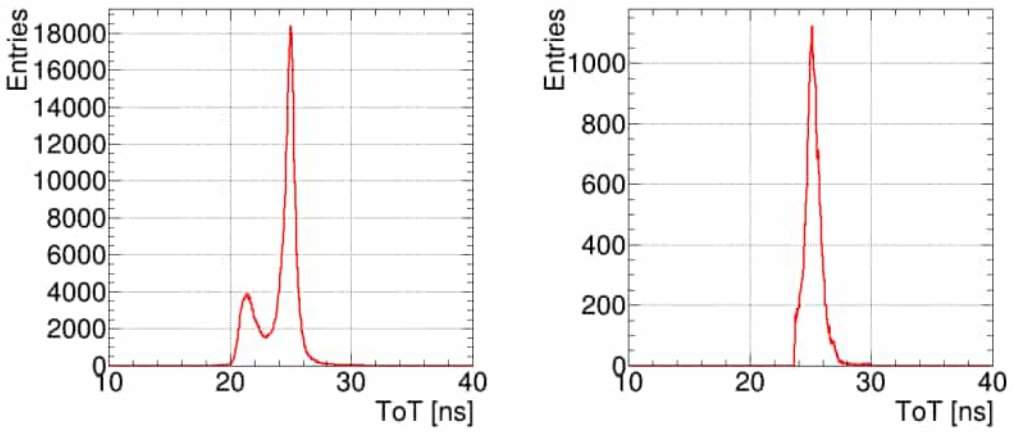

Figure B.7.4: Left: ToT of the raw digis from the detector. Right: ToT after event building and ToT-cut application.

The application of a ToT-cut and the corresponding reduction of the background is nicely visible in the hit distribution Plot. The individual pixels have heavily varying number of hits without a ToT-cut, whereas the application of the cut leads to a more homogeneous distribution (see Fig. B.7.5; lower row).

The mRICH detector has grown in size over the last three data taking campaigns and now is fully equipped. Due to some optimizations and to increase stability, for now the detector was not operated completely, but the hardware is available for a complete data taking. In March 2019 the detector was only using five DiRICH boards and one aerogel block with 12 MAPMTs.

With the availability of a second aerogel and more DiRICH readout hardware, the November 2019 campaign could be done with significantly more acceptance and already a fully equipped MAPMT plane. From November 2019 to March 2020 the last missing DiRICHes could be mounted and the stability of the readout was significantly improved (see Fig. B.7.5).

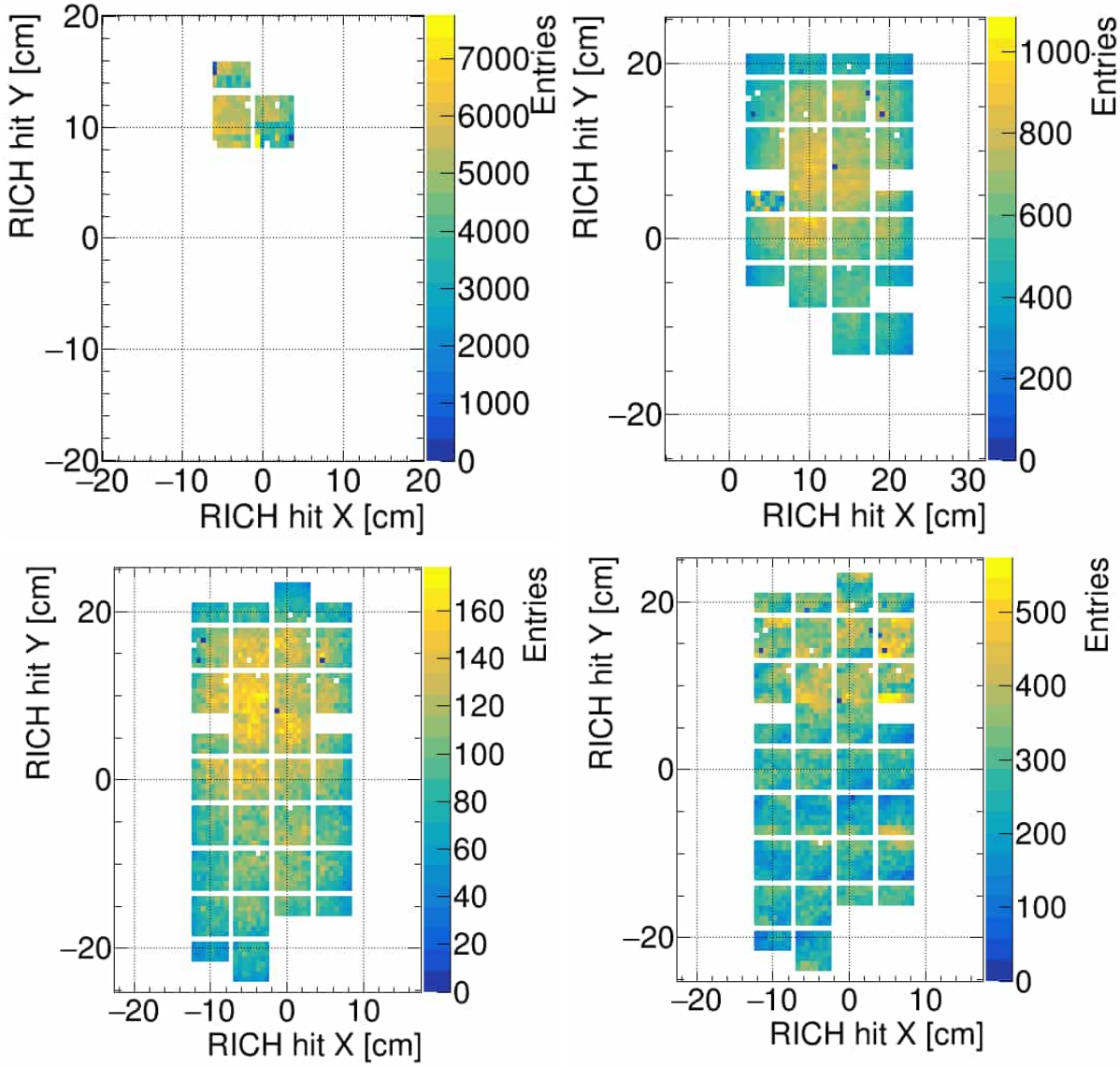

Figure B.7.5: Hit distributions of the mRICH detector. Top Left: March 2019 with ToT cut. Top Right: November 2019 with ToT cut. Bottom Left: March 2020 with ToT cut. Bottom Right: March 2020 without ToT cut.

In the configuration of March 2020 with the highest acceptance, a huge number of events could be reconstructed from the free streaming data. The event building is triggering on a certain time window and a minimal number of digis in selected subsystems. Based on this selection and the use of our ring finding algorithm many Cherenkov rings could be found (see Fig. B.7.7). The rings in mCBM show an interesting difference to rings expected in CBM. The mRICH detector is placed in the particle beam and the particles passing the detector create in addition to the Cherenkov ring a signal in the center of the ring (Cherenkov radiation in the glass window of the MAPMT).

The mTOF detector in the mCBM setup is installed directly in front of the mRICH and is a perfect detector to show the spatial correlations as well as to perform tracking. In an ideal case a track from the mTOF detector should point to the center of the RICH ring, as the mCBM experiment is running without a magnet. Simulations and reality show, that the particles are getting slightly bent and so the tracks and rings are not matching perfectly. The distance between a ring and the closest track is shown in Fig. B.7.6. The distance is peaking at approx 8 cm.

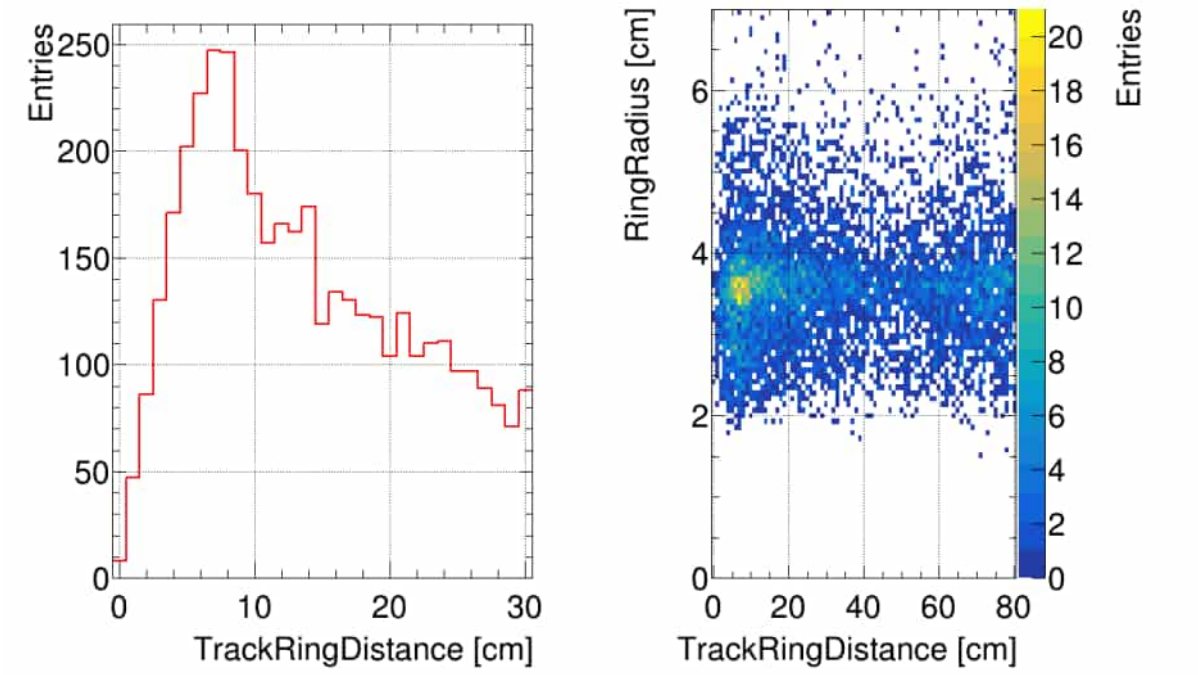

Figure B.7.6: Left: Ring-Track Distance between the mRICH and mTOF detectors. Right: Radius versus Ring-Track Distance. The track used is the closest track to the found ring center.

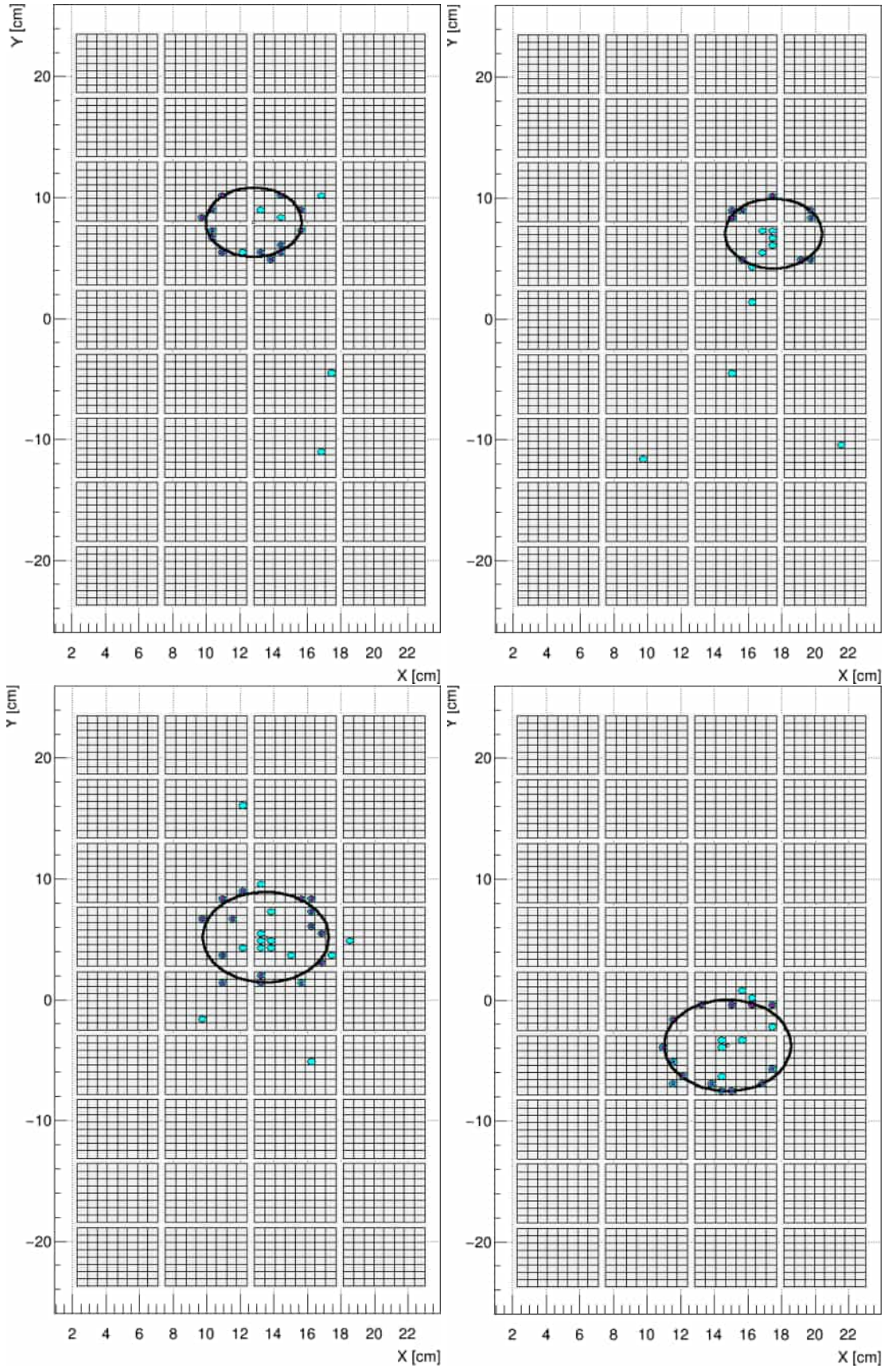

Figure B.7.7: Single Event displays with RICH Rings. The cyan coloured points show the hits in the MAPMT pixels that survive the ToT-cut. The black circle is the found ring in the event and the dots with a magenta coloured dot inside are the hits, that are matched to the fitted ring.

B.8 mPSD

The PSD (the Projectile Spectator Detector) is the forward hadron compensating lead/scintillator calorimeter, which will be used in the CBM experiment to measure the collision centrality and the reaction plane orientation in heavy-ion collisions. The PSD has transverse and longitudinal segmentation with light readout performed via micropixel photodetectors. The PSD will be assembled from already constructed 46 individual modules and has a beam hole in the center, as presented in figure B.8.1. Each module consists out of 60 lead/scintillator assemblies with 4 mm thick scintillator plate and 16 mm thick lead plate. Total length of the module is about 5.6 nuclear interaction lengths. The transverse size of the module is 200x200 mm^2 and the weight is about 500 kg. Light from each scintillator plate is collected by the WLS fiber glued in the circle groove in the scintillator plate and stretched in the 2 mm air gap at one the lateral sides of the module. Six consecutive scintillator tiles form a section and are collected together on a separate optical connector at the end of the module. One Hamamatsu MPPC S12572-010P with active area $3\times3mm^2$ is used as photodetector for each section of the module. One optical fiber for the calibration system is glued into each optical connector in addition to these 6 WLS fibers. Other ends of 10 such fibers are collected together on separate optical connector to be illuminated by the light emitting diode (LED).

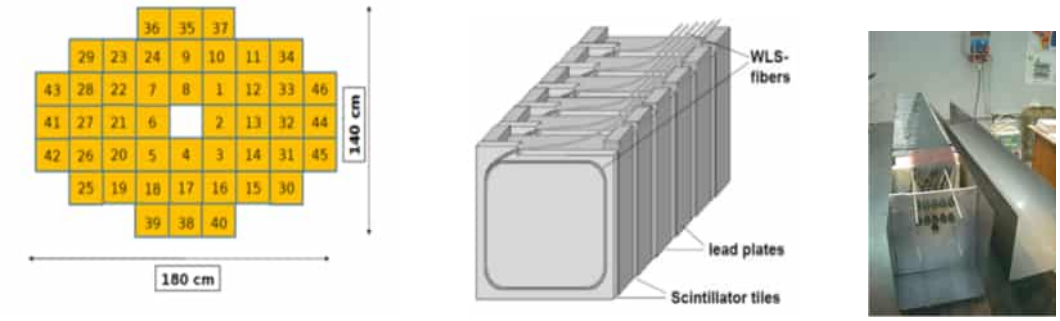

Figure B.8.1: Schematic view of the CBM PSD, left. Schematic view of the PSD module structure, center. Photo of assembled PSD module, right

Each photodetector is supplied with a common base voltage of about 70 volts, as well as individual automatic correction to the base voltage depending on the external temperature. The temperature sensor, as well as the LED for the possibility of photoelectronic calibration of MPPC, are placed on the FEE panel. The monitoring of temperature and voltage parameters from all FEEs are carried out by means of a slow control system, which provides the MPPCs gain control during the data taking. Thus, each PSD module has ten longitudinal sections, which ensures the uniformity of light collection along the modules. Schematic view and photo of a PSD module without top cap are shown in figure B.8.1, center and right.

One of the PSD module (mPSD) has been installed at the mCBM below the beam axis and is used to measure particle energies at the angle 5° relative to the beam axis from reactions in the target. The main motivations of taking data with the mPSD at mCBM is as follows:

- Test the FEE and readout electronics of the mPSD with full DAQ and control systems as of the full CBM experiment.
- Obtain time correlations between the mPSD and other detector subsystems in a realistic experimental environment.
- Test the rate capability and radiation tolerance of the MPPC, FEE and readout electronics of the mPSD.

B.8.1 mPSD readout concept

The signal readout of the PSD at CBM will be performed with an ADC board represented in figure B.8.2 (left) and an Addon board represented in figure B.8.2 (right). Estimation of accumulated neutron flux for 2 months of operation gives about 10^{11} for a board that hosts MPPCs. To avoid radiation influence on the electronics, no amplification circuitry will be mounted at the calorimeter and the ADC boards will be distanced from the calorimeter at about 25 - 40 m. The Addon board at the mPSD is placed below the mPSD and is connected with a MPPCs board in the mPSD via 5 m of 50 Ω cable.

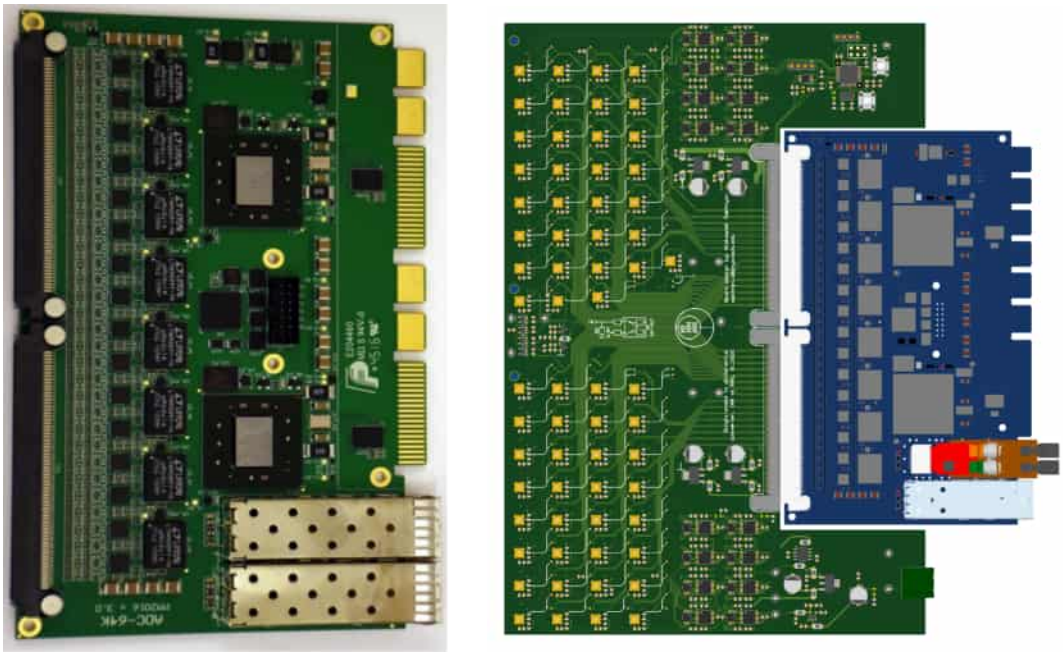

Figure B.8.2: 64-channel ADC board with 2 FPGA Kintex 7 (left); Addon board design with the ADC board mounted (right)

Signals from MPPCs are collected by the ADC Addon board, which provides a single-ended interface based on single-ended to differential converters AD8138 ICs. The design allows for an adjustable input and output offset, utilizing the whole dynamic range of the converter. Besides providing a signal interface, Addon board includes an MPPC offset adjustment system, that consists out of 16 four-channel digital to analog converters (DACs) with unity-gain buffers. DACs provide a DC offset on the signal line, providing fine adjustment of the voltage over the MPPC's terminals. Control of the DACs is accomplished through an STM32F103 microcontroller placed on the Addon board, which receives commands and adjustment data from the ADC board.

Signals are then digitized by the ADC board initially designed for the ECAL detector of PANDA experiment (see figure B.8.2, left). The 64-channel board is based on LTM9011 ADC with digitization rate up to 125Msps and 14-bit digitization resolution. The ADC board is mounted directly onto the Addon board (see figure B.8.2, right), and the whole assembly is designed to fit standard 6U Eurocard cradles. Digitized samples of 64 analog signals are sent to 2 Kintex 7 FPGAs using 128 LVDS links. Each FPGA processes data from 32 channels. Signal processing algorithm is based on the Prony-LS fitting procedure, which allows working with signals near the noise level, and is also used for the pile-up recognition. Such algorithm will be implemented in the FPGA firmware in the future. To meet the requirements of experiment's DAQ, GBT FPGA transceiver was integrated into the firmware. GBT allows to transmit data, slow control and clock signals. Expected data rate is 1MHz per channel that gives a constrain of

100bit/hit for GBT data rate of 3.2 Gbit/s. LMK0460 jitter cleaner is used for generation of ADC and MGTREF clocks. After a reset signal, 100MHz clock from on-board generator TD-100 is used as a master clock. After GBT RX synchronization is established, source is switched to an external clock, sourced from GBT RX. The clock switching scheme allows to maintain common DAQ clock domain. Measuring hit time in trigger-less readout occurs relative to the time counting named "timeslice", which is synchronized for the whole experiment readout.

B.8.2 The first mPSD beam test results at mCBM

At the end of 2019 and beginning of 2020, beam tests at mCBM@SIS18 were carried out with Au and Pb ions at 1.01 - 1.22 AGeV energy range. The main goal was to test detectors subsystems, DAQ and online data aggregation procedure. Test of the mPSD prototype as a part of mCBM experiment allows to approve and verify the feasibility of the PSD readout concept. The prototype includes crucial parts of the readout such as Addon prototype board and ADC FPGA readout board. In this setup, Addon incorporated only the single-ended to differential converters and the necessary power systems. Photo of the assembled FEE setup is represented on figure B.8.3.

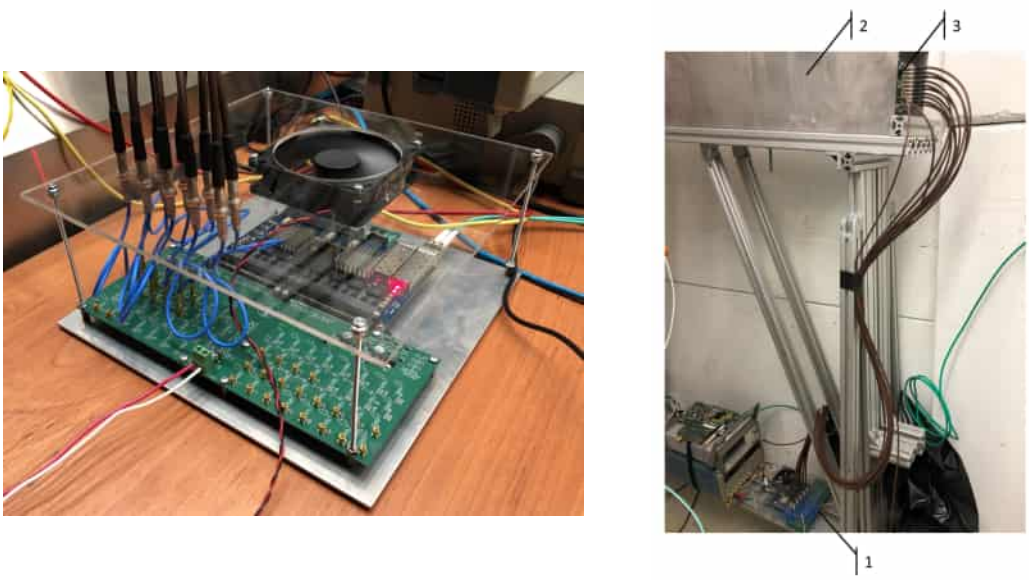

Figure B.8.3: Photo of the ADC board assembled with the Addon board prototype (left); photo of mPSD module connected to FEE (right; 1 - Addon and ADC assembly, 2 - mPSD, 3 - MPPC board)

ADC FPGA board was connected to mCBM DAQ via GBT protocol used for data transport, clock distribution and configuration purposes. The ADC was used in 80 Msps digitization mode, with an upgrade up to 120 Msps scheduled in 2020. Each channel is triggered independently by amplitude threshold crossing and extracts data points from the waveform of the input signal measured in a fixed gate. The ADC takes data in trigger-less readout mode according to CBM DAQ requirements. In addition, prototypes of all crucial software parts such as data unpacker, event building and data monitor were developed and tested. In 2021, it is planned to adapt the mPSD readout to the Common Readout Interface (CRI).

B.8.3 Preliminary mPSD test results

One of the prime aims of mCBM is to test and validate the data processing concept and the reconstruction software which are being developed for the full CBM experiment. mCBM thus

will be a demonstrator for the computing concept of CBM, including the reconstruction of events and selection of data in real-time and the full offline data analysis. It is thus planned to use already existing software components as far as possible for both online and offline computing in mCBM. The challenge of the trigger-less readout is time synchronization and event building procedure. It is necessary to construct events from signals based on their time stamps while data processing.

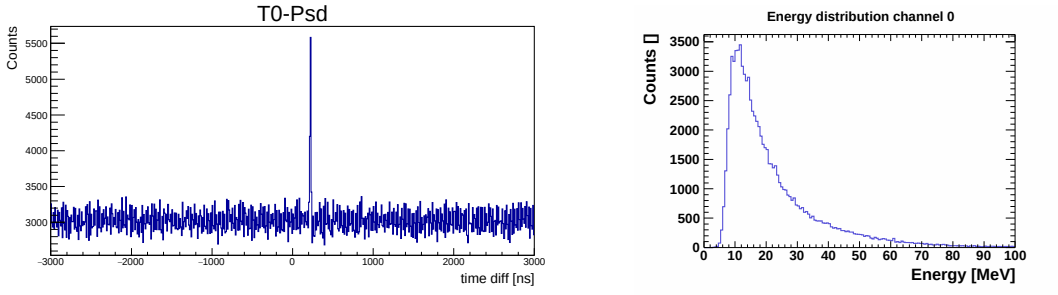

Figure B.8.4: T0-Psd time correlation(left); mPSD energy deposition in first section (right)

During the data acquisition, information from all the detectors of the mCBM experiment is recorded in a common binary file. To check the synchronization of the data from the detectors, the time correlation graphs are constructed (see figure B.8.4). An explicit peak in the distribution of the difference in the response time of the detectors T0 and mPSD (time offset), located at about 200 ns, indicates the correlation of the data and serves to select beam events.

In the same way, the timestamps of signals from all subsystems are used to attribute these signals to a specific event. To ensure the possibility of this approach, time synchronization between the subsystems is used taking into account the time offsets that are inevitably introduced during the signal acquisition process. In the current approach, we assume the signals to form a single event, if their time stamps are located in a single time window of 200ns. In addition to introducing a fixed time window for event selection, conditions on the minimum number of signals from subsystems that are located in the considered time window can be applied. Such a straightforward approach is justified at the debugging stage and will be improved in the future.

The distribution of the mPSD energy deposition in the first section after event building is shown in figure B.8.4 (right).

C List of Acronyms

A:	ADC	Analog-to-Digital Converter
	AFCK	AMC FMC Carrier Kintex
	AGS	Alternating Gradient Synchrotron
	ALICE	A Large Ion Collider Experiment
	AMC	Advanced Mezzanine Card
	ANN	Artificial Neural Network
	ASIC	Application Specific Integrated Circuit
	AWRF	Anode Wire Response Function
B:	BDT	Boosted Decision Tree
	BNL	Brookhaven National Laboratory
	BR	Branching Ratio
C:	CBM	Compressed Baryonic Matter
	CDR	Conceptual Design Review
	CERN	Conseil Européen pour la Recherche Nucléaire
	CF	Carbon Fibre
	CFRP	Carbon Fibre Reinforced Plastic
	CLK	CLocK
	CPU	Central Processing Unit
	CRI	Common Readout Interface
	CRB	Common Readout Board
	CSA	Charge Sensitive Amplifier
D:	DAQ	Data AcQuisition
	DCS	Detector Control System
	DESY	Deutsches Elektronen-SYnchrotron
	DPB	Data Processing Board
	DSP	Digital Signal Processor
	DSTRD	Double-Sided TRD
	DTW	Drift Time Window
E:	ECAL	Electromagnetic CALorimeter
	ECS	Experiment Control System
	EDR	Engineering Design Review
	ENC	Equivalent Noise Charge
	ENOB	Effective Number Of Bits
	ESD	ElectroStatic Discharge
F:	FAIR	Facility for Antiproton and Ion Research
	FASP	Fast Analog Signal Processor
	FEB	Front-End Boards
	FEE	Front-End Electronic
	FIFO	First In First Out
	FLES	First Level Event Selector

	FLIB	FLES Interface Board
	FLIM	FLES Interface Module
	FMC	FPGA Mezzanine Card
	FNR	First Neighbor Readout
	FPGA	Field Programmable Gate Array
	FT	Flat Top
	FWHM	Full Width Half Maximum
G:	GBT	GigaBit Transceiver
	GEANT	GEometry ANd Tracking
	GEM	Gas Electron Multiplier
	GH	Glueing Hours
H:	HCA	Host Channel Adapter
	HDMI	High-Definition Multimedia Interface
	HDL	Hardware Description Language
	HDR	200Gb/s InfiniBand network interconnection
	HSD	Hadron String Dynamics
	HT	High Tension
	HV	High Voltage
I:	ID	IDentification
	IIR	Infinite Impulse Response
	IMR	Intermediate Mass Region
	ISO	International Organization for Standardization
J:	JINR	Joint Institute for Nuclear Research
L:	LFR	Likelihood Function Ratio
	LHC	Large Hadron Collider
	LQ	Likelihood derived from charge (Q) measurement
	LS	Layer Support
	LV	Low Voltage
	LVDB	Low Voltage Distribution Board
M:	MADC	Multiplexed Analog-to-Digital Converter
	MAPD	Multi-Avalanche Photo-Diodes
	MAPS	Monolithic Active Pixel Sensors
	MAPT	Multi-Anode Photomultiplier Tubes
	MBS	Multi Branch System
	MC	Monte Carlo
	MCBM	mini-CBM
	MIMOSIS	Minimum Ionizing Particle
	MIP	Minimum Ionizing Particle
	MPO	Multi-fiber Push On connector
	MPV	Most Probable Value
	MRPC	Multi-gap Resistive Plate Chambers

	MSV	Modularized Start Version
	MUCH	MUon CHambers
	MVD	Micro Vertex Detector
	MWPC	Multi-Wire Proportional Chamber
N:	NICA	Nuclotron-based Ion Collider fAcility
	NIEL	Non-Ionizing Energy Loss
	NIST	National Institute of Standards and Technology
P:	PASA	Pre-Amplifier Shaping Amplifier
	PC	Power Consumption
	PCB	Printed Circuit Board
	PDF	Probability Density Function
	PE	PolyEthylene
	PID	Particle IDentification
	PMMA	PolyMethylMethAcrylate
	POB	POwer Boards
	PP	PolyPropylene
	PRF	Pad Response Function
	PRR	Production Readiness Review
	PS	Power Supply
	PS	Proton Synchrotron (CERN)
	PSD	Projectile Spectator Detector
	PWR	PoWeR (USB socket)
Q:	QDC	Charge-to-Digital Converter
	QGP	Quark-Gluon Plasma
R:	RCT	Readout ConTroller
	REQ	REQuest signal
	RHIC	Relativistic Heavy-Ion Collider
	RICH	Ring Imaging CHerenkov
	RPC	Resistive Plate Chamber
	RST	ReSeT signal
	ROB	Read-Out Board
	ROC	Read-Out Chamber
S:	SIS	Schwer-Ionen Synchrotron
	SPADIC	Self-triggered Pulse Amplification and Digitization ASIC
	SPS	Super Proton Synchrotron
	SSTRD	Single-Sided TRD
	ST	Shaping Time
	STAR	Solenoidal Tracker At RHIC
	STS	Silicon Tracking System
T:	TFC	Timing and Flow Control system
	THR	THReshold

	TOF	Time-Of-Flight
	TR	Transition Radiation
	TRD	Transition Radiation Detector
	TTL	Transistor-Transistor Logic
U:	UDP	User Datagram Protocol
	UrQMD	Ultra-relativistic Quantum Molecular Dynamics
	UNILAC	Universal Linear Accelerator
	UMC	United Microelectronics Corporation
	UV	Ultra-Violet
V:	VECC	Variable Energy Cyclotron Centre
	VTR	Versatile TransReceiver
	VTT	Versatile Twin-Transmitter
W:	WH	Working Hours
	WHPD	Working Hour Per Day
	WHPW	Working Hour Per Week
	WLS	WaveLength Shifter
X:	XT	Cross-Talk
	XYTER	X-Y-Time-Energy Readout

D The CBM Collaboration

A. Adler[1], A. Agarwal[2], K. Agarwal[3], Z. Ahammed[2], A. Ahmad[4], N. Ahmad[5], A. Akindinov[6], P. Akishin[7], M. Al-Turany[8], I. Alekseev[6], E. Alexandrov[7], I. Alexandrov[7], A. Andronic[9], H. Appelshäuser[10], D. Argintaru[11], B. Arnoldi-Meadows[10], E. Atkin[12], M.D. Azmi[5], V. Baban[11], S. Bähr[13], M. Bajdel[8], G. Balassa[14], M. Balzer[13], N. Baranova[15], M. Baszczyk[16], E. Bechtel[10], J. Becker[13], K.-H. Becker[17], M. Becker[18], S. Belogurov[7,12], A. Belousov[19], A. Bercuci[20], R. Berendes[9], D. Bertini[8], O. Bertini[8], O. Bezshyyko[21], P.P. Bhaduri[2], A. Bhasin[22], S.A. Bhat[4], T.A. Bhat[4], W.A. Bhat[4], B. Bhattacharjee[23], A. Bhattacharyya[24], S. Biswas[25], T. Blank[13], D. Blau[26,12], C. Blume[10,8], J. Brzychczyk[27], T. Bus[10], A. Bychkov[28], M. Cãlin[11], M. Caselle[13], A. Chakrabarti[24], S. Chatterjee[25], S. Chattopadhyay[2,25], H. Cherif[10,8], P. Chudoba[29], E. Clerkin[30], M. Csanád[31], P. Dahm[8], Supriya Das[25], Susovan Das[3], J. de Cuveland[19], A. Demanov[12], D. Dementiev[28], Zhi Deng[32], H. Deppe[8], I. Deppner[33], O. Derenovskaya[7], M. Deveaux[10], Sheng Dong[34,33], E. Dorenskaya[6], P. Dorosz[16], A.K. Dubey[2], A. Dubla[8], M. Dürr[18], V.V. Elsha[28], D. Emschermann[8], T. Eşanu[11], J. Eschke[30,8], M. Esen[10], Xingming Fan[35,57], O. Fateev[28], C. Feier-Riesen[18], Sheng-Qin Feng[36], F. Fidorra[9], D. Finogeev[37], P. Fischer[38], H. Flemming[8], J. Förtsch[17], P. Foka[8], U. Frankenfeld[8], V. Friese[8], I. Fröhlich[10], J. Frühauf[8], T. Galatyuk[39,8], R. Ganai[24], G. Gangopadhyay[24], Xin Gao[8], P. Gasik[30,8], T. Geßler[18], C. Ghosh[2], S.K. Ghosh[25], D. Giang[10], S. Gläßel[10], L. Golinka-Bezshyyko[21], O. Golosov[12], S. Golovnya[40], M. Golubeva[37], D. Golubkov[6], S. Gope[23], S. Gorbunov[19], S. Gorokhov[40], D. Gottschalk[33], F. Guber[37], M. Gumiński[41], A. Gupta[22], Yu. Gusakov[28], R. Haas[18], Dong Han[32], H. Hartmann[19], Shu He[34], J. Hehner[8], N. Heine[9], N. Herrmann[33,8], J.M. Heuser[8], C. Höhne[18], R. Holzmann[8], Dongdong Hu[42,33], Guangming Huang[34], D. Hutter[19], D. Ivanishchev[43], P. Ivanov[12], Victor Ivanov[7,12], Vladimir Ivanov[43,12], A. Ivashkin[37], A. Izvestnyy[37], T. Janson[1], A. Jipa[11], I. Kadenko[21], P. Kähler[9], B. Kämpfer[35,57], K.-H. Kampert[17], R. Kapell[8], R. Karabowicz[8], N. Kargin[12], D. Karmanov[15], N. Karpushkin[37], E. Kashirin[12], V.K.S. Kashyap[44], K. Kasiński[16], A. Kazantsev[26], U. Kebschull[1], G. Kekelidze[28], M.M. Khan[5], S. Khan[3], A. Khanzadeev[43,12], F. Khasanov[6], A. Kiryakov[40], M. Kiš[8], I. Kisel[19], P. Kisel[19,8,7], S. Kiselev[6], P. Klaus[10], R. Kłeczek[16], Ch. Klein-Bösing[9], V. Klochkov[30], K. Koch[8], L. Kochenda[43,12], P. Koczoń[8], M. Kohn[9], R. Kolb[33], A. Kolozhvari[28], B. Komkov[43], M. Korolev[15], I. Korolko[6], R. Kotte[35], M. Koziel[10], G. Kozlov[19,7], V. Kozlov[43], P. Kravtsov[43,12], I. Kres[17], D. Kresan[8], M. Kruszewski[41], A.V. Kryanev[7,12], E. Kryshen[43], W. Kucewicz[16], L. Kudin[43], I. Kudryashov[15], A. Kugler[29], P. Kuhl[8], Ajay Kumar[45], Ajit Kumar[2], L. Kumar[46], S.K. Kundu[47], V. Kyva[48], V. Ladygin[28], E. Lavrik[30], I. Lazanu[11], A. Lebedev[8,7], S. Lebedev[18,7], E. Lebedeva[18], J. Lehnert[8], Chao Li[42], Yuanjing Li[32], V. Lindenstruth[19,8], Feng Liu[34], I. Lobanov[40], E. Lobanova[40], S. Löchner[8], P.-A. Loizeau[30], K. Łojek[27], O. Lubynets[8,10], Xiaofeng Luo[34], A. Lymanets[8], N. Lyublev[6], Jian-Hao Ma[36], S. Mahajan[22], Z. Majka[27], A. Malakhov[28], D. Malkevich[6], B. Mallick[49], O. Malyatina[12], M. Mandal[2], V. Manko[26], O. Maragoto Rodriguez[8,10], A.M. Marin Garcia[8], J. Markert[8], T. Matulewicz[50], S. Mehta[3], M. Merkin[15], A. Meyer-Ahrens[9], J. Michel[10], P. Miedzik[41], K. Mikhailov[6], V. Mikhaylov[29], V. Militsija[48], M.F. Mir[4], D. Miskowiec[8], B. Mohanty[44], I. Momot[48,10], H. Morgenweck[9], T. Morhardt[8], S. Morozov[37], W.F.J. Müller[30], C. Müntz[10], S. Mukherjee[25], P. Munkes[9], Yu. Murin[28], E. Nandy[2], L. Naumann[35], F. Nickels[8], W. Niebur[8], V. Nikulin[43], D. Normanov[12], P. Otfinowski[16], J.H. Otto[18], Liang-ming Pan[51], I. Panasenko[3,48], S. Pandey[45], P. Parfenov[12], S. Parzhitskiy[28], V. Patel[17], C. Pauly[17], V. Petráček[52], M. Petri[10], M. Petriş[20], M. Petrovici[20], O. Petukhov[37], D. Pfeifer[17], P. Pfistner[13], K. Piasecki[50], J. Pietraszko[8], R. Płaneta[27], V. Plotnikov[6], V. Plujko[21], J. Pluta[53], K. Poźniak[41,50], S.K. Prasad[25], M. Prokudin[6], M. Pugach[48], V. Pugatch[48], A. Puntke[9], L. Radulescu[20], S. Raha[25], P. Raisig[10], R. Ray[25], A. Redelbach[19], A. Reinefeld[54], A. Reshetin[37], C. Ristea[11], O. Ristea[11], A. Rodriguez Rodriguez[10,8], F. Roether[10], R. Romaniuk[41], A. Rost[30,39], E. Rostchin[43,12], A. Roy[47], S. Roy[25], E. Rubio[33], Yu. Ryabov[43], R. Sahoo[47], P.K. Sahu[49], S.K. Sahu[49], J. Saini[2], F. Salem[54], S.S. Sambyal[22], V. Samsonov[43,12,58], C. Schiaua[20], F. Schintke[54], C.J. Schmidt[8], D. Schmidt[1],

H.R. Schmidt[3,8], P.M. Schneider[9], T. Schütt[54], F. Seck[39], I. Segal[12], I. Selyuzhenkov[8,12], A. Semennikov[6], A. Sen[25], A. Senger[30], P. Senger[30,10], A. Shabanov[37], A. Shabunov[28], N. Sharma[46], A.D. Sheremetiev[28], Shusu Shi[34], S. Shirinkin[6], M. Shiroya[8,10], M. Shitenkow[28], V. Shumikhin[12], I. Sibiryak[26], V. Sidorenko[13], C. Simon[33], C. Simons[8], A.K. Singh[55], B.K. Singh[45], C.P. Singh[45], O. Singh[5], R. Singh[44], V. Singhal[2], L. Škoda[52], D. Spicker[10], D. Stach[35], P. Staszel[27], D. Storozhyk[48], M. Strikhanov[12], J. Stroth[10,8], C. Sturm[8], Yuan Su[42], N. Sukhov[28], R. Sultanov[6], Yongjie Sun[42], Zhengyang Sun[42], D. Svirida[6], R. Szczygieł[16], A. Taranenko[12], O. Tarassenkova[43], A. Toia[8,10], M. Träger[8], M. Traxler[8], E. Trifonova[13], Yu. Tsyupa[40], N.G. Tuturas[11], F. Uhlig[8], K.L. Unger[13], I. Vassiliev[8], O. Vasylyev[8], R. Visinka[8], E. Volkova[3], A. Vorobiev[40], A. Voronin[15], L. Wahmes[9], Botan Wang[32], Dong Wang[34], Tianxing Wang[42], Xinjian Wang[42], Yi Wang[32], A.A. Weber[18], M. Weber[13], P. Weidenkaff[33], J.P. Wessels[9], D. Wielanek[53], A. Wieloch[27], A. Wilms[8], Gy. Wolf[14], Ke-Jun Wu[36], Qiqi Wu[51], Junfeng Yang[42], Zhongbao Yin[34], In-Kwon Yoo[56], Jianhui Yuan[42], I. Yushmanov[26], W. Zabołotny[41,50], Yu. Zaitsev[6], N.I. Zamiatin[28], H. Zbroszczyk[53], M. Zhalov[43], Qiunan Zhang[33,32], Xiaoming Zhang[34], Yu Zhang[34], Sheng Zheng[36], Daicui Zhou[34], Jian Zhou[42], Wenxiong Zhou[51], Xianglei Zhu[32], A. Zinchenko[28], I. Zivko[6], F. Zorn[18], W. Zubrzycka[16], P. Zumbruch[8]

[1]Institute for Computer Science, Goethe-Universität Frankfurt, Frankfurt, Germany
[2]Variable Energy Cyclotron Centre (VECC), Kolkata, India
[3]Physikalisches Institut, Eberhard Karls Universität Tübingen, Tübingen, Germany
[4]Department of Physics, University of Kashmir, Srinagar, India
[5]Department of Physics, Aligarh Muslim University, Aligarh, India
[6]Institute for Theoretical and Experimental Physics named by A.I. Alikhanov of National Research Centre "Kurchatov Institute" (ITEP) in Moscow, Russia (ITEP), Moscow, Russia
[7]Laboratory of Information Technologies, Joint Institute for Nuclear Research (JINR-LIT), Dubna, Russia
[8]GSI Helmholtzzentrum für Schwerionenforschung GmbH (GSI), Darmstadt, Germany
[9]Institut für Kernphysik, Westfälische Wilhelms-Universität Münster, Münster, Germany
[10]Institut für Kernphysik, Goethe-Universität Frankfurt, Frankfurt, Germany
[11]Atomic and Nuclear Physics Department, University of Bucharest, Bucharest, Romania
[12]National Research Nuclear University MEPhI (Moscow Engineering Physics Institute), Moscow, Russia
[13]Karlsruhe Institute of Technology (KIT), Karlsruhe, Germany
[14]Institute for Particle and Nuclear Physics, Wigner Research Centre for Physics, Hungarian Academy of Sciences, Budapest, Hungary
[15]Skobeltsyn Institute of Nuclear Phyiscs, Lomonosov Moscow State University (SINP-MSU), Moscow, Russia
[16]AGH University of Science and Technology (AGH), Kraków, Poland
[17]Fakultät für Mathematik und Naturwissenschaften, Bergische Universität Wuppertal, Wuppertal, Germany
[18]Justus-Liebig-Universität Gießen, Gießen, Germany
[19]Frankfurt Institute for Advanced Studies, Goethe-Universität Frankfurt (FIAS), Frankfurt, Germany
[20]Horia Hulubei National Institute of Physics and Nuclear Engineering (IFIN-HH), Bucharest, Romania
[21]Department of Nuclear Physics, Taras Shevchenko National University of Kyiv, Kyiv, Ukraine
[22]Department of Physics, University of Jammu, Jammu, India
[23]Nuclear and Radiation Physics Research Laboratory, Department of Physics, Gauhati University, Guwahati, India
[24]Department of Physics and Department of Electronic Science, University of Calcutta, Kolkata,

India
[25]Department of Physics, Bose Institute, Kolkata, India
[26]National Research Centre "Kurchatov Institute", Moscow, Russia
[27]Marian Smoluchowski Institute of Physics, Jagiellonian University, Kraków, Poland
[28]Veksler and Baldin Laboratory of High Energy Physics, Joint Institute for Nuclear Research (JINR-VBLHEP), Dubna, Russia
[29]Nuclear Physics Institute of the Czech Academy of Sciences, Řež, Czech Republic
[30]Facility for Antiproton and Ion Research in Europe GmbH (FAIR), Darmstadt, Germany
[31]Eötvös Loránd University (ELTE), Budapest, Hungary
[32]Department of Engineering Physics, Tsinghua University, Beijing, China
[33]Physikalisches Institut, Universität Heidelberg, Heidelberg, Germany
[34]College of Physical Science and Technology, Central China Normal University (CCNU), Wuhan, China
[35]Institut für Strahlenphysik, Helmholtz-Zentrum Dresden-Rossendorf (HZDR), Dresden, Germany
[36]College of Science, China Three Gorges University (CTGU), Yichang, China
[37]Institute for Nuclear Research (INR), Moscow, Russia
[38]Institut für Technische Informatik, Universität Heidelberg, Heidelberg, Germany
[39]Institut für Kernphysik, Technische Universität Darmstadt, Darmstadt, Germany
[40]Institute for High Energy Physics (IHEP), Protvino, Russia
[41]Institute of Electronic Systems, Warsaw University of Technology, Warsaw, Poland
[42]Department of Modern Physics, University of Science & Technology of China (USTC), Hefei, China
[43]Petersburg Nuclear Physics Institute named by B.P.Konstantinov of National Research Centre "Kurchatov Institute" (PNPI), Gatchina, Russia
[44]National Institute of Science Education and Research (NISER), Bhubaneswar, India
[45]Department of Physics, Banaras Hindu University (BHU), Varanasi, India
[46]Department of Physics, Panjab University, Chandigarh, India
[47]Indian Institute of Technology Indore, Indore, India
[48]High Energy Physics Department, Kiev Institute for Nuclear Research (KINR), Kyiv, Ukraine
[49]Institute of Physics, Bhubaneswar, India
[50]Faculty of Physics, University of Warsaw, Warsaw, Poland
[51]Chongqing University, Chongqing, China
[52]Czech Technical University (CTU), Prague, Czech Republic
[53]Faculty of Physics, Warsaw University of Technology, Warsaw, Poland
[54]Konrad-Zuse-Zentrum für Informationstechnik Berlin (ZIB), Berlin, Germany
[55]Indian Institute of Technology Kharagpur, Kharagpur, India
[56]Pusan National University (PNU), Pusan, Korea
[57]also: Technische Universität Dresden, Dresden, Germany
[58]also: St. Petersburg Polytechnic University (SPbPU), St. Petersburg, Russia